REPORT NO. M10569

Cathode Precursor Production Pilot Plant (C4P): Stage 3 Summary Report

Results of research carried out as MRIWA Project M10569

at CSIRO and Curtin University

by

CSIRO Team: Neda Ghaebi Panah, Michael Jackson, Nicky Chapman, Kate Moyes-Martin, Adalberto Leles de Souza, Syahmi Johanie, Diego Holanda Pereira de Souza, Aissa Polenio, Alton Grabsch, Anna Nowosielska, Jian Li, Keith Barnard, Sean Paton.

Curtin University Team: Carlos Perea Solano, Lauren Jackson, Deepak Kumar, Laurence Dyer, Leqi (Mark) Zhao, Zongping Shao.

Date published June 2026

This report is a redacted version of a full technical report prepared by CSIRO and Curtin University for MRIWA. Specific test procedures, conditions and results have been withheld from public dissemination, however may be made available to interested parties on a case-by-case basis.

Distributed by: MRIWA
1 Adelaide Terrace
Perth WA 6000
to which all enquiries should be addressed

1 Acknowledgements

MINISTER FOR MINES AND PETROLEUM
Hon Daniel Pastorelli MLA

CHIEF EXECUTIVE OFFICER, MINERALS RESEARCH INSTITUTE OF WESTERN AUSTRALIA
Nicole Roocke

LEAD INVESTIGATOR, CSIRO, Mineral Resources
Keith Barnard

LEAD INVESTIGATOR, Curtin University, School of Mines, Minerals & Chemical Engineering
Jacques Eksteen

AUTHORS:
CSIRO Team: Neda Ghaebi Panah, Michael Jackson, Nicky Chapman, Kate Moyes-Martin, Adalberto Leles de Souza, Syahmi Johanie, Diego Holanda Pereira de Souza, Aissa Polenio, Alton Grabsch, Anna Nowosielska, Jian Li, Keith Barnard.
Curtin University Team: Carlos Perea Solano, Lauren Jackson, Deepak Kumar, Laurence Dyer, Leqi (Mark) Zhao, Zongping Shao.

REFERENCE
The recommended reference for this publication is:
G. Panah N et. al. (2025) Cathode Precursor Production Pilot Plant (C4P): Stage 3 Summary Report. CSIRO and Curtin University, Australia.

DOI: 10.71342/748978941933

PARTICIPATING ORGANISATIONS
CSIRO and Curtin University

KEYWORDS AND TAGS
pCAM, Lithium-ion, batteries, battery materials, energy storage, nickel, cobalt, manganese, NCM, NMC.

Published 2026 by the Minerals Research Institute of Western Australia
This report is published in digital format (PDF) and is available online at https://www.mriwa.wa.gov.au/research-projects/project-portfolio/

CONTACT
Minerals Research Institute of Western Australia
1 Adelaide Terrace
Perth WA 6000
+61 8 6180 4340
mail@mriwa.wa.gov.au
https://www.mriwa.wa.gov.au/

Contents

Figures

Tables

Acknowledgments

CSIRO Mineral Resources and Curtin University would like to thank the Minerals Institute of Western Australia (MRIWA) for the financial support, intellectual input and industry connections which have made this project possible. CSIRO Mineral Resources Characterisation group is thanked for conducting the analysis. The CSIRO Waterford workshop is thanked for their invaluable technical assistance to the C4P.

Executive summary

Stage three of the Cathode Precursor Production Pilot Plant (C4P) was an extension of the research and capabilities established under the Future Batteries Industry Cooperative Research Centre (FBI-CRC) and aimed to facilitate the viability of a West Australian battery materials industry. The project was a collaboration between the Commonwealth Scientific and Industrial Research Organisation (CSIRO) and Curtin University, funded by the Minerals Research Institute of Western Australia (MRIWA). Within stage three there were seven distinct work packages conducted, namely:

- An investigation of opportunities to reject impurities during Nickel (Ni), Cobalt (Co) and Manganese (Mn) (NCM) pCAM production.
- Development of the capability to run the reactor systems in a batch mode, as previous stages had focused solely on continuous systems.
- An investigation of production methods for nickel, cobalt, manganese and aluminium (NCMA) chemistries.
- A preliminary investigation of selected next-generation pCAM production methods, including elemental gradients within particles and the use of titanium doping to control grain structure.
- The combining of computational fluid dynamics (CFD) and population balance models (PBM) to predict product parameters (a PhD student project).
- The development of an image analysis tool to provide quantitative assessments of particle parameters from SEM images (an honours student project).

Only high-level details of the results can be released at this time. If you are interested in discussing the results further, or how the C4P capabilities can assist in advancing your project please contact the team via batterymaterials@csiro.au.

1 Impurity Rejection During pCAM Production

1.1 Introduction

Currently, specifications for battery-grade chemicals are determined by foreign pCAM producers, with any potential Australian producer required to comply. It was hypothesised that some elements of these specifications are arbitrary, as they appear to be based on what traditional chemical purification flowsheets produce. To meet the required specifications, many Australian companies are developing innovative flowsheets, driven by new technologies or the properties of local feed materials [1, 2]. Some of these new flowsheets require additional processes to reject or avoid certain impurities, and these additional process steps can add significant cost. Instead, if impurity rejection during pCAM production can be demonstrated, it may enable local pCAM manufacturers to accept less pure local feed material. A less process-intensive precursor production pathway would logically have a lower cost (both OPEX and CAPEX) and result in lower CO_2 emissions, potentially representing a competitive advantage to local industry. Ten common elements were selected for testing based on prevalence in Australian nickel deposits and secondary resources, while also having tight specifications on current battery-grade chemicals.

Nine tests in total were conducted to investigate impurity rejection, with each test operated in continuous mode for approximately 11 days. Tests 1 and 9 were baseline tests with no impurities present; tests 2-8 investigated a range of impurities present in West Australian-based ores. The exact elements and concentrations are not being publicly released at this time.

1.2 Literature Review

1.2.1 Introduction to NCM Precursor Cathode Active Materials (pCAM) for Lithium-ion batteries (LIBs)

In 2024, EVs accounted for over 80–85% of global lithium(Li)-ion battery demand [3], with the split between nickel-based chemistries (e.g. NCM, NMA) and lithium iron phosphate (LFP) being about 55%:45% [4]. The increased energy density of the nickel-based chemistries delivers increased range relative to the LFP batteries but comes at the expense of reduced cycle life. Increasing the nickel content in the battery amplifies these effects. There is ongoing interest in developing materials with improved battery performance, both in terms of specific energy density (directly related to range in an EV) and cycle degradation (related to battery lifespan). Ni-rich NCM (Ni > 80 mol.%) is one material under consideration due to its energy and power density, lifespan, safety, and production costs. Nonetheless, Ni-rich layered oxides have limitations such as structural damage, thermal instability, and diminished performance at high voltages (above 4.3 V) [5] which will be discussed further in this literature review.

1.2.2 Synthesis of Ni-rich NCM layered oxide pCAM

In the past two decades, several methods have been developed for synthesising NCM cathode materials for LIBs in both research and industry. Techniques include coprecipitation, solid-state reaction, sol-gel, spray pyrolysis, hydrothermal, solvothermal and combustion. Coprecipitation and spray pyrolysis are commonly used for commercial production, whereas other approaches are not

considered commercially relevant [6]. A schematic of the most common NCM battery synthesis methods is shown in Figure 1. Each method has inherent advantages and disadvantages, as shown in Table 1.

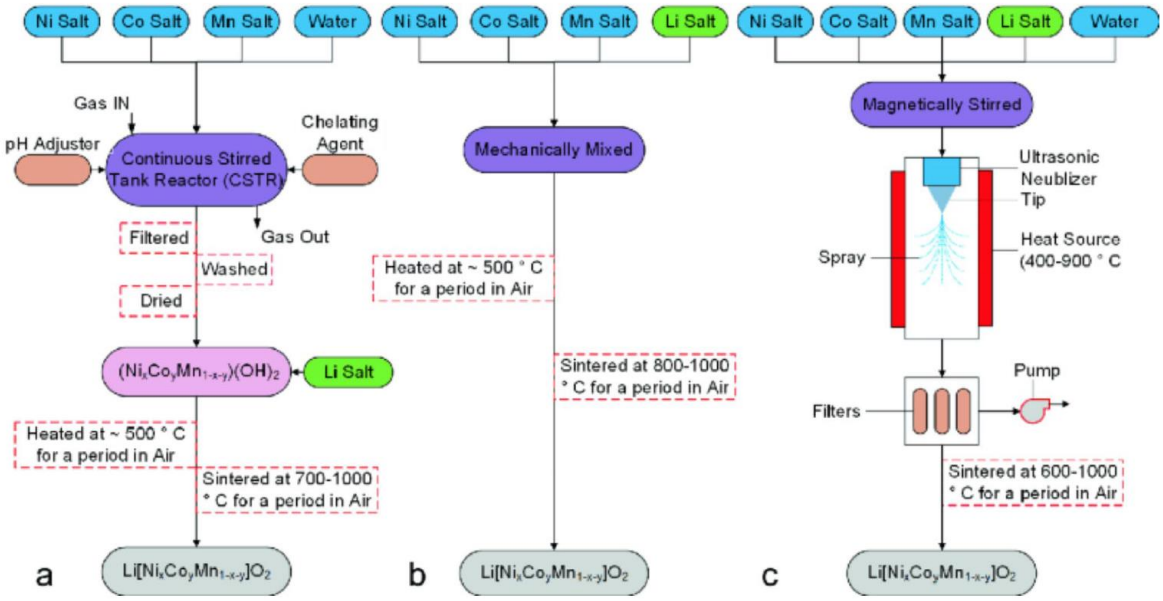

Figure 1 Schematic of NCM battery synthesis methods. a. Coprecipitation, b. Solid state, c. Spray pyrolysis [7]

Table 1 Summary of the NCM cathode synthesis methods [7]

Methods	Highlights
Solid State	[+] Most simple process, correct stoichiometry
	[−] Time and energy consuming, low homogeneity
Co-precipitation	[+] High morphology and homogeneity, tap density, well atomic-level mixing
	[−] Complex parameter control, long residence time, large wastewater,
Spray pyrolysis	[+] Faster synthesis, scalable, spherical morphology
	[−] Smaller and fragile particles resulting lowering cyclability

1.2.3 Hydroxide Coprecipitation Synthesis of NCM pCAM

Of the three main coprecipitation methods for making pCAM (hydroxide, carbonate, and oxalate), hydroxide was developed first and remains the most commonly used, especially for NCM hydroxide. It is cost-effective and efficient, producing particles with high tap-density and controlled size distribution [6, 8]. Tap-density measures the dry particle packing under vibration (standard numbers of taps), directly influencing the volumetric energy density of the final cathode.

The hydroxide coprecipitation method utilises a chelating agent, such as ammonium hydroxide (NH_4OH), to facilitate the formation of dense, single-phase spherical particles [6]. This process comprises three main stages: (1) nucleation of hydroxide precursor particles, (2) agglomeration of these primary particles, and (3) subsequent growth of secondary particles with controlled

morphology. Particle morphology plays a critical role in determining the material's charge/discharge rate capability, structural attributes, and thermal stability. Parameters including pH, temperature, stirring speed, reaction duration, atmospheric conditions, and chelating agent concentration play a critical role in the particle characteristics. Coprecipitation typically yields polycrystalline spherical particles sized between 3 and 12 µm, which consist of nanoscale primary particles ranging from 50 to 100 nm [7].

1.2.4 Structure of Ni-rich layered oxide cathodes for LIBs

The layered crystal structure of NCM cathode active material with ion positions is demonstrated in Figure 2 [5]. Previous studies believe that Li^+ (0.76 Å) and Ni^{2+} (0.69 Å) occupy the 3a site, Ni, Mn and Co take the 3b site, O is in the 6c site [5, 8].

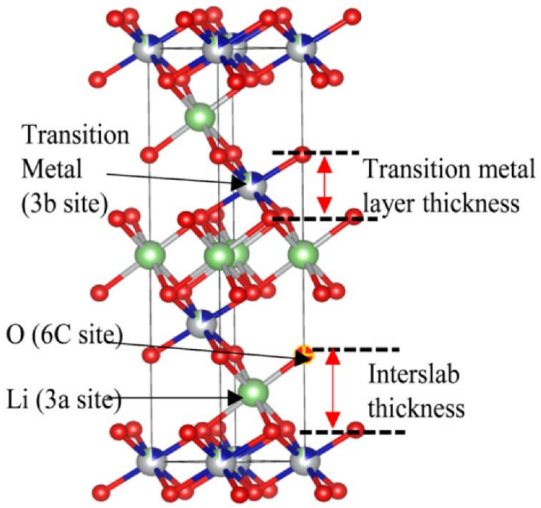

Figure 2 Layered crystal structure schematic of NCM cathode active materials ($LiNiCoMnO_2$) [5]

1.2.5 Challenges

Layered lithium transition metal oxide cathodes are essential components in advanced batteries [9]. However, NCM cathode materials face several notable challenges in achieving the often-competing priorities of high specific and volumetric capacities, high-capacity retention and high discharge voltage. These include cation mixing, lithium residue, oxygen release, particle cracking and phase transitions from layered to spinel and ultimately to rock-salt structures [9, 10].

Ni^{2+} and Li^+ may exchange their sites in the crystal structure (a process known as cation mixing) as they are very similar in ionic radii (0.69 Å for Ni^{2+} and 0.76 Å for Li^+). Cation mixing results in structural degradation, capacity loss, and poor thermal stability [9]. The structure can undergo noticeable changes between layered and cubic structures, which can influence their stability during operation and affect how well the material performs electrochemically [11]. The layered cathode structure is not thermodynamically preferred and can transform from layered → spinel → rock-salt structures, as shown in Figure 3.

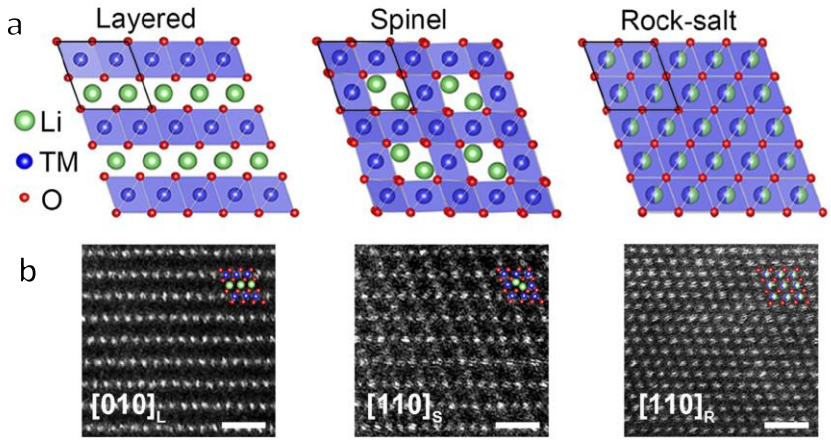

Figure 3 The layered, spinel and rock-salt phases. a. The atomic structural models. b. HAADF-STEM images [12]

This structural transformation is accelerated under specific conditions such as higher cutoff voltages, high operating temperatures or a deteriorating electrochemical environment [7]. At higher voltage (usually above 4.3 V) Ni^{2+} migrates from the TM layer to the Li layer causing cation mixing. This leads to local transformation from a layer structure to a spinel structure. With prolonged cycling at high voltages, further cation disorder occurs which results in a rock-salt structure, characterised by its low ionic conductivity. This impedes lithium-ion diffusion pathways and hinders the lithiation and delithiation processes (poor cycle life) which occurs during charging/discharging. As cycling progresses, the formation of this phase contributes to a decline in capacity retention. Analytical techniques such as XANES (X-ray Absorption Near-Edge Structure) and XPS (X-ray photoelectron spectroscopy), have revealed that the surfaces of nickel-rich layered oxides tend to accumulate undesirable lithium compounds [7]. This typically occurs due to the intentional use of excess lithium during cathode synthesis to compensate for lithium loss during high-temperature lithiation as depicted in Figure 4 [9, 10]. It also can occur during post-synthesis handling (due to exposure to ambient air), storage and electrochemical cycling. At room temperature, these lithium compounds can react with carbon dioxide and water to produce lithium carbonate (Li_2CO_3) and lithium hydroxide (LiOH), which may result in the suppression of Li^+ diffusion, irreversible capacity, increased charge transfer resistance and cation mixing [9, 10].

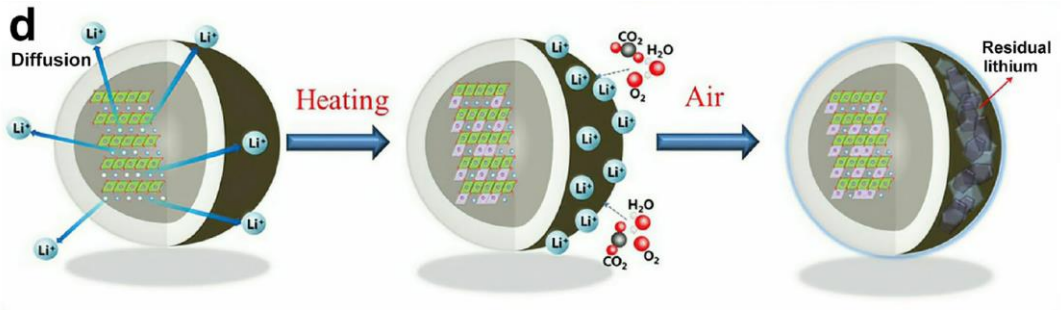

Figure 4 Schematic of the formation process of LiOH and Li_2CO_3 at an Ni-rich cathode surface [10]

The high Ni content in NCM cathodes can also lead to structural instability. Elevated levels of nickel ions in the cathode material can lead to the release of oxygen from the lattice structure. Oxygen release can destabilise the crystal structure, promote electrolyte oxidation, and initiate side reactions, contributing to structural instability and degradation of the cathode material [9].

During charging and discharging, lithium ions move in and out of the cathode material, causing it to expand and contract. This volumetric change becomes more pronounced in nickel-rich NCM materials. Over repeated cycles, this puts mechanical stress on the cathode particles, which can

result in cracking and damage to the structure. This effect becomes more pronounced once nickel content exceeds 80 mol.% [10]. Once cracks form, the electrolyte can penetrate deeper into the particles, further accelerating degradation (Figure 5) [9, 10]. The interaction between cathode materials and the electrolyte can trigger a range of side reactions, including electrolyte decomposition, transition metal ion dissolution, chemical degradation and phase transitions within the active cathode structure. These reactions not only cause decreased battery performance but also pose safety risks due to the generation of reactive gases such as oxygen and alkanes, including methane.

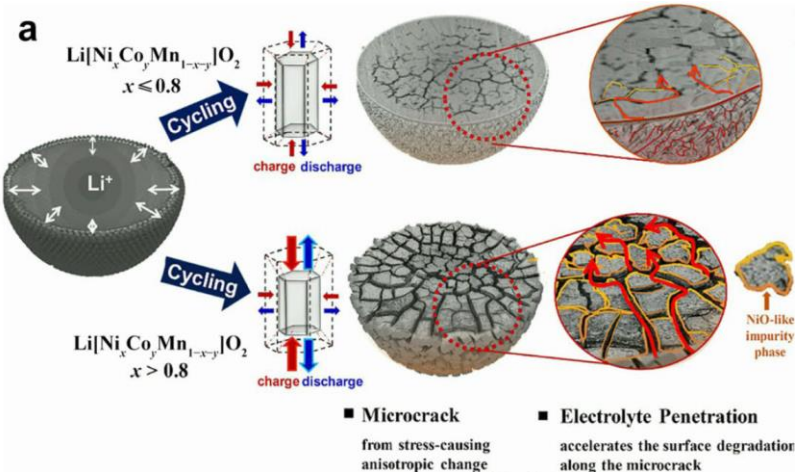

Figure 5 Capacity fading scheme of Ni-rich cathodes [10]

1.2.6 Dopants vs Impurities in the crystal structure of pCAM

Doping is a widely applied strategy in materials engineering, involving the deliberate introduction of one or more foreign elements into a host structure to modify its properties. This process typically induces desirable impurity-related effects that influence the defect landscape without altering the fundamental crystal structure. As a result, doping is generally performed at low concentrations to maintain the integrity of the base material [7, 13].

In NCM cathodes, three general sites can be substituted by a dopant atom, namely the lithium, oxygen, and TM sites [13] (Figure 2). The site a dopant occupies depends on its valency, ionic size and how the material is synthesised. When atoms that form strong bonds with oxygen occupy the TM or Li sites, they strengthen the structure. This added rigidity reduces changes in the crystal lattice during battery charging/discharging which limits oxygen loss and cation movement, which in turn decreases the rate of surface damage and electrolyte breakdown. For instance, adding 1.0 mol.% boron to NCM90 ($Li[Ni_{90}Co_5Mn_5]O_2$) has been shown to completely prevent microcracking after 100 cycles at 55 °C. However, the B-doped material showed slightly lower rate capability than the undoped version [13].

Previous studies show that Mg incorporation into the pCAM crystal structure can decrease cation mixing. The occupancy of Mg^{2+} (0.72 Å (when present) is predominantly in the Li sites [14]. Mg in low concentrations occupies both the Li and TM sites and creates a “stable pillar effect” by creating linkages across the inter-layer structure, stabilising the layered structure and helping to prevent structure collapse. Decreasing cation mixing increases the rate capacity and cycle performance. However, if the Mg concentration is too high, it can hinder Li diffusion during charging and discharging, resulting in poor rate capacity [8, 14].

Al is another widely studied dopant that tends to occupy TM sites, especially that of nickel. Studies have shown that strong Al-O bonds stabilise the cathode structure and improve charge transfer to oxygen, although it slightly inhibits Li diffusion [13].

1.3 Experimental Procedure

1.3.1 Reactor Configuration in continuous operation

The C4P is equipped with four parallel, purpose built, pCAM precipitation units, designed and constructed by hte, a subsidiary of BASF. These units are capable of operating in continuous, semi-batch and batch modes. In this activity, the continuous operation mode was utilised and is described below. The semi-batch and batch mode operations are discussed in later sections.

There are five storage tanks (Figure 6(1)) mounted on weightometers in each hte unit designated for supplying chemicals to the reactor (Figure 6(2)). Diaphragm dosing pumps transfer reagents based on feed tank mass loss, controlled via a programmable logic controller (PLC) shown in Figure 6 (3). The SCADA (Supervisory Control and Data Acquisition) software manages each pump's flow rate to user-defined values, dosing of chemicals by mass, controlling pH levels and keeps track of other parameters, enabling continuous data collection throughout the experiment. The chemicals, including TM solution, sodium hydroxide and ammonium hydroxide, are pumped into the reactor which is blanketed by nitrogen to prevent oxidation. Reactors are available in two sizes; 2.5 L and 8 L. 2.5 L vessels were used for all experiments unless otherwise stated. The start-up solution volume and composition are adjusted depending on whether the reactor is operated in continuous, semi-batch or batch mode and the reactor volume. When operated in continuous mode, a rotary table auto-sampler is connected to the reactor overflow, diverting the overflow to collection vessels for automated sampling at set times.

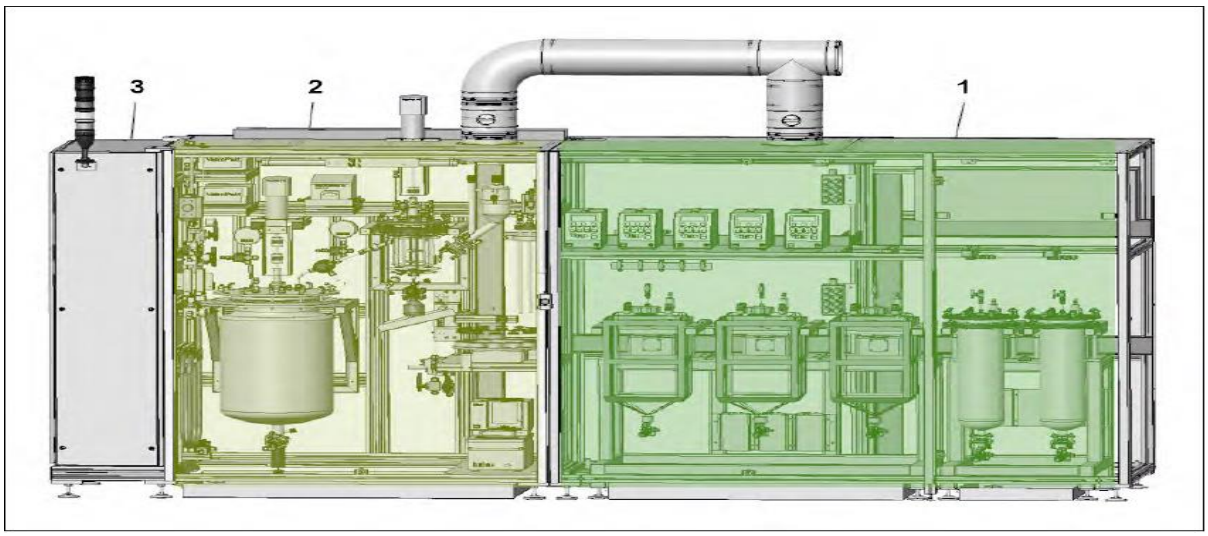

Figure 6 Precipitation Rig Structure; (1) Liquid/Reagent Rack, (2) Reactor Rack, (3) Electrical cabinet

In continuous operation mode, a reactor (Figure 7a) is connected to a nitrogen blanketed 50 L ageing tank (Figure 7c) via an overflow tube (Figure 7b).

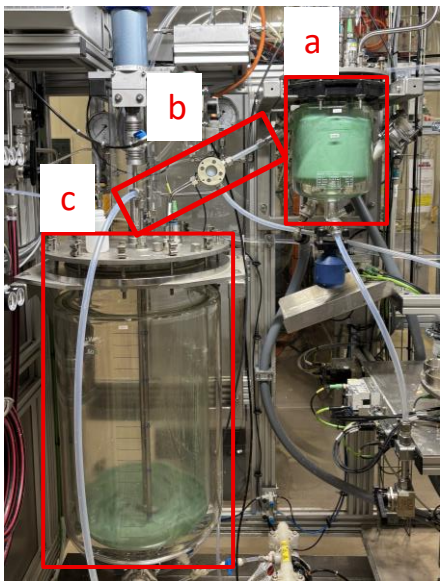

Figure 7 The hte unit operating in a continuous mode. a. reaction vessel, b. overflow tube, c. ageing tank

1.3.2 Preparation of $Ni_{0.83}Co_{0.12}Mn_{0.05}(OH)_2$ precursors in continuous mode

To prepare the nickel, cobalt manganese TM solution, with a molar ratio of Ni:Co:Mn = 83:12:5 (to produce $Ni_{0.83}Co_{0.12}Mn_{0.05}(OH)_2$), Ni solution was added to a feed preparation tank, with stoichiometric amounts of Co and Mn added, as well as DI water to dilute to a total metals concentration of 2 M, before extended mixing to ensure complete dissolution.

The preparation method for generating $Ni_{0.83}Co_{0.12}Mn_{0.05}(OH)_2$ precursors was based on conditions found to create material meeting target specifications during Stage 2 (conducted under the FBI-CRC) project activities. The reaction vessel within the hte precipitation unit was initially filled with DI water, blanketed with nitrogen gas, and heated to the target temperature using a circulating water bath. Ammonium hydroxide (as the chelating agent) and sodium hydroxide solution, and the TM solution were pumped into the reaction vessel, NaOH was automatically added, via a pump, to adjust the pH to the target value.

1.3.3 Characterisation

The morphology of the cathode precursor was observed by a Field Emission Gun Scanning Electron Microscope (FEG-SEM) coupled with Energy Dispersive Spectroscopy (EDS) for elemental mapping. SEM image samples were mounted on carbon coated stubs and carbon coated before analysis. Samples for EDS analysis were prepared by cold mounting in resin and carbon coated for analysis.

The elemental composition of solutions was determined by both Inductively Coupled Plasma-Optical Emission Spectroscopy (ICP-OES) and Inductively Coupled Plasma-Mass Spectrometer (ICP-MS).

Solid samples were digested before analysis using the same methodology as liquors. Selected product samples were also analysed via X-ray Fluorescence (XRF) Spectroscopy for cross-comparison.

The precursor particle size distributions were measured using a Malvern Mastersizer 3000.

The tap-density of the product was measured using a tap-density meter.

The BET surface area and BJH Pore Size were measured via Micromeritics Tristar II Plus instrument. Samples were degassed to remove adsorbed contaminants and moisture from atmospheric exposure prior to analysis. High-purity nitrogen gas was used to measure the surface area and pore size.

Crystal phase identification was carried out via X-ray powder diffraction. The analysis was performed using 10 wt.% alpha-alumina (corundum) addition to the samples to allow for investigation of peak position shifts associated with instrument and sample packing to be corrected for.

1.4 Results and Discussion

Figure 8 shows an SEM image of a typical sample produced. It was found that none of the elements tested had any measurable effect on particle size or tap density. Furthermore, it was shown that of the ten impurity elements tested, three remained in the solution and were not taken into product (within analytical accuracy). Given these impurities had no measurable effect on either physical or chemical properties of the product, it is postulated that their removal from battery grade chemicals is unnecessary, however this requires further validation through electrochemical testing of products.

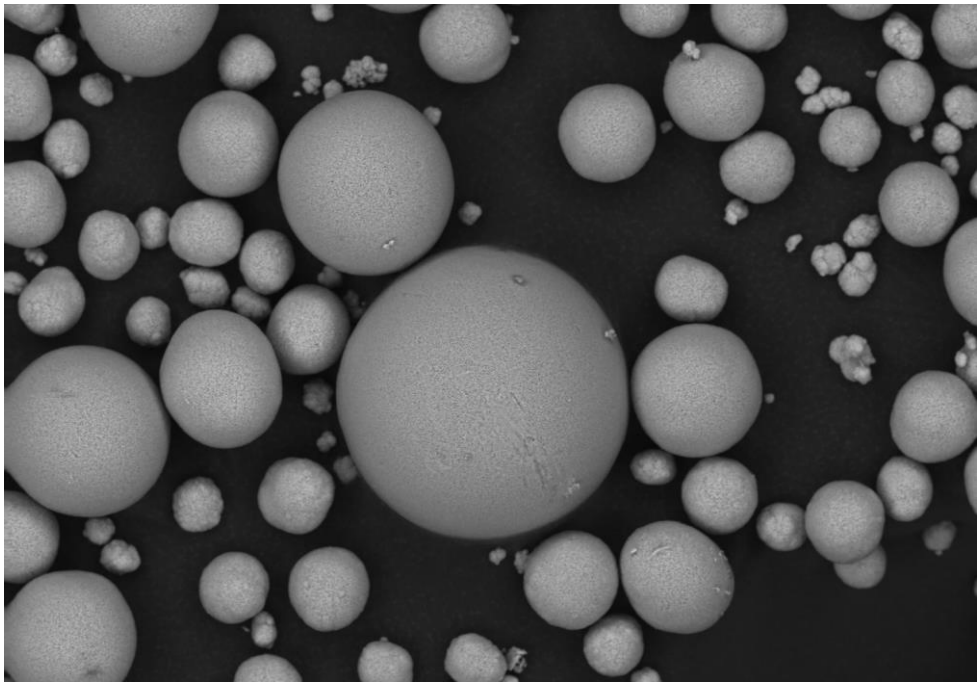

Figure 8 SEM images of one of the pCAM samples

Figure 9 shows the EDS mapping of one sample made without impurity inclusion. This technique was used to determine where the incorporated elements sit within the pCAM particles. In most cases impurity elements were found to be homogeneously distributed within the pCAM structure, indicating integration into the structure, rather than formation of a separate phase.

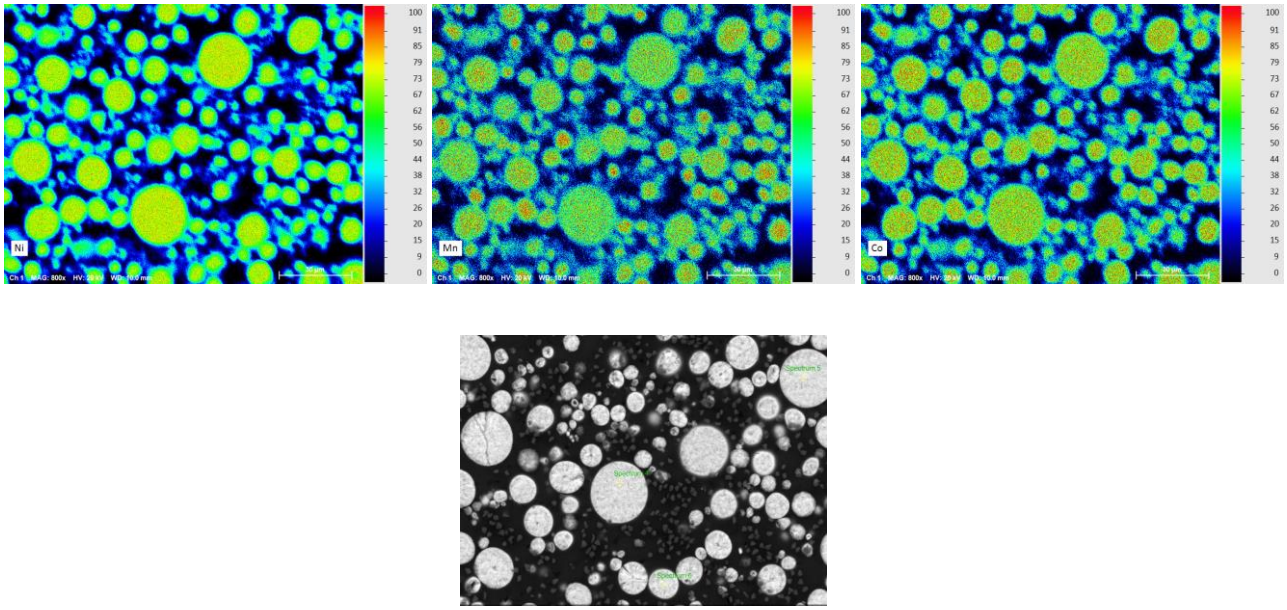

Spectrum (wt.%)	O	Na	S	Mn	Co	Ni
Spectrum 4	34	0.29	0.21	2.8	7.8	54
Spectrum 5	36	0.19	0.21	3.7	8.1	51
Spectrum 6	35	0.36	0.33	3.0	8.0	52

Figure 9 EDS and elemental mapping of pCAM product with no impurities added. All EDS data is uncalibrated and is comparative only, not absolute

The x-ray diffraction patterns of the pCAM products from Tests 2, 3, 4, 7 and 8 (tests with various impurities) are shown in Figure 10. Test 9 is included for comparison as on specification NCM without impurities. The identified crystalline phase for all tests is the single-phase of theophrastite, a layered nickel hydroxide β-Ni$(OH)_2$ with a P-3m1 space group. This confirms that the impurity elements taken up were fully incorporated into the structure and did not create any additional crystalline phases. Comparing the peak positions across all tests showed no significant peak shifts, indicating minimal changes in the crystal lattice parameters. A peak ratio change was observed around 83-84.6 degrees in Test 4. Further characterisation would be needed to determine which element/s are causing this lattice strain. A subtle peak shift was observed for Test 8, indicating similar crystal lattice strain and/or defects with the incorporated ion/s. A narrower peak was also observed at 83–84.6 degrees, which can be indicative of anisotropic changes in the crystal structure, including preferred growth orientation along a specific plane, anisotropic crystallite growth direction and selective relief of internal stress/strain/defects along only one specific crystallographic direction.

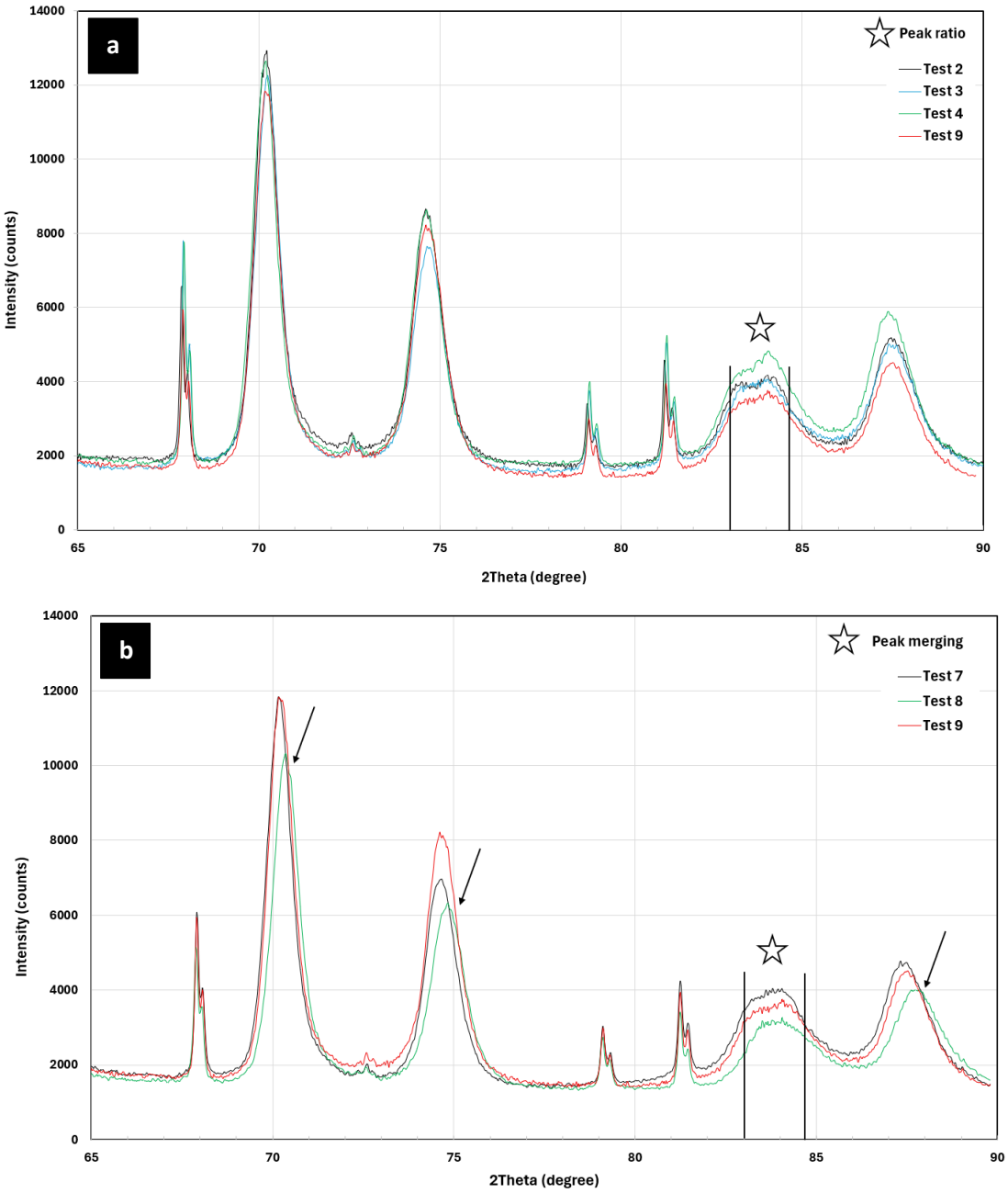

Figure 10 X-ray diffraction patterns of the solid pCAM products in the range of 65-90 degrees. A. Test 2-4 compared with Test 9 as the reference sample. B. Test 7 and 8 compared to Test 9

1.5 Conclusions

Elements that currently require removal if/when WA-based ores are processed to produce battery-grade chemicals were investigated. Of the ten elements tested, three had no detectable effect on physical or chemical properties of the pCAM produced.

A baseline sample (produced in the absence of impurities) and one produced in the presence of one of the impurities tested were electrochemically tested by Curtin University, with no significant difference in performance under the test conditions. This is strong evidence that these element can be rejected during pCAM production rather than requiring upstream removal from feed chemicals for them to be considered battery grade. This creates the opportunity to simplify processing and reduce costs within the battery material supply chain.

2 WA Processing Optimisation through pCAM Production Impurity Rejection

2.1 Introduction

Western Australia possesses mineral deposits containing all three required metals NCM cathode materials, yet, to date has not fully realised the potential value from this mineral endowment by midstream processing to value-added battery materials.

Modern NCM cathode chemistries are trending towards high nickel, containing 80-90 mol.% nickel (relative to total metal content), making nickel the primary value driver and a natural entry point for battery market participation. Furthermore, in WA's mining operations, cobalt is often produced as a byproduct of nickel processing.

The battery industry utilises high-purity crystalline nickel sulfate hexahydrate ($NiSO_4 \cdot 6H_2O$) as input for pCAM production, which is generally produced by further refining other conventionally produced nickel products (such as nickel metal or processing intermediates).

While WA has historically had a relatively high number of nickel mines and processing facilities, operations have been economically challenged in recent years due to depressed commodity prices. Most WA operations are currently in care and maintenance, driven by a combination rising energy and operating costs, and depressed nickel prices driven by intense competition from lower-cost overseas operations. Furthermore, only BHP's Kwinana nickel sulfate plant has yet gone as far downstream as to produce battery-grade nickel sulfate in WA, and it too is in care and maintenance. All other operations produce nickel intermediates or metal products, or otherwise simply ship concentrates offshore.

This lack of midstream processing to value-added products is not due to inadequate natural resources, but rather as a result of conventional 'battery-grade' specifications that require CAPEX-intensive refining infrastructure and OPEX intensive processes that, to date, most aspiring producers cannot economically justify. International pCAM producers have established stringent nickel sulfate purity standards – typically <10 ppm total impurities with sub-ppm limits on specific elements – that dominate global procurement. These specifications appear to be derived from conventional solvent extraction based purification pathways, rather than validated cathode performance requirements, yet they function as de facto market gatekeepers. Meeting them requires multiple intensive purification cycles that substantially increase capital costs, operating expenses, energy consumption, and carbon emissions.

The result is that WA exports low-value intermediates, and increasingly struggles to do so, while international refiners capture the value-added from battery-grade chemical production and the rest of the downstream battery value chain. Resource ownership doesn't translate to supply chain participation, leaving WA locked out of the fastest-growing segment of nickel demand despite possessing the raw materials to supply it. Beyond the economic and supply chain security factors, there are also ESG considerations; cathode materials represent the largest environmental impact in battery production, yet the supply chain's specification regime may exclude viable lower-impact alternatives while perpetuating market concentration among established refiners.

Our preliminary assessment examined how demonstrated impurity rejection during pCAM production challenges conventional specification requirements. The findings suggest that certain

purification steps, costly, energy-intensive, and currently considered essential, may be unnecessary when nickel sulfate feeds directly into integrated pCAM production. This opens a pathway for WA processors to compete not by replicating current refining practices, but by implementing optimised flowsheets tailored to local ore characteristics and integrated operations, capturing cost and carbon advantages while building domestic battery chemical capability.

2.2 Understanding Nickel's Path to Batteries

Before examining opportunities for optimisation, it's important to understand how nickel reaches the battery supply chain, and why current pathways create barriers for Australian producers.

2.2.1 Different Ore, Different Routes

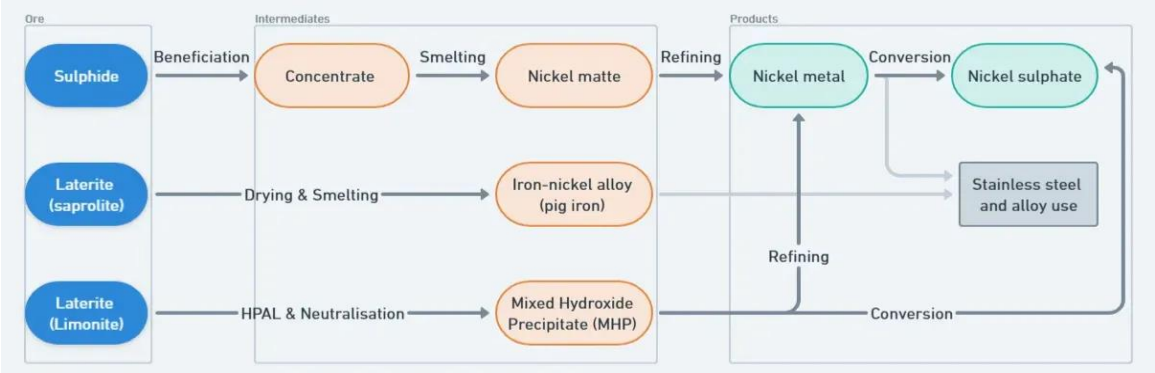

Figure 11 Simplified commodity-focused flowsheet showing pathways of nickel from ores to intermediates and products [3]

Nickel occurs in two distinct ore types (sulfides and laterites) that require fundamentally different processing approaches.

Laterite ores are low grade surface deposits rich in oxidised minerals. They dominate global reserves with limonites closer to the surface (low Ni, high Fe, with Co) and saprolites slightly deeper within the deposit [15] (high Ni, low Fe), Figure 12.

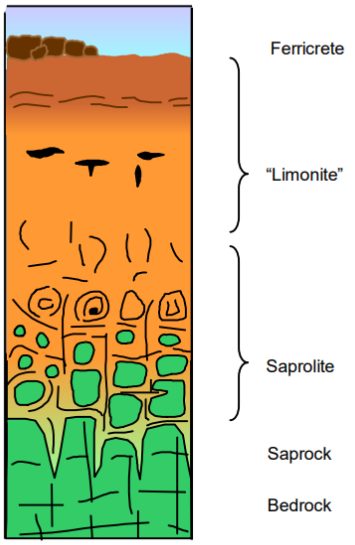

Figure 12 Schematic laterite profile developed on ultramafic rock [15]

Limonites undergo hydrometallurgical processing – high-pressure acid leaching (HPAL) to produce Ni-Co intermediates like mixed hydroxide precipitate (MHP) for refining to metal or conversion to nickel sulfate. Some recent facilities, such as Ravensthorpe, employ enhanced acid leach processes (EPAL) combining HPAL with atmospheric saprolite leaching using recycled acid [16].

High-grade saprolite deposits are processed pyrometallurgically by calcining and smelting dried ore to produce Fe-Ni alloy (nickel pig iron) [17]. Traditionally used for stainless steel, rising battery demand has driven the conversion of this alloy to nickel matte for further refining to nickel metal then onto nickel sulfate. In January of 2020, the Indonesian government implemented a ban of all raw nickel ore exports. Since then, there has been significant investment in smelting and refining infrastructure within Indonesia, resulting in a rapid increase in production. This has subsequently depressed nickel market prices, however, in general, this production has high carbon intensity due to the smelting technology and a significant reliance on coal-based energy.

Sulfide ores occur from surface to deep underground, often carrying valuable copper, platinum, and palladium alongside nickel. Sulfide deposits offer processing advantages as these ores concentrate readily at the mine site into shippable product, unlike laterites that requires moving large tonnages of low-grade material. WA's sulfide processing was developed to target alloy and electroplating markets through pyrometallurgical routes – smelting concentrates to nickel matte and in some cases further processing to metal. Converting these products to battery-grade sulfate requires expensive downstream processing.

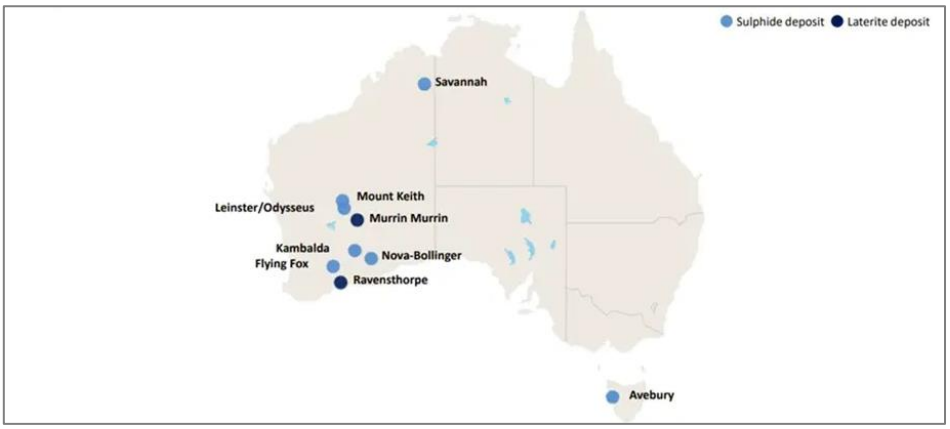

Figure 13 Locations of Australia's nickel mines [18]

2.2.2 The Refining Bottleneck

Nickel supply chains traditionally served electroplating and alloy production (predominantly stainless steel), using intermediates like MHP or refined nickel metal. Nickel-based battery chemistries emerged relatively recently and, to date, have not been a large enough market for supply chain optimisation, resulting in minimal integration. Consequently, nickel sulfate is typically produced by converting existing nickel materials, either nickel intermediates (such as MHP) or refined nickel products (nickel metal).

Currently, producing battery-grade nickel sulfate requires not just chemical conversion but extensive purification. This conventionally involves solvent extraction (SX) steps to selectively load and strip specific elements onto organic phases, including a dedicated cobalt separation despite cobalt's value in cathode material [19], Figure 14.

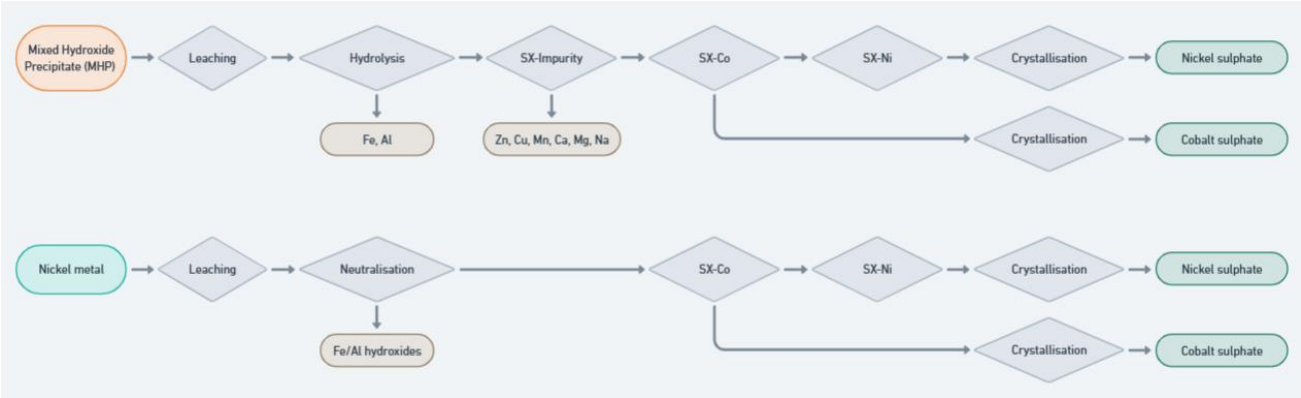

Figure 14 Conventional processing pathways to battery-grade nickel sulfate crystals

The nickel purification step (SX-Ni) represents a particular cost burden. Unlike impurity removal where only trace elements transfer to the organic phase, SX-Ni must load all nickel present between 50-100 g/L, versus <1 g/L for impurities, onto the organic phase (consuming base for pH control), then strip it back to aqueous phase (consuming acid). At bulk concentrations, this represents a substantial expense as it consumes large quantities of reagents and generates waste streams that require management.

2.3 Opportunities for Production Route Optimising

2.3.1 Leveraging Impurity Rejection During pCAM Production

C4P research examined impurity behaviour during pCAM coprecipitation to assess whether conventional battery-grade nickel sulfate specifications impose unnecessary processing requirements. The findings suggest that certain elements are not incorporated into the pCAM structure, potentially enabling significant upstream process simplifications with substantial cost savings and environmental impact reduction.

Relaxed specifications may also enable meaningful reductions in water quality requirements. Eliminating the requirement for high purity water in pCAM production would facilitate water recycling and process circularity while reducing operating costs. More speculatively, this may extend to alternative water sources, though substantial validation of tolerance limits for all elements in any alternative sources would need to be verified.

2.3.2 Vertical Integration Opportunities

Supply chain fragmentation imposes real costs through processing inefficiencies, where every section of the supply chain must make a profit rather than the chain as a whole. Processors must invest in intensive purification to meet specifications that may exceed battery production requirements. Nickel and cobalt are separated into individual products despite being recombined for NCM production. Nickel sulfate is crystallised for shipment, then redissolved by pCAM manufacturers. Each step adds cost, energy consumption, and carbon emissions without conclusively improving final battery performance.

Vertical integration of nickel processing directly into pCAM production represents a substantial strategic opportunity for Australian producers when combined with relaxed specifications based on demonstrated impurity rejection. Rather than conforming to generic international specifications designed for diverse ore types and fragmented supply chains, integrated partnerships can develop tailored specifications leveraging WA's specific ore mineralogy and processing capabilities. This approach recognises that impurity profiles and optimal processing routes vary between deposits, which may allow Australian producers to compete based on their specific advantages rather than attempting to replicate foreign production systems.

An artifact of legacy supply chains rather than technical necessity, separation of nickel and cobalt into individual refined products becomes unnecessary for materials for NCM cathode production. Vertical integration or collaboration between refiners of nickel sulfate and pCAM producers, may allow the elimination of this solvent extraction stage, SX-Co, with its associated capital costs, reagent consumption, and operational complexity.

Following this, the crystallisation of nickel and cobalt sulfate products is an energy intensive process which, in some cases, could be avoided in more integrated operations. While crystallisation can have some technical benefit as a method of purification, it is primarily utilised in conventional supply chains to reduce the mass required for transport and storage. Even after crystallisation however, the hexahydrate product of nickel sulfate still contains only 22% nickel by weight, making it an inefficient commodity to transport. Since pCAM production requires aqueous nickel and cobalt sulfate solution, crystallisation, if often only done for transport, represents processing inefficiency with no technical benefit. Eliminating crystallisation removes capital equipment, ongoing energy costs, and handling steps.

2.4 Potential Impact and Competitive Advantages

Western Australia has specific advantages for integration of the battery materials supply chains; high-quality nickel ores with favourable metallurgy, established mining infrastructure, political/policy stability, renewable energy for low-carbon processing, and proximity to Asian battery manufacturing markets. Rather than competing directly with established refiners using the same technologies, a WA-optimised approach for nickel sulfate production into pCAM could deliver substantial economic and environmental benefits. This approach treats specifications as process-dependent variables rather than fixed constraints, allowing tailoring to local feedstocks and locally integrated processing, ensuring more value is captured within the Australian economy. This work identified several viable pathways to more efficiently process from both sulfide and lateritic nickel deposits to pCAM with significantly lower capex and opex than has been achieved previously. While these process improvements are not currently being disseminated publicly, the C4P team are happy to discuss further with interested parties.

3 Development of Batch Operation Mode Capability

3.1 Introduction

The hte pCAM precipitation units utilised in the C4P facility are capable of operating in either a batch or continuous mode, with only continuous mode utilised in previous work conducted under the FBI-CRC. This activity aimed to develop the capability to run the hte units in batch mode. Where continuous operation achieves steady production through ongoing feed input and simultaneous product removal, batch operation processes fixed quantities of reactants in a closed system with no material removal until completion. Each of these operating modes comes with intrinsic advantages; continuous operating systems require smaller equipment for a given production rate, leading to lower capital costs, whereas batch operations allow for greater quality control (as each batch can be analysed and controlled separately) and a greater ability to clean equipment and perform maintenance between each batch, allowing for greater product quality control.

While it is believed there is a global industry trend towards continuous operation for mass production, batch operation is still used industrially for pCAM production [20]. Developing the capability and know-how to produce pCAM in batch and semi-batch modes is valuable for two reasons; Australian industry may well choose to take this approach of operating in batch mode as, in addition to the advantages listed above, it results in a product with slightly higher energy density.

For research and development being able to test conditions in a batch system, can expedite work by enabling faster testing while using fewer resources (e.g. staff-hours, reagent use). During this activity it was found that attachment of a slurry concentrator system onto a batch reactor configuration enables semi-batch operations which offers further advantages to standard batch mode.

3.2 Literature Review

3.2.1 Batch vs continuous hydroxide coprecipitation

Coprecipitation can be conducted in batches or continuously using different reactor configurations. The most commonly used reactors for commercial coprecipitation processes are a Continuous Stirred-Tank Reactors (CSTR), where reactants flow into the reactor and products are discharged at a constant rate, with the system reaching a steady state condition. At the laboratory scale, coprecipitation is often conducted in batch reactors which are closed systems in which reactants are added, and the reaction proceeds for a set time, however, the reaction in the batch reactor does not necessarily reach a steady state [21].

In coprecipitation, several factors, such as the reactant input rate, reaction temperature, duration, pH, solution concentration and stirring rate influence the synthesis process. One key advantage of the coprecipitation method is its ability to control particle shape and size [21]. Hydroxide precipitation is cost-effective for large-scale production, scalable and widely used in industry, offers precise control over particle morphology and compositions. However, it requires precise control of pH, temperature and chemical concentrations [9, 21].

Careful regulation of the nucleation and growth rates of the particles is essential to produce high-quality products. One strategy to improve these factors is to increase the solid hold-up (pulp density) in the reactor by modifying its design. Figure 15 shows a design of a new, gas-liquid-solid three-phase separation system reported in literature, namely, siphon and gravity sedimentation equipment, to separate crystalline solid particles from the spent liquor after the chemical reactions. This multiphase separation system can achieve continuous reactive crystallisation by continuously feeding reactants into the reactor, and discharging of the clear spent liquid after precipitation. This slurry concentrator system integrates various functions including separation and exhaust of entrained gas and sedimentation and circulation of solid particles allowing for discharge of clear spent liquor. This circulation of the solids allows particles to grow to a desired size in the crystalliser. Thus, it can overcome some of the technical limitations associated with the fixed volume of the reactor to more easily generate high-quality precursors at lab scale. In addition, by continuously feeding the reactive crystalliser until the product meets the quality requirements, the solid concentration in the reactive crystalliser significantly increases, with pulp densities greater than 1300 g/L achievable, which is conducive to refining the spherical morphology of the product and further enhancing the electrochemical performance of the cathode materials. Previously reported morphologies of precursors with high and low solid holdups are shown in Figure 15 [22].

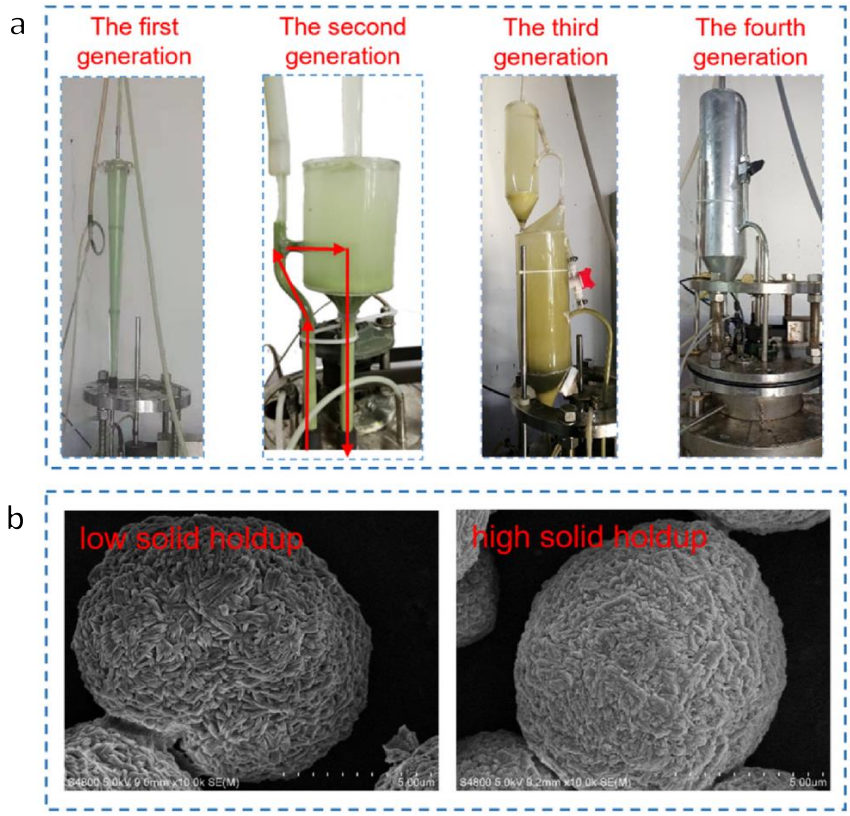

Figure 15 Solid concentration systems a. Four generations of sedimentation separation equipment for preparing ternary cathode precursors. b. Scanning electron microscopy images of different precursor morphologies at high and low solid holdups [22]

3.3 Experimental Procedure

3.3.1 Materials

The Ni, Mn and Co sulfates used were as per described in section 1.3.2.

3.3.2 Preparation of $Ni_{0.83}Co_{0.12}Mn_{0.05}(OH)_2$ precursors in Batch mode

Transition Metal solutions were prepared following the process stated in Section 1.3.2, however no impurities were added.

3.3.3 Reactor Configuration in Batch Mode

For batch tests the outlet port of the reactor is sealed with a plug, which is differentiated from a continuous reactor configuration where there is an overflow tube to the ageing tank and autosampler. A manual sampling tube was installed in lieu of the autosampler, with samples drawn via a syringe. The reactor sizes used in this activity were 2.5 L and 8 L. For all tests, the reaction vessel was pre-purged with nitrogen.

Figure 16 An 8 L reactor in batch mode with the overflow port blanked

3.3.4 Standard Batch Tests with 2.5 L reactor

Twenty-three batch tests were undertaken using a 2.5 L reactor without a settling arm ('standard' batch mode configuration). For each test, the reaction vessel was initially filled with 700 mL of dilute ammonium hydroxide solution, as this was found to be a reasonable compromise between having minimum volume in the reactor while still having acceptable agitation at startup. All tests were operated for 24 hours in total with chemical addition time and ageing time varied. Hourly samples were collected during the work shift, with the final sample collected 24 hours after test commencement.

3.3.5 Standard Batch Tests with 8 L reactor

Three batch tests were conducted using an 8 L reactor. The 8 L reactor, aside from the bigger reactor volume, has a different reactor geometry and a modified impeller configuration. The start-up

solution volume used in both vessels was chosen by visual inspection of the system during water commissioning, so that the solution mixing was as high as possible while minimising splashing, bubbles and vortex effects.

3.3.6 Reactor Configuration in Semi-Batch Mode

Semi-batch tests were conducted in a 2.5 L reactor with a settling arm attachment which serves as an integrated slurry concentrator. The settling arm allows removal of clarified spent liquor from the reactor while retaining precipitated particles in the reaction vessel. By continuously creating space in the reactor for the addition of further fresh liquor, the reactor volume and concentrations can be maintained for continued precipitation, allowing for many of the benefits of a continuous test, such as greater particle growth to be achieved with similar levels of resourcing as a batch test.

The capability development and performance evaluation of a 2.5 L reactor fitted with a slurry concentrator was conducted and continuously refined through five ‘semi-batch’ tests.

3.3.7 Characterisation

Samples were characterised by PSD, SEM, tap-density, ICP-OES and ICP-MS using the same instruments and methodologies as specified in section 1.3.3.

3.4 Results and Discussion

The team was successful in generating material which met all target specifications (tap density, particle size, chemical composition and structure) utilising the semi-batch mode of operation. Additionally, conversion factors were identified to translate test conditions from batch to continuous systems and vice versa, allowing for rapid prototyping in batch/semi-batch conditions before conversion to a continuous system, to allow for more rapid test work to be conducted.

As expected, the batch products exhibited less spherical morphology, with an example shown in Figure 17, however it had a higher tap density and a size distribution with lower span.

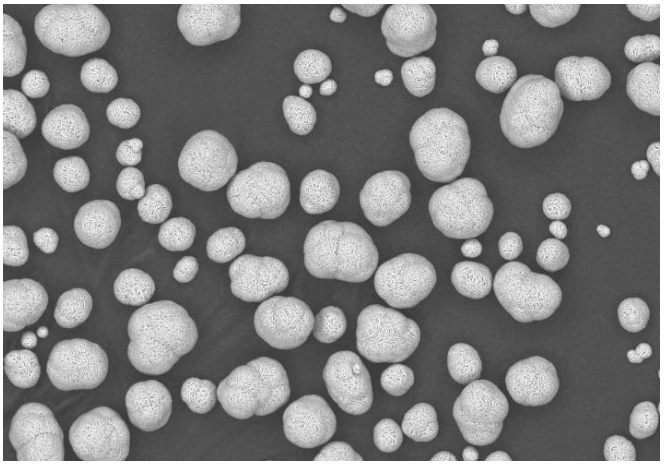

Figure 17 SEM image a semi-batch produced product

3.5 Conclusion

A total of 30 tests were conducted for this research activity, comprising standard batch tests in 2.5 L and 8 L reactors as well as semi-batch tests. While standard batch tests did not directly produce on-specification products, this work provided essential learnings that enabled the team to achieve on-specification products using semi-batch conditions.

Semi-batch tests using a slurry concentrator allowed for the removal of spent liquor from the reactor and addition of fresh liquor to continue the reaction, increasing both the particle size and the tap-density of the final solids.

Semi-batch operation combines the advantageous start volume of continuous operation with the intensified timeframes and reduced reagent usage of batch processes, while theoretically unrestricting residence time and enabling higher reactor hold-up for enhanced particle growth.

4 Development of Alternative pCAM Chemistries

4.1 Introduction

There are various lithium-ion battery chemistries used commercially, with selection informed by parameters such as cost, energy density, output voltage, life span and safety. To date, most commercial interest for Australian production of battery materials has been focused on Ni, Co and Mn chemistries due to their high performance and significant market share. The development of capabilities to produce alternative pCAM chemistries beyond NCM is essential for Western Australia to remain competitive in the rapidly evolving global battery market. One of the promising alternative chemistries in the current battery market, that also aligns with WA resources is NCMA (Ni, Co, Mn and Al). Incorporating Al has been shown to increase structural stability, which allows for an increase in Ni and reduction in Co concentrations within the pCAM structure, resulting in higher specific charge densities. This inclusion of Al suppresses the multistep phase transitions of Ni-rich materials upon delithiation (battery charging), while reducing the cost of batteries with lowering Co concentrations [20]. For this activity, multiple NCMA pCAM chemistries were produced, characterised, and compared with the previously discussed reference pCAM.

4.2 Literature Review

4.2.1 Compositions beyond NCM811 pCAM

State-of-the-art LIB cathode materials are evolving toward compositions that exceed NCM811 in nickel content. The relationship between Ni content, discharge capacity and thermal stability in ternary Ni, Co, Mn materials is shown in Figure 18. As the Ni content increases (accompanied by reductions in Co and Mn), the discharge capacity improves. However, this enhancement comes at the cost of diminished thermal stability. Notably, a sharp increase in discharge capacity, coupled with a decrease in thermal stability, is observed when the Ni content increases from 85% to 90% [23]. This highlights both the opportunity and the challenges in producing Ni-rich NCM materials.

Doping is considered an effective strategy for mitigating degradation, and its importance increases as the nickel content is increased [20, 24]. Discharge capacity, capacity retention and thermal stability of NCMs with different Ni compositions are shown in Figure 18 [13].

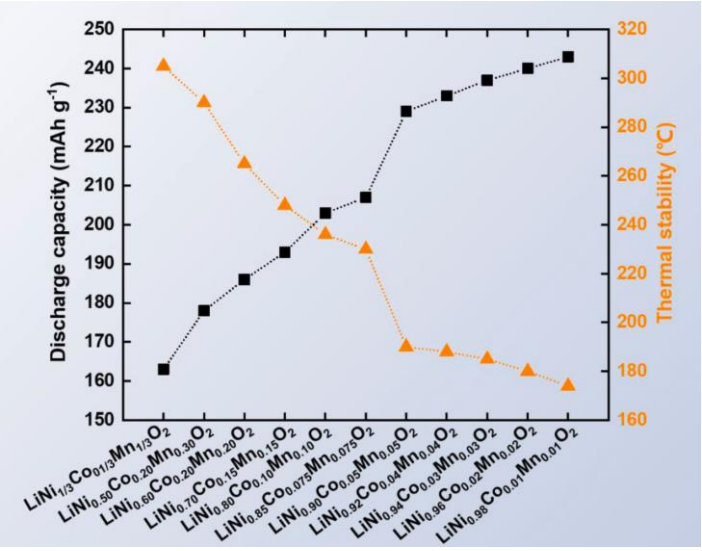

Figure 18 The diagram of the relationship between Ni content, discharge capacity and thermal stability in the NCM ternary material [20]

4.2.2 Doped Al effects on Ternary NCM systems

Doping refers to the deliberate introduction of impurity elements into a material to enhance the characteristics of that material. For cathode materials, the characteristics targeted by dopant addition are; conductivity, stability, capacity and structure which improve battery performance. Typically, doping is performed at levels not exceeding 1% of the total host TM atoms, enabling controlled modifications of material characteristics without significantly affecting overall structure. However, in certain cases, concentrations of up to 5% may be utilised to more strongly influence the behaviour of active materials. Even minimal amounts of dopant can lead to significant changes in the structure of lithiated oxides and their electrochemical properties. It is essential to determine an optimal dopant concentration, as excessive doping may cause detrimental effects that outweigh the intended benefits. Adding small amounts of elements such as Al, Ti or Mg to the cathode improves structural stability and prevents phase transitions during cycling. However, too much doping can reduce available sites for Li^+, lowering capacity and overall cathode performance [11].

One of the best doping candidates is Al as it forms stronger bonds with oxygen due to increased bonding energy (Al-O; 512 kJ mol^{-1}) when compared with Ni, Co and Mn in NCM cathode (Ni-O; 391.6 kJ mol^{-1}, Co-O; 368 kJ mol^{-1}, Mn-O; 402 kJ mol^{-1}). This enables a robust lattice structure as oxygen gas evolution is minimised. Moreover, Al is less electronegative than TM ions in the NCM cathode. This property also enables Al to form stronger bonds with lattice oxygen [25].

In the context of layered ternary materials, transition metal elements fulfil distinct roles and demonstrate notable complementary effects in their contributions to energy storage performance. A radar chart is shown in Figure 19 to highlight the respective advantages and limitations of the Ni, Co, Mn and Al elements. A high concentration of Ni ions provides high capacity and rate capability, thereby increasing the volumetric and mass energy density. Increased Co ion content can enhance the electronic conductivity of cathode materials and reduce cation mixing, improving rate performance and discharge specific capacity. While Mn and Al ions do not participate directly in electrochemical reactions during lithiation and delithiation (discharging and charging), they help stabilise the layered structure and increase safety in high-nickel cathode materials by mitigating multistep phase transitions in Ni-rich substances during delithiation. The addition of Al to NCM 80:15:5 contributes to the stability of structural, electrochemical and thermal properties of the cathode. Al substitution reduces anisotropic lattice changes during cycling, maintains greater

interlayer thickness for Li^+ diffusion and elevates the onset temperatures of phase transformations during heating. Furthermore, the abundance of Mn and Al helps lower the cost of LIBs [20].

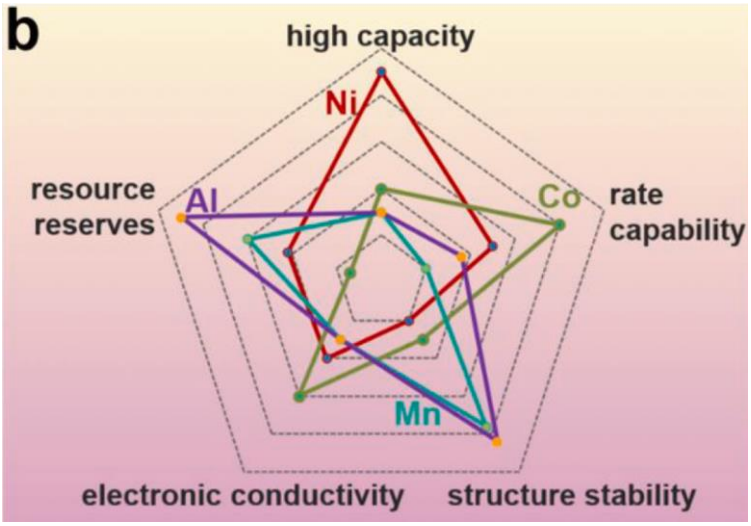

Figure 19 The role of Ni, Co, Mn and Al in NCM ternary cathode materials and the elemental resources reserves [20]

4.3 Experimental Procedure

4.3.1 Materials

The Ni, Mn and Co sulfates used were as described in section 1.3.2. Aluminium sulfate hydrate $Al_2(SO_4)_3 \cdot xH_2O$ (9% Al) was used as the Al precursor in the TM solutions.

The hte units were operated in continuous mode using a 2.5 L reactor as per section 1.3.1. Likewise, TM solution preparation was the same as section 1.3.3, however instead of impurities, Al was added. The stochiometric amounts of Ni, Co, Mn and Al based on their molar ratios differed between tests.

The pH and ammonium hydroxide to TM molar ratios were increased as nickel concentration was increased as it was found in C4P stage 2 (conducted under the FBI-CRC), higher Ni concentrations generally require higher pH and ammonium hydroxide to TM molar ratios.

4.3.2 Characterisation

Samples were characterised by PSD, SEM, tap-density, ICP-OES, ICP-MS, XRF, XRD, EDS and BET using the same instruments and methodologies as specified in section 1.3.3.

4.4 Results and Discussion

pCAM materials with both 87 and 89 mol.% nickel were successfully synthesised with the addition of Al. Electrochemical testing of these materials is yet to be conducted. Images of the synthesised material is shown in Figure 20. As expected, the addition of aluminium resulted in a slight decrease in tap density.

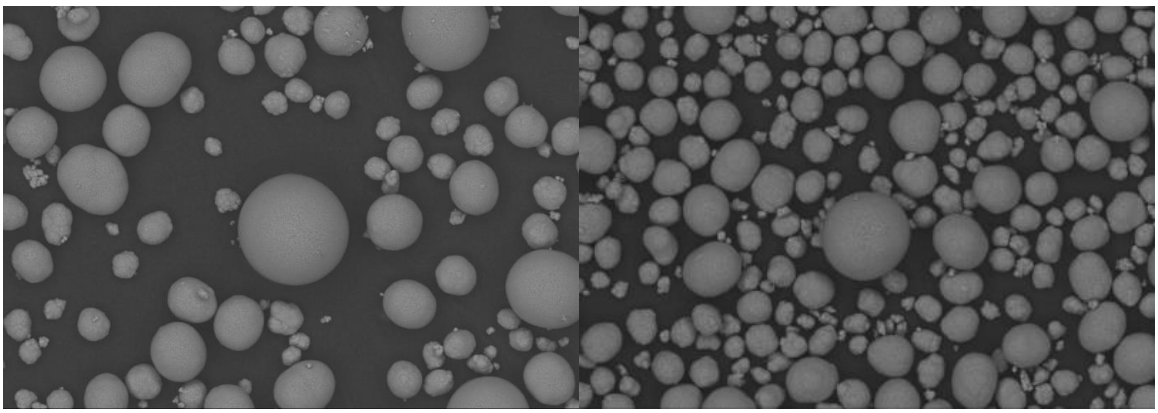

Figure 20 SEM images of high nickel NCMA pCAM products at two different magnifications

EDS and elemental mapping of NCMA products show a strong presence of Ni, Co and Mn as expected, with Al evenly distributed within the particles. There was also no evidence of secondary phase generation.

4.5 Conclusions

Seven tests were conducted within this activity with differing NCMA pCAM chemistries, altering the Al, Ni and Co content. The results indicated that high nickel materials were successfully generated, however this is pending confirmation via electrochemical testing.

5 Preliminary CFD Model of pCAM Precipitation Reactor

5.1 Introduction

This chapter presents work undertaken as part of a PhD student project at Curtin University, commenced under the FBI-CRC. The data from the pilot plant experiments conducted in previous project stages have been used in this activity to calibrate and validate a CFD model of the reactor system. The model was partially developed in stage 2, but validation and parametric studies were conducted during stage 3. NCM pCAM is mainly produced in the CSTR by a reactive precipitation process [26]. It is important to have a fundamental knowledge of the coprecipitation process to be able to scale up the process to produce precursor material. Due to the complexity of the process, it is important to simulate the system to save time, raw materials, and make it cost-effective. To design a mixing model, it is important to study the hydrodynamics of mixing, which can predict the concentration distribution of species in different environments, at different times and locations within the reactor [27]. Coupling the Computational Fluid Dynamics (CFD) with the Population Balance Model (PBM) can be used to predict PSD, and we can calculate the mean crystal size of particles [28]. To study the size-dependent growth in coprecipitation environments, the population balance model coupled with the quadrature method of moments (QMOM) provides good results to predict PSD [28].

Growth Mechanism

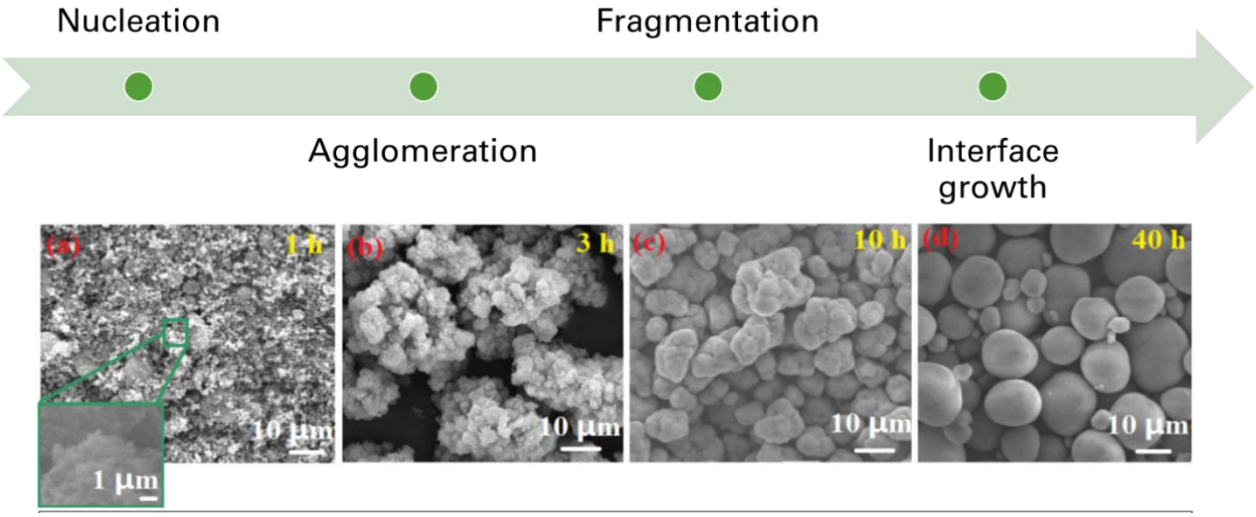

Figure 21 SEM images of NCA precursors prepared under various reaction times at a NH3H2O concentration of 0.5 mol L-1 (a-d) [29]

The precipitation process for the growth mechanism can be broadly classified into four categories: Nucleation, agglomeration, fragmentation/interfacial growth, and interface growth, as shown in Figure 21 [29].

The first process in the precipitation of a solute is nucleation. Nucleation can be further divided into two parts: Primary nucleation and secondary nucleation. Primary nucleation also has two types: homogeneous and heterogeneous nucleation. Homogeneous primary nucleation is the spontaneous formation of nuclei in the absence of any solids, such as seed crystals or impurities. Heterogeneous primary nucleation refers to the nucleation of solute onto existing solids, like impurities [30]. Purely homogenous nucleation is difficult to achieve due to the presence of solids (even the container/reactor wall materials can serve as heterogeneous nucleation sites). Secondary nucleation requires the addition of a secondary solid. pCAM nucleation is classed as primary nucleation.

5.1.1 Hydrodynamic effect on particle size and morphology

The structure of pCAM material is highly affected by ammonia concentration in the reactor because it acts as a complexing agent that inhibits the nucleation rate and increases the growth rate [29]. The inlet position of the feed pipe should be placed close to the impeller to save energy. The flow has a huge impact on the crystal size, dendritic shape-like particles observed for a high feed rate of reactants, and cuboid-shaped particles observed for a low feed rate of reactants [31]. Mixing has a huge effect on particle size; small sized particles can be observed with high intensity mixing [31]. Whereas Lee and co-workers [32] have investigated the precipitation of metal hydroxides under various operating conditions and found that particle size distribution and morphology are significantly influenced by key parameters such as pH, the concentration of the chelating agent (aqueous ammonia), stirrer speed, etc. The precipitation kinetics are significantly affected by local supersaturation.

5.1.2 Coprecipitation Modelling for NCM-hydroxide

Micromixing model

The probability (volume fraction) of an environment is defined as the concentration of species in that environment at a certain time and spatial position. We can divide this into three feed environments, namely; TM, sodium hydroxide, and ammonia feeds. The fourth environment is where precipitation occurs [26]. The probability of a multi-feed environment decreases as the mixing from the precipitation environment, and the concentration of the feed environment are assumed constant for the micromixing model [26]. The feed environment probability can be tracked by equation (1) [33].

$$\mathbf{u}_f \cdot \frac{\partial p_i}{\partial \mathbf{x}} = \frac{\partial}{\partial \mathbf{x}}\left(\frac{C_\mu}{Sc_t}\frac{\kappa^2}{\varepsilon}\frac{\partial p_i}{\partial \mathbf{x}}\right) - C_f \frac{C_\emptyset}{2}\frac{\varepsilon}{\kappa}\, p_i\left(1 - p_i\right) \qquad \text{for i} \in (1,2,3) \qquad (1)$$

where p_i is the volume fraction of the environment i, ε and κ are the turbulent kinetic energy and dissipation rate. Sc_t is the turbulent Schmidt number and C_μ is an empirical constant. C_f and $C_\emptyset$ are defined as modelling coefficients. If the flow is characterised as a high Reynolds number, the value of $C_\emptyset$ is assumed to be 2. Though Lui and Fox [34] argued that the selected value overestimates the micro-mixing rate for Sc = ν/Γ >> 1 (i.e. for liquids). u_f defines the velocity of the particle, like the fluid velocity (as the particle size is very small, we assume they are going to follow the fluid flow, without affecting it).

5.1.3 Precipitation governing equation

For very small particles and low-volume fractions, it can be assumed that the particles follow fluid direction without disturbing fluid flow. The moment of order k is defined by [26].

$$m_k = \int_0^\infty L^k n(L)\, dL \tag{2}$$

where L is particle size

The first five moments of order are of interest (k = 0,1,2,3,4) because they are useful to find:

(a) Total number particle density (N_t)= m_0,

(b) Total particle area (A_t) = k_a m_2,

(c) Total solid volume (V_t) = $k_v m_3$,

where k_a, k_v are area and volume shape factors, respectively [28].

Supersaturation is defined by the ratio of the activity coefficient of involved species to the solubility product of metal oxides [30].

$$S = \sqrt[3]{\frac{\left(a_{Ni^{2+}}\right)^{0.8}\left(a_{CO^{2+}}\right)^{0.1}\left(a_{Mn^{2+}}\right)^{0.1}\left(a_{OH^-}\right)^2}{\left(k_{Sp}^{Ni(0H)_2}\right)^{0.8}\left(k_{Sp}^{Co(0H)_2}\right)^{0.1}\left(k_{Sp}^{Mn(0H)_2}\right)^{0.1}}}, \tag{3}$$

where α = the activity of the species and K_{sp} = the solubility product of metal hydroxide. The equation is for $N_{0.8}C_{0.1}M_{0.1}$, but it can be modified for other NCM chemistries. The activities were calculated using theoretical values by solving non-linear equations as explained by Shiea and others [26]. These non-linear equations come from the chemical equilibrium equations, as shown in Table 2, and are used to solve for ion concentration. Whereas solubility can be taken from the experimental values.

The growth rate (G) and nucleation rate (J) are defined by [27].

$$\mathrm{G} = k_{\mathrm{G}}\,(\mathrm{S}\text{ -}1) \tag{4}$$

Where S = supersaturation, k_G = modelling coefficient.

Nucleation rate (J) is defined by [27]

$$\mathrm{J}\,(\mathrm{S}) = k_1 \exp\left(\frac{-B_1}{(\ln S)^2}\right) + k_2 \exp\left(\frac{-B_2}{(\ln S)^2}\right) \tag{5}$$

Where B_1,B_2,k_1, and k_2 are modelling coefficients, and S is the supersaturation. In the above equation first term on the right side of the equation denotes homogeneous nucleation, and 2nd term denotes heterogeneous nucleation.

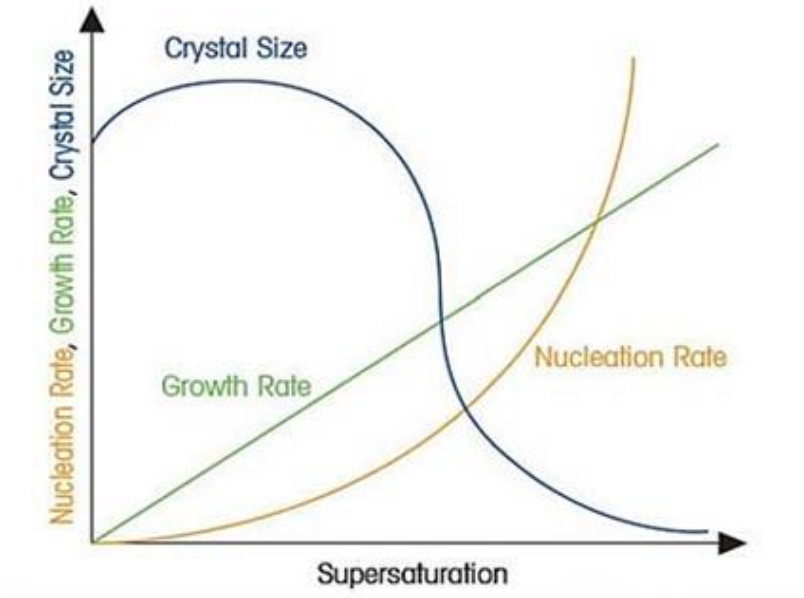

Figure 22 Nucleation rate, Growth rate and Crystal size with respect to supersaturation [35]

The dependency of supersaturation on growth rate and nucleation can be seen in equations 4 and 5. Figure 22 shows that the growth rate increases linearly with an increase in supersaturation, and the nucleation rate increases exponentially with an increase in supersaturation.

The values of the modelling coefficients for nucleation growth and agglomeration are not provided in the literature, and it is also important to tune them for this system.

5.1.4 **Chemical Equilibrium**

The iterative Newton-Raphson method adapted to a system of equations can be used for solving the equilibrium equation [36]. For equilibrium calculation, no activity coefficient was included. Because at high basic (pH > 10) conditions, deviations from ideal are minimal and do not materially influence equilibrium outcomes. Self-ionisation of water becomes negligible under such strongly basic conditions, so it does not affect the calculated concentrations involved in coprecipitation, and ammonia decomposes insignificantly under equilibrium conditions. And for the lack of data on the activity coefficients of metal-ammonia complexes, it is assumed the activity of metal ions is similar to that of metal-ammonia complexes due to the same charges. Although, to calculate supersaturation the activity coefficients are included [27].

5.1.5 **Activity Coefficient**

To calculate the activities of each metal hydroxide, $M(OH)_2$, the following equation is used [26]:

$$a_{M^{2+}} (a_{OH^-})^2 = [\,M^{2+}][OH^-]^2\,\gamma_{\pm}^3 \qquad (6)$$

Where, $\gamma_{\pm}$ is the mean molal activity coefficient. The mean molal activity coefficient of metal and hydroxide ions in the solution can be calculated by adopting Bromley's method [37]. The effect of ammonia on the activity coefficient is neglected [26].

5.1.6 Calculation step for simulation

Figure 23 shows the simulation steps, where we first freeze the flow field by using water in the system. Later, all the UDS are solved simultaneously by using these frozen flow fields to get all the moments. Then the moments are used to reconstruct the PSD.

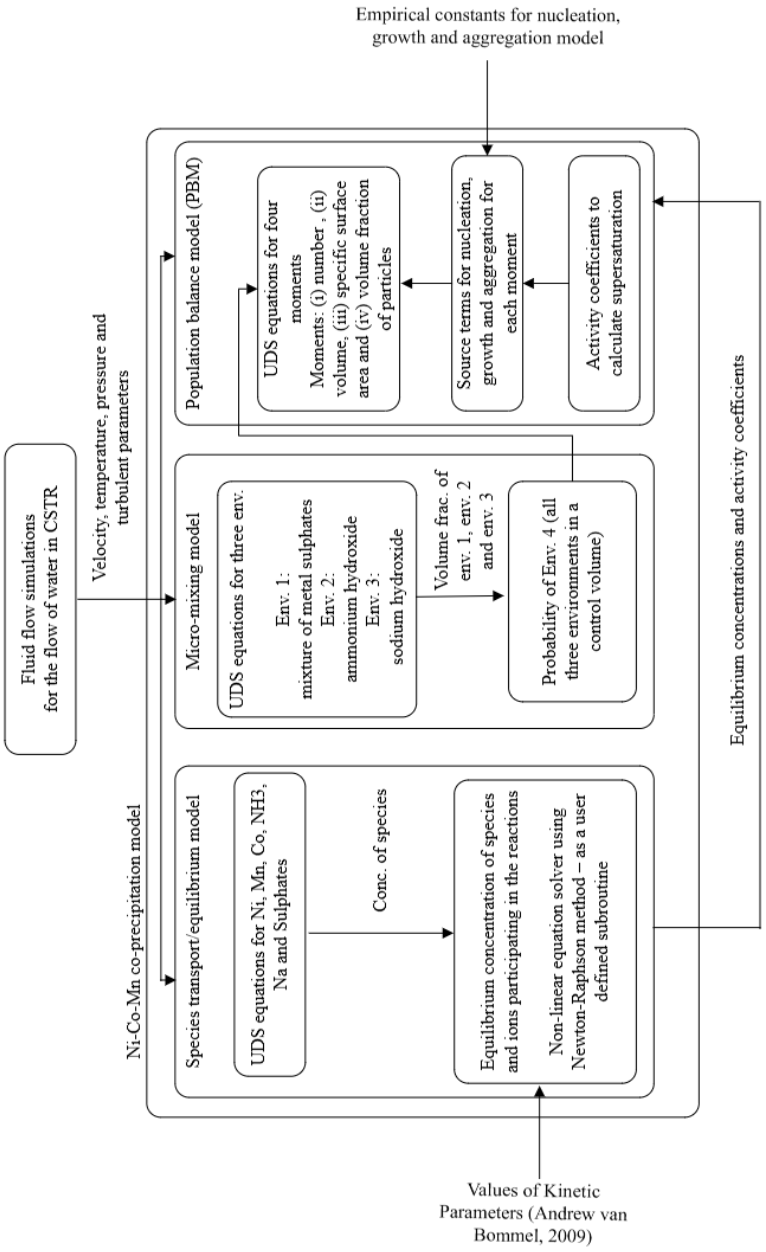

Figure 23 Calculation step for simulation

5.1.7 **Objective**

The objectives for this Activity were:

- Develop a mixing model with a population balance model for the precipitation of Precursor to facilitate PSD predictions that will help to forecast product quality, optimise operating conditions, and reduce experimental effort.
- Model validation with experimental data.
- Predicting the effect of operating conditions on PSD.

5.2 Methodology

5.2.1 **Experimental Studies**

The main reaction involved in the coprecipitation of NCM is given as:

$$TMSO_4 + 2\,NaOH + (NH_4OH + H_2O) \rightarrow TM(OH)_2 + (NH_4OH + H_2O) + Na_2SO_4 \quad (7)$$

Note: The portion in the brackets reflects spectator species that influence the reaction at the precipitation rate and determine the overall medium for the reaction, but they are not consumed or generated in the reaction itself.

The equilibrium reactions involved in the process are given in Table 2.

Table 2 Equilibrium reaction involved in the crystallisation process of NCM [38]

Reactions		Log k		
		Ni	Mn	Co
$M_i^{2+} + NH_3 \rightleftharpoons [M_i(NH_3)]^{2+}$		2.81	1.00	2.10
$M_i^{2+} + 2\,NH_3 \rightleftharpoons [M_i(NH_3)_2]^{2+}$		5.08	1.54	3.67
$M_i^{2+} + 3\,NH_3 \rightleftharpoons [M_i(NH_3)_3]^{2+}$		6.85	1.70	4.78
$M_i^{2+} + 4\,NH_3 \rightleftharpoons [M_i(NH_3)_4]^{2+}$		8.12	1.3	5.53
$M_i^{2+} + 5\,NH_3 \rightleftharpoons [M_i(NH_3)_5]^{2+}$		8.93		5.75
$M_i^{2+} + 6\,NH_3 \rightleftharpoons [M_i(NH_3)_6]^{2+}$		9.08		5.14
$M_i^{2+} + 2\,OH^- \rightleftharpoons M_i(OH)_2$	Log k_{sp} =	-15.22	-12.70	-14.89
$NH3 + H2O \rightleftharpoons NH4+ + OH-$	Log k_b =	-4.80	-4.80	-4.80
$H2O \rightleftharpoons H+ + OH$	Log k_w =	-14	-14	-14
Note: In the reactions, Ni and Co form all six complexes with ammonia, but Mn forms only the first four complexes. Where, i = 1,2,3 and $M_1^{2+} \equiv Ni^{2+}$, $M_2^{2+} \equiv Mn^{2+}$, $M_3^{2+} \equiv Co^{2+}$				

All data used in this activity were generated during Stage 2 of the project under the FBI-CRC program. The same dataset was used for model calibration and validation. A summary of the experimental conditions is provided in Table 3.

Table 3 The experimental operating conditions N.B test numbers refer to stage 2 tests

Test no.	NCM	NH_3/TM ratio	Agitation Intensity	Feed Flow regime
29	811	High	High	Controlled
31	811	Medium	High	Controlled
32		High	Very High	Reduced
7		Medium	Low	Controlled
18		Medium	Moderate	Controlled
22	622	Medium	High	Controlled
21		Low	Moderate	Controlled

5.2.2 **Modelling**

Figure 24 (a) shows the geometry of the reactor, which was used for simulation predictions. There are a few assumptions that were taken into consideration to reduce the complexity of the system and the model. Like:

1. pH probes: Due to the system's complexity, it's appropriate not to include pH probes while designing the geometry. It helps in designing a geometry with a neat mesh.
2. Steady state solver: The process is complex, and it solves multiple equations simultaneously. So, to lower computational time and computational power, we only solved time-independent equations.
3. Moving reference frame motion: The reason for choosing MRF over Moving mesh is to reduce computational time and computational power, where MRF uses a steady state approximation by keeping the mesh stationary and solving the flow in a rotating frame.
4. Single-phase fluid flow: It is assumed that the solid particle formed during pCAM production will follow the fluid path without affecting it, due to the very small size (micrometres) of the particles.

5.2.3 **Characterisation Techniques**

Product Characterisation (PSD) was performed using a Malvern Mastersizer 3000.

5.3 Results and Discussion

5.3.1 **Mesh independence**

Experimental and numerical torque data were generated using a water-based system. Mesh sensitivity was evaluated using two computational grids of increasing resolution within an MRF modelling framework. Simulations were performed across a range of impeller speeds to enable comparison between measured and predicted torque values.

Applied torque is the torque acting on the rotating components. In contrast, the received torque corresponds to the reaction torque predicted on the stationary walls, as reported in Table 4 and Table 5.

Table 4 Torque data from experiments and simulation predictions for different impeller speeds

Stirrer speed	Experimental torque	Simulation predictions (N cm)	
		Applied torque	Received torque
Low	Low	Moderate	Lower
Medium	Moderate – high	High	Moderate
High	High	Very high	High

Table 5 Torque data from experiments and simulation predictions for different grid size

Mesh Resolution	Experimental torque	Simulation predictions (N cm)	
		Applied torque	Received torque
Lower resolution	Moderate	Higher	Lower
High resolution		Moderate	Lower

As the impeller speed increases or introduce more turbulence to the system, the simulation results deviate more from experimental results, as shown in Table 5.

Torque value is high for higher rpm can be due to over estimation of stress by turbulent model near the wall or due to choosing MRF motion that also over-predict torque at high rpm. The geometry with a larger number of cells gets a closer value to the experimental value. Furthermore, a grid size of approximately 0.1 million cells was used for subsequent simulation.

5.3.2 **Flow predictions**

Figure 24 shows the velocity magnitude on the vertical sectional plane, in which Figure 24 (a) shows contour plots and Figure 24 (b) shows the velocity vector. It is seen that the highest magnitude of velocity is at the impeller surface because of the rotation of the impeller. And the direction of fluid flow is different for both the impellers due to their design, one is forcing the fluid to flow downwards, and the other in an upward direction. Ultimately, the fluid is flowing towards the wall of the reactor and forming two vortices.

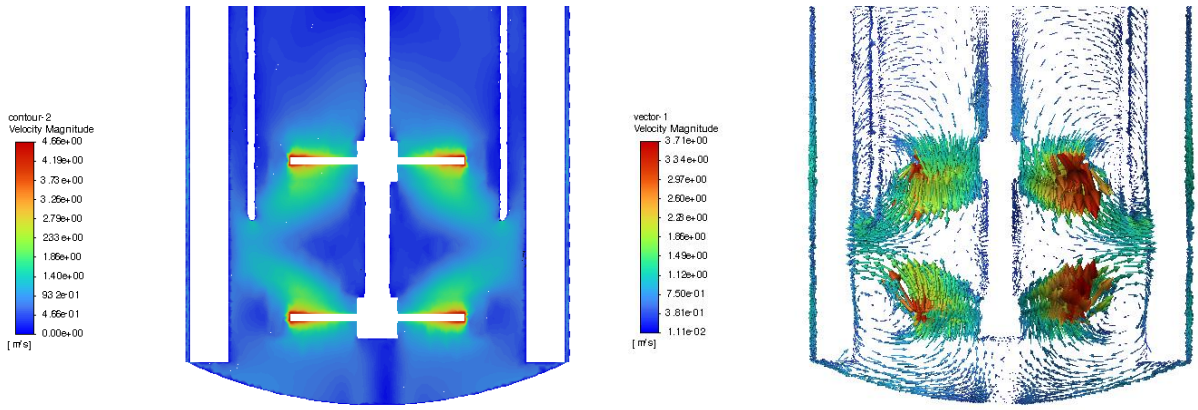

(a) (b)

Figure 24 Velocity magnitude (a) Contour plot, and (b) Vector plot

Figure 25 illustrates the pressure contour inside the reactor on the vertical sectional plane. A higher-pressure contour can be seen between two impellers because of fluid interaction at high velocity.

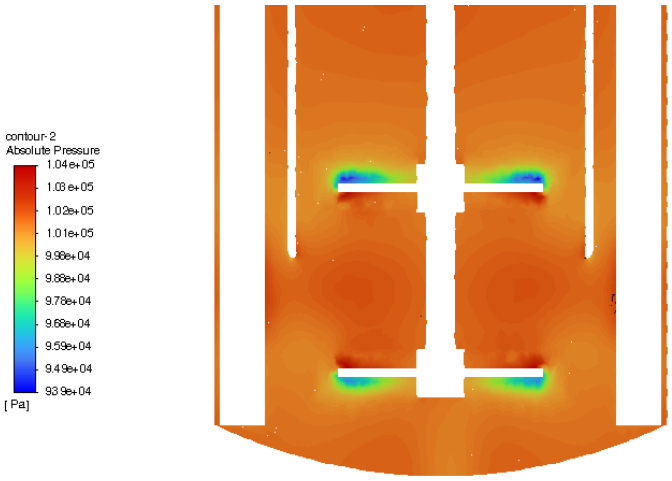

Figure 25 Contour of absolute pressure

Figure 26 shows the supersaturation and nucleation rate contour on the inlet horizontal plane and vertical plane. A very high supersaturation zone around the inlet of the TM feed solution, as shown in Figure 26 (a). The reaction zone is the supersaturation zone that is conical in shape and moves towards the reactor wall from the inlet pipe. And Figure 26 (b) shows the nucleation rate within the reactor. As expected, the nucleation rate is highest in regions with elevated supersaturation, consistent with the trend explained earlier.

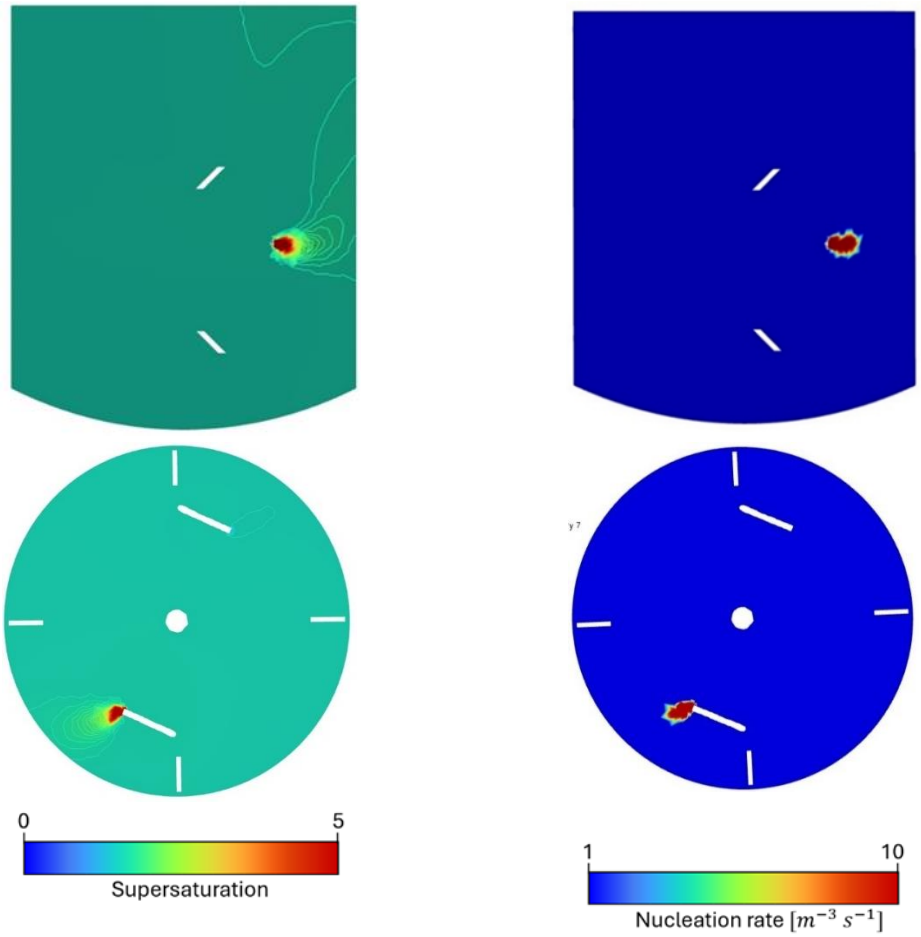

Figure 26 Contour plots on the inlet vertical and horizontal plane (a) Supersaturation, and (b) Nucleation rate

5.3.3 **Tuning of modelling coefficients**

The initial parameters of modelling coefficients for nucleation, growth, and agglomeration were adopted from the User-Defined Functions (UDFs) [26], which were implemented as the starting point of model calibration and subsequent sensitivity analysis.

Model calibration was performed using experimentally measured data described in the preceding section. Following initial calibration, the nucleation, growth, and agglomeration coefficients were systematically varied to evaluate model sensitivity and their influence on predicted mean particle size. Exactly calibrated parameters values are no reported due to project confidentiality restrictions.

Before tuning the parameters, the mean crystal size (d4,3) is 0.216 µm, which is significantly less than the experimental results. Then, one parameter was varied at a time to see the impact of different parameters on the mean crystal size, as shown in Figure 27 and Figure 28.

Figure 27 illustrates that with a decrease in the value of k_G and Ap, the mean crystal size increases, but the change is minimal.

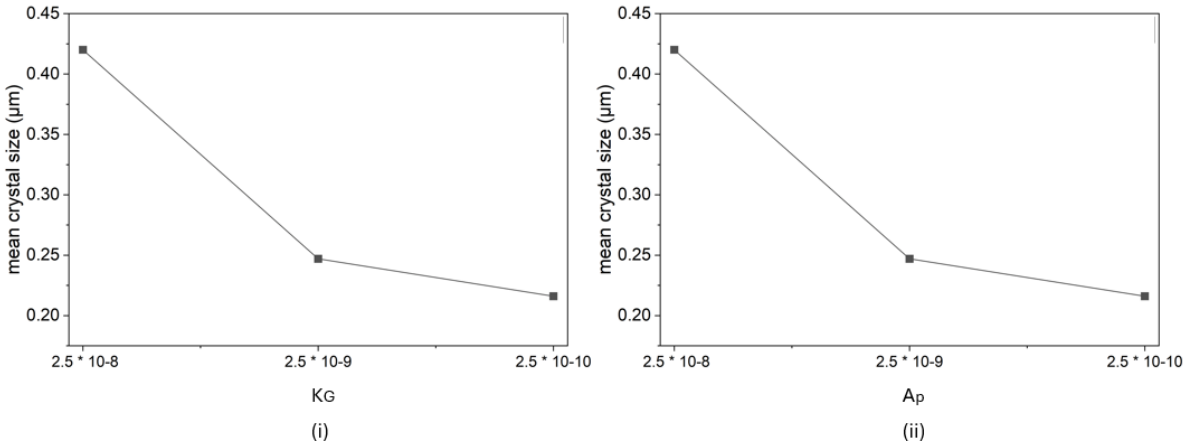

Figure 27 Effect of (i) Growth modelling coefficient (kG) and (ii) Ap from Agglomeration on mean crystal size

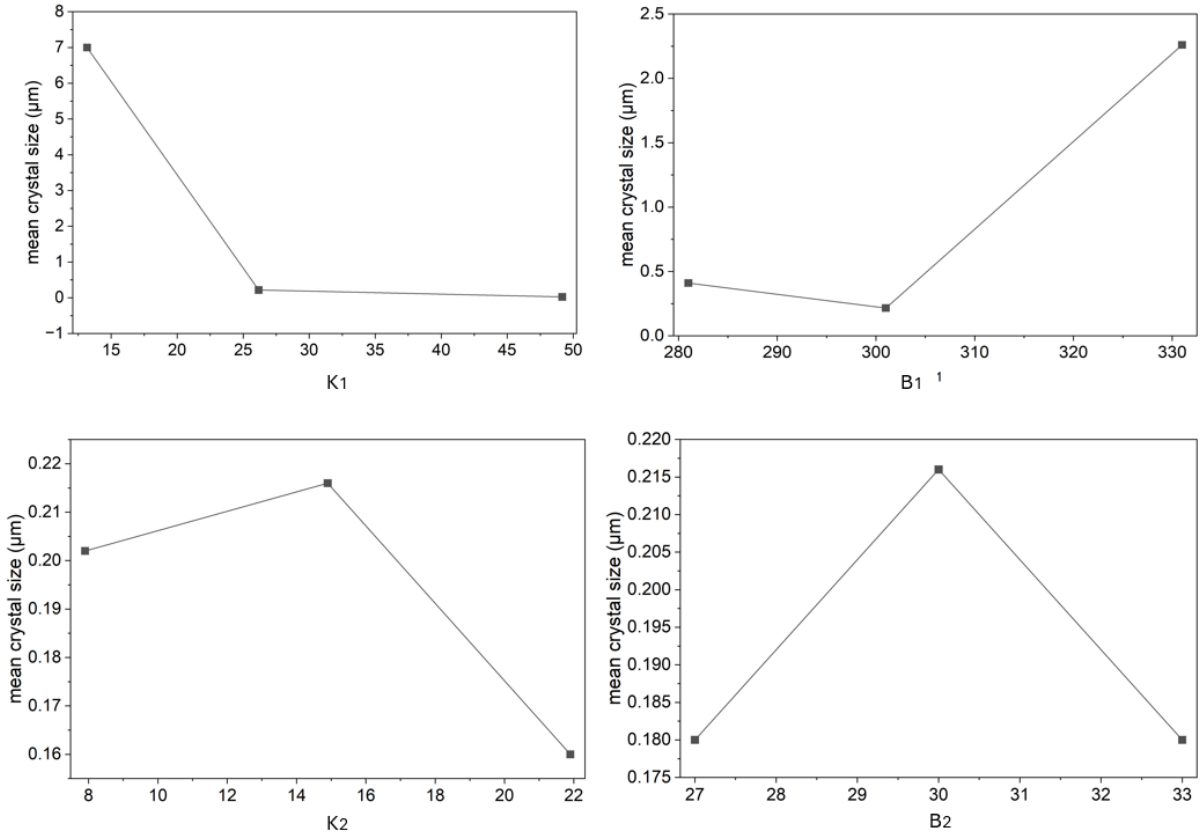

Figure 28 Effect of nucleation modelling coefficient (K1, B1, K2 and B2) on mean crystal size

Figure 28 shows the effect of nucleation modelling coefficient on d4,3. With a decrease in K1 and an increase in B1 values, there is a significant increase in the mean particle size. Whereas with the variation of K2 and B2 values, the change is negligible. With this observation, it can be said that the first term on the right-hand side of equation (5) is more dominant than the 2nd term. This indicates that the homogeneous nucleation is overpowering the heterogeneous nucleation for our system.

The effect of supersaturation values was modelled from a very high supersaturation value to a very low; these values of supersaturation are obtained from the simulations. These values are used in equation (5) to evaluate the effect of modelling parameters on nucleation rate. The nucleation rate shown in the graph is the log10 value of the actual nucleation rate.

Figure 29 shows that at very low supersaturation, varying B1 or K1 have no effect on nucleation rate, but nucleation rate does change with a change in K2 and B2. At very high supersaturation, K1 has a large effect on nucleation rate as compared to B1, whereas K2 and B2 only effect the nucleation rate slightly at very low values of K1.

Figure 29 Effect by varying K1 & B1 with increasing supersaturation (left to right) and K2 & B2 (top to bottom) on nucleation rate

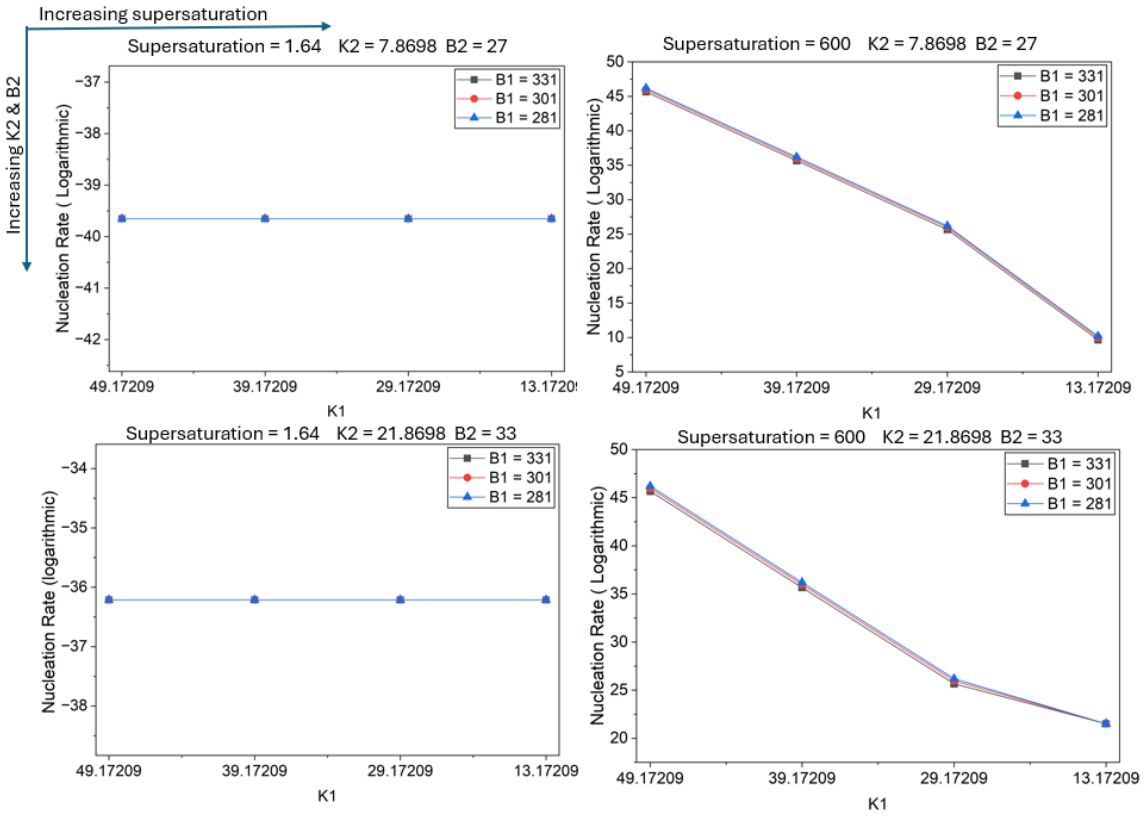

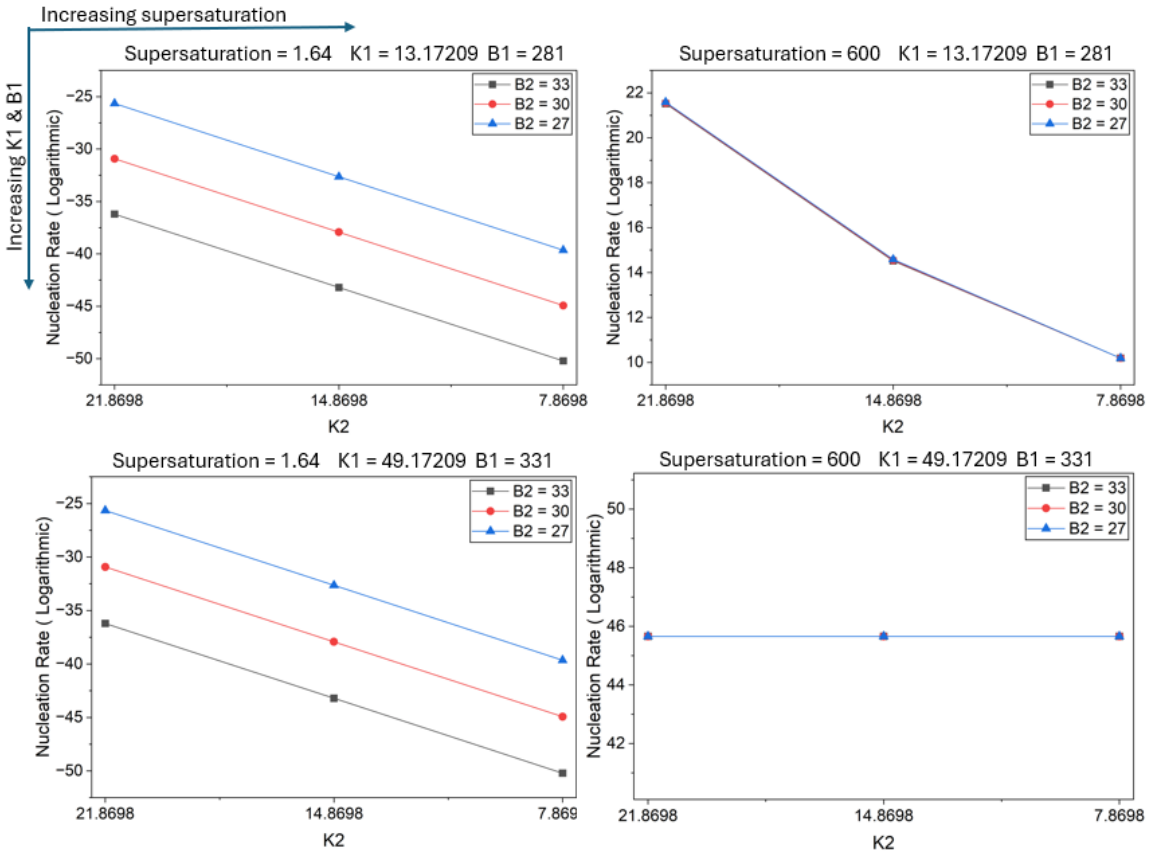

Figure 30 Effect by varying K2 & B2 with increasing supersaturation (left to right) and K1 & B1 (top to bottom) on nucleation rate

Figure 30 shows that at low supersaturation, K1 and B1 have no effect on nucleation rate, but with decrease in the K2 values results in a lower nucleation rate, whereas a decrease in B2 increases nucleation rate. But for high supersaturation, nucleation rate decreases with a decrease in the K2 value where whereas B2 values have no effect. However, for very high values of supersaturation, K1 and B1 show no effect on nucleation rate when K2 and B2 are varied.

Using the selected set of calibrated model parameters, the predicted mean crystal size was within 1 µm of the experimentally measured value obtained under the corresponding operating conditions, indicating good agreement between experimental observations and model predictions, demonstrating that the adopted parameter set provides a reliable representation of the system behaviour within the scope of this study.

5.3.4 **Model Validation**

The d4,3 from the pilot plant is calculated by taking an average of the close and repeated values, as the process is continuous and it operates from 4 to 12 days.

Simulated values for mean crystal size are close to the experimental results with very little discrepancy. It confirms that the model is trained and can be used to predict PSD for different operating conditions.

5.3.5 **Effect of TM concentration and impeller speed on PSD**

The effect of TM concentration on PSD (d4,3 and d3,2) is illustrated in Figure 31. It can be said that with a decrease in inlet TM concentration, d4,3 and d3,2 increase. Whereas an increase in concentrations show a high peak and a narrow PSD, indicating that the particle size is uniform and most of the particles are close to the average size of particle.

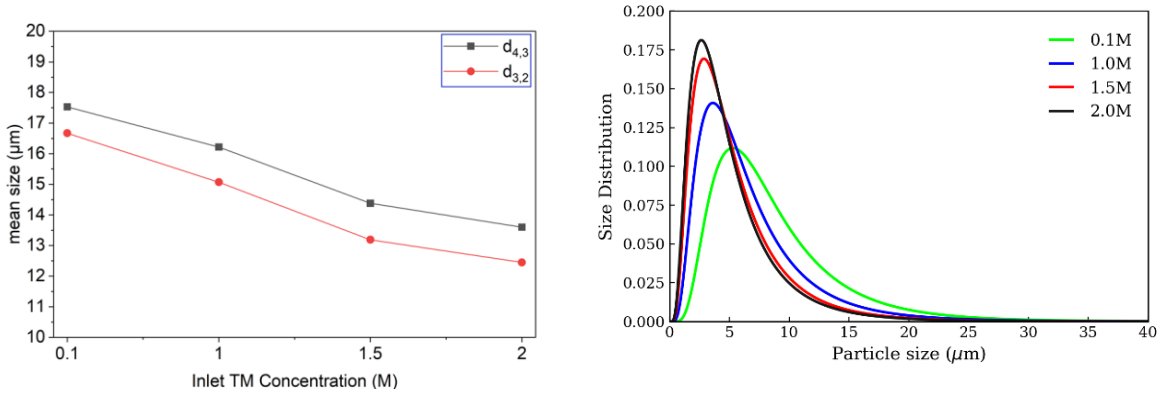

(a) (b)

Figure 31 Effect of TM concentration on (a) d4,3 and d3,2, (b) PSD

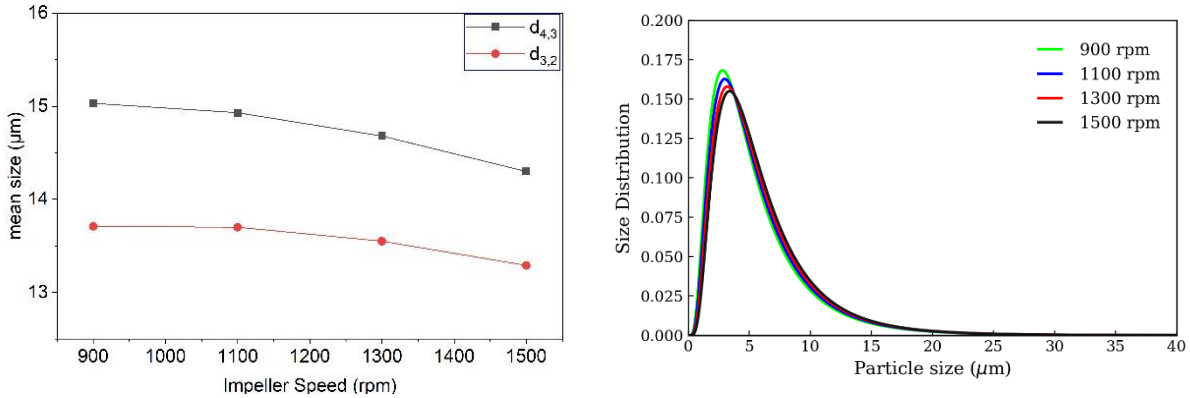

(a) (b)

Figure 32 Effect of impeller speed on (a) d4,3 and d3,2, (b) PSD

The effect of impeller speed on PSD (d4,3 and d3,2) is shown in Figure 32. It is visible that the effect of impeller speed on particle size is very small or negligible, however this may just be the result of not including the breakage model.

Conclusion and Recommendations

In this Activity, a CSTR geometry was defined, and the mesh validated with experimental torque data gathered through experiments. A detailed parametric study of modelling parameters for nucleation, growth and agglomeration was conducted to develop a CFD-PBE-based model. Interrogation of this model concluded that the homogenous nucleation mechanism is dominant in this system as compared to heterogeneous nucleation.

Model predictions were quantitatively compared with experimentally measured particle size characteristics to assess predictive capability. Agreement between simulated and experimental PSD trends was used to evaluate model performance and guide calibration of the modelling coefficients.

The effects of the TM concentration and impeller speed were examined. The PSD is highly affected by TM concentration, but the impeller speed is predicted to have little effect.

Further development of the model should include a breakage model to accurately predict PSD, further validate the model with a secondary data set and determine the effect of other experimental parameters such as TM/Ammonia ratio and residence time on particle size distribution. A different type of reactor or impeller design could also be studied in the future. It is also recommended to subtract torque in air to account for motor and bearing losses, which will ensure more accurate comparisons between experimental and simulation torque values for future studies.

This model can be used to simulate pCAM production processes and scale-up. This model can provide a prediction of the PSD expected for any reactor size, however further validation would be required.

6 Automated Analysis Techniques

6.1 Introduction

6.1.1 Background

This chapter presents work undertaken as a Master's student project at Curtin University. Like any process, pCAMs need to meet certain specifications to be able to be used in lithium-ion batteries, two of these specifications are particle size and particle sphericity. As the electric charge primarily travels along the surface of the electrode structures, it is important that the pCAM particles have a smooth surface without cracks and are spherical to prevent the build-up of charge in dips and on sharp edges. There is also a correlation between particle size and energy and power density with small particles corresponding with a high energy density and large particles corresponding with a high-power density [39]. Particle sphericity is currently determined through qualitative assessment of SEM images by trained scientists. This means that for every plant there needs to be at the very least one trained analyst per plant or the images will need to be sent to a third party for analysis. Out of the available options the first is by far the preferred method as it greatly reduces the turnaround from image acquisition and the delivery of results by having a dedicated analyst.

Computer program image analysers are being used in many industries including medical imaging [40], environmental monitoring [41], tunnelling [42], sediment analysis, steel manufacturing [43] and additive manufacturing [44-46]. These techniques were implemented to improve the efficiency of the production of results and remove the bias that the differences between analysists and the circumstances affecting them such as tiredness at the end of the day. Currently image analysers still have a human interface for initiating the analysis rather than the processes being initiated automatically [47].

6.1.2 Project scope

The scope of this project was to develop quantitative analytical techniques for assessing product quality using SEM images. Specifically, the project was required to deliver:

1. Quantitative analysis of key particle characteristics, including:
    - Particle sphericity
    - Particle surface smoothness
    - Prevalence of particle cracking
2. These parameters were to be measured reliably across representative samples, with methods developed, implemented, and reported as part of the project outcomes.
3. Identification and implementation of additional analytical improvements, where appropriate (e.g., particle size distribution or other relevant laboratory techniques), with progress and outcomes discussed during monthly meetings with MRIWA.
4. Development and delivery of a training package to ensure that the analytical techniques created in the project can be adopted and applied by at least two staff members.

6.1.3 Objectives

The main objective of this project was to reduce the time and labour needed to analyse SEM images to determine the quality of pCAM particles as well as human bias present in the process. This was done through:

1. Investigating what programs are available for image analysis and selecting the one that was most suitable
2. Determining the parameters required by the software and produced data sets for training for qualitative analysis of the particles within the images
3. Adapted the software to identify individual particles in the images acquired
4. Adapted the software to quantitatively determine the percentage of cracked particles as well as the sphericity and smoothness of the surface of the particles

6.2 Methodology

Over the course of this project, image analysis programs were developed. This program was created to quantitatively determine the PSD and percentage of cracked particles within a SEM image as well as the sphericity and surface smoothness of the particles within the image. The SEM images and PSD data used to create and validate the programs were provided from results obtained by the C4P team during stage 2.

6.2.1 Software

The coding for the original training set file generation program and analysis program was created using Python 3.13.3. In addition to the base functions, several other libraries were used to complete the programs. The original training set file generation program the openpyxl and Pillow (PIL) packages to produce a Microsoft Excel workbook. The analysis program also used the PIL library along with the cv2, pandas, numpy and tqdm libraries as well as specific modules from the Scikit Image, matplotlib and scipy libraries.

6.2.2 Developing the analysis program

The first step in creating the program was developing the code to identify the particles in the image and create masks of them to allow for analysis. To achieve this, the contrast of the image needed to be manipulated and enhanced. This was done by using the technique of contrast stretching which redistributes the intensities of the pixels of the image over a larger range. This was followed up by the binarization of the image. This was achieved using the cv2 functions cv2.THRESH_BINARY and cv2.THRESH_OTSU. The two functions were used in conjunction instead of one or the other as cv2.THRESH_BINARY binarizes the image and cv2.THRESH_OTSU removes noise from the image. A preprocessing function was then constructed to remove imperfection in the base binary image, such as removing holes within the middle of particles, to allow for the accurate representation of the particle area by the mask. A function for extracting the masks for the particles from the pre-processed binary image was created using the scikit image measure functions to label and extract the dimensions of the masks including the area, perimeter, solidity and centroid of the masks as well as the length of the major and minor axes and compiled in pandas dataframe. The calculation circularity of the masks was also worked into the function and immediately added to the dataframe. A function for displaying the masks as a scatter plot overlayed on the binary and original images was

created to show how well the masks represented the particles within the image as shown in Figure 33.

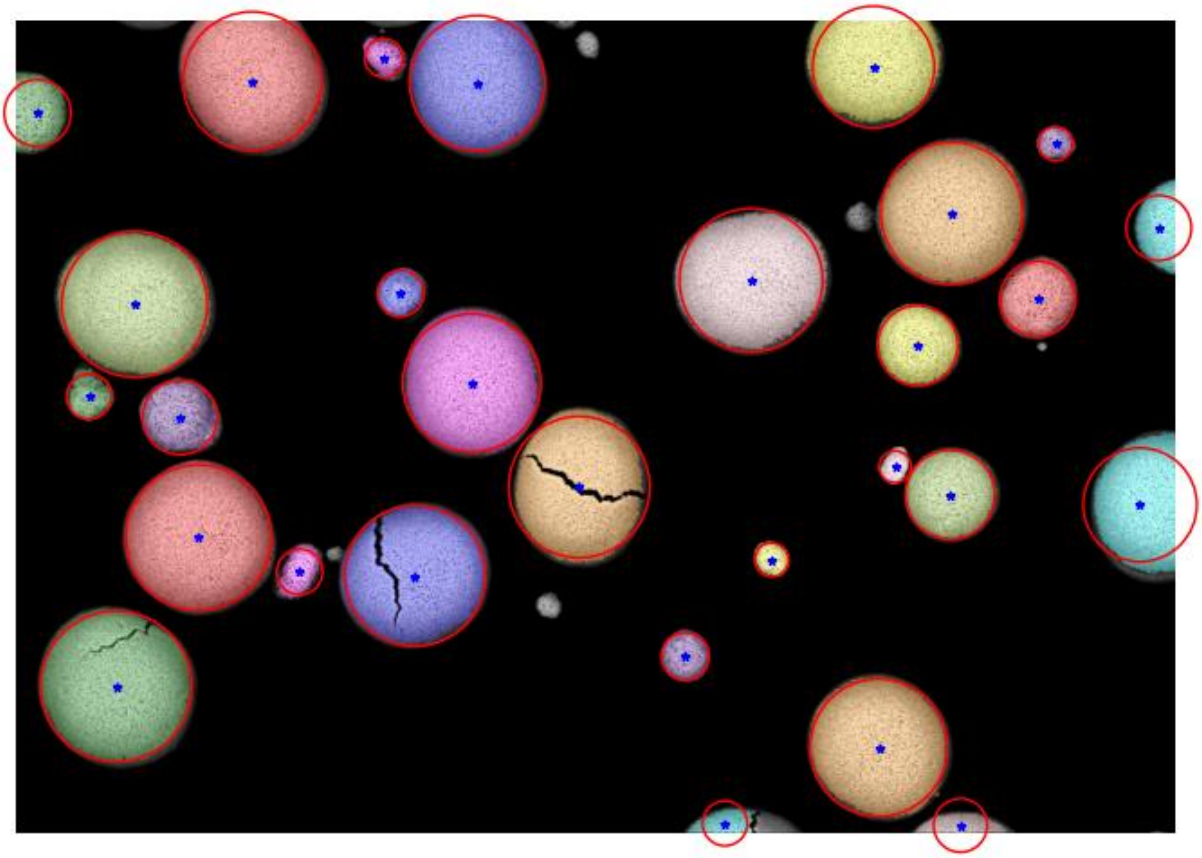

Figure 33 The initial masks for the 1000× magnified image, overlayed on the original image

The first function developed calculated the diameter of the mask using five different methods, allowing for tailored selection in the D50 calculation. Two functions were created for the direct calculation of the D50 of the sample within the image. The first calculated the D50 based on the median diameter of the particles and the second calculated the D50 based on the volume of the particles using the cumulative sum divided by the total sum of the volume of the particles. Ultimately, the calculation of the D50 of the particles by volume was used in the final program.

The identification of cracked particles followed the creation of the functions for the calculations of the PSD of the sample. A review of literature for a method for the detection of cracks in SEM images did not yield any fruit as the identification of cracks was the primary focus of the programs and models used and were almost exclusively on a homogeneous plane [41, 42, 48, 49]. This meant that the cracks were masked directly rather than needing to be detected in an existing mask. Therefore, a new method needed to be developed. The first step was adapting the masks to pick up the cracks as the masks were solid in all cases excepting large cracks. To achieve this, a toggle was added to the initial generation of the masks to prevent the filling of holes in the mask after the dilation step. A plot of the resulting masks was plotted and showed the cracks on the particles within the masks along with some small holes. An example of the filled and non-filled binary masks is shown in Figure 34. A function was then created around a ‘for’ loop which iterated through the rows in the dataframe taking a ratio between the masks with and without the hole filling step, compared it to a threshold and increased the count of cracked particles depending on the result.

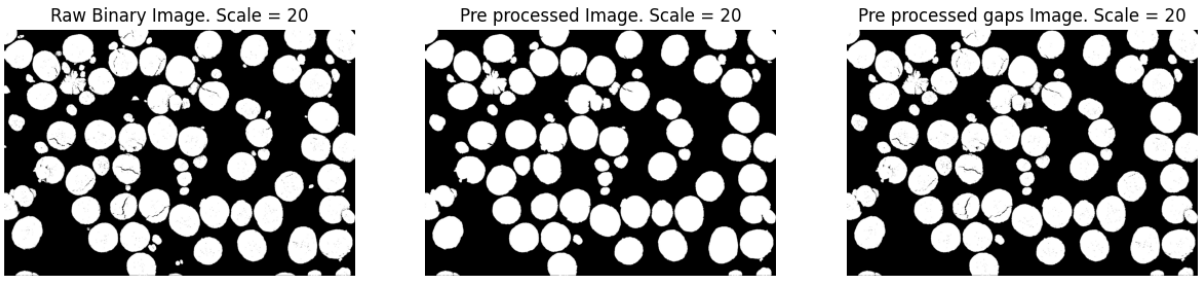

Figure 34 The raw binary image and pre-processed images created form the 1000× magnified image

During the development of the analysis functions to this point, it had been noted that program tended to group small particles together as well as some overlapping particles. To separate them, a function was developed to iterate through the masks and apply a secondary processing step to masks below a certain threshold for circularity in the form of a watershed separation.

The development of a method of presenting the results for the sphericity of the particles, which was determined to be synonymous with the circularity of the masks, was undertaken once the incorrectly grouped particles were able to be separated. The results were first collated and summarised numerically then a histogram generated to easily view the distribution of the values. An interpretation of the results was then added to allow for the quick characterisation of the sample using different shape classes.

The code for the identification of cracked particles was then transferred from the older version of the program where it was created. When copied in, the function produced an error whilst running saying that the index didn't exist in the dataframe. Upon viewing the plots of the masks, it became apparent that the removal of the hole filling step in the creation of the masks decreased the circularity of a large proportion of them below the threshold required for the application of the watershed to not be applied causing the particles to be split apart. This increased the number of masks significantly over the number created from the filled masks resulting in the error as the number of rows in the dataframe of the non-filled masks, which the loop used to determine the number of iterations, exceeded those in the filled masks. As this error could not be rectified, the older mask generation function was used as it generated the same number of masks regardless of the state of filling and produced an accurate representation of the number of cracked particles within the image.

The quantification of the smoothness of the surface of the particles was then undertaken. Initially, it was proposed that the gradient of the pixel intensities be used to determine the smoothness of the surface using local maxima to detect bumps on the surface. This method however had already been used in the separation of the particles showing that it would not work for the quantification of surface smoothness. This caused the silhouette of the particles to be used instead. The solidity of the masks, a ratio of the true area of the mask and the area of the convex hull of the mask which was already calculated and stored in the existing dataframe, was used to determine the surface smoothness and was summarised and presented using the same method as the sphericity of the particles with its thresholds and classes adapted to the new parameter of interest.

Once the functions for the calculations of the various parameters had been completed, the presentation of the results was addressed. Due to the modular construction of the code, the results of each analysis were printed directly after the code which produced them as the section was checked. The lines which generated the results were moved to produce the results at the end of the code with printed lines and plots used for debugging. A function was also created to produce a comma separated value (CSV) file for the numerical results and a text (txt) file for the result summary to produce lasting copies of the analysis. The lines regarding the importing of the various libraries

and modules used for the different functions were consolidated and moved to the beginning of the code preventing duplicates. Finally, the unused or duplicated code was removed, the program organised to conduct the analysis of the image in a logical manner and a progress tracker as well as an end statement added to complete the program.

Where thresholds were needed, an initial estimate was selected after viewing the relevant parameter within the main dataframe or calculation to be the working threshold and the function run to observe the results. The results were compared to the ground truth, which had been determined using traditional methods, and the thresholds to bring the results of the automated analysis closer to the ground truth. This process was repeated until an optimal value which produced the smallest error across all scenarios. The program was then tested as a Python 3 file and a Jupyter notebook file and the time required to run the program compared.

6.2.3 Program workflows

Original training set generation program

The development of the training sets for the program began with the construction of an efficient method for inserting the desired images directly into a document to allow for easy viewing. The code began with the generation of a blank excel document with a single worksheet labelled 'Test 25' after the folder from which the data would later be drawn. Headings were added to the column then the width of the columns changed. As the components generated thus far would be consistent across each worksheet, the worksheet was copied and renamed seven times corresponding to tests 26 to 32 using a 'for loop'. As the number of folders within each test was different, each worksheet had the height of the rows changed and images added individually on an as needed basis to prevent bloat within the file. This was achieved by procedurally generating the file paths required using a combination of nested 'for' and 'conditional' loops. A list of directories each folder contained was generated using a combination of the os.listdir() function and a conditional loop using the os.path.isdir() function. The active worksheet was then set to the folder being accessed (e.g. Test 25) then the rows labelled and the height of the rows changed for each directory within the folder using a for loop. As the number of images of each magnification within each folder was inconsistent, a conditional loop was employed using the os.path.exists() to prevent the code from producing an error or an image being inserted into the wrong column. The image was resized for ease of viewing then inserted into the column designated for that magnification. The document was saved after each change excepting the last steps as it was easier to complete the row modifications and image insertions at the same time to prevent the unnecessary duplication of code. After the document was generated, the file was opened and conditional formatting applied to the document to create a visual cue for the operator to determine the destination of the product based on its quality. A screenshot of the document is included in Figure 35.

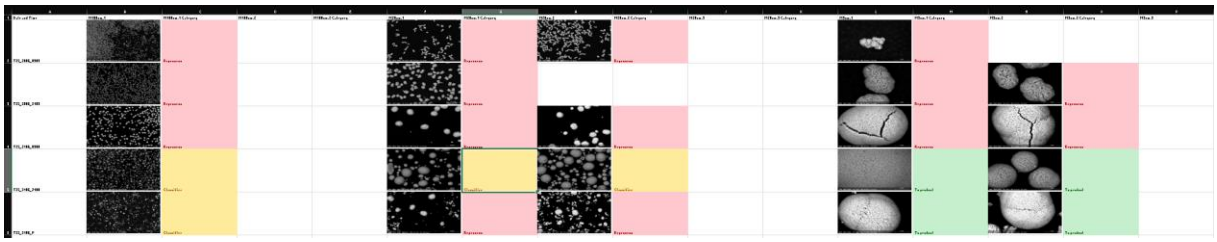

Figure 35 Screenshot of the reference workbook created by the code originally developed to create the training sets for an AI model

Analysis program

To ensure it is easy to find for when it needs to be changed, the main file path for accessing the folder which contains the tests to be analysed is defined at the beginning of the program. Following this, the libraries, modules and operating system required for running the program are imported. The functions for loading, processing, analysing and showing the images as well as the presentation and saving of results are defined before the code which creates the analysis and results runs. The working part of the program begins with the generation of the lists of subfolders and files within the subfolders for the creation of the image file path later. This section contains the options enable and disable parts of the code to allow single folders or files to be processed. Detailed instructions for doing this were included within the README.txt file included within the same folder as the program files. The 'for' loop for iterating through the files, which can also be modified in a similar way to the file path generator, then begins. The file path to the specific image is created, the scale extracted then the image loaded and converted to binary with a numpy array. The image is processed twice to produce the filled and non-filled masks. The number of the file being analysed out of the number of files in the subfolder is reported confirming that the masks have been created and enabling the monitoring of the analysis progress. The pre-processed image with the filled masks undergoes preliminary analysis using both the computing_metrics_refined and computing_metrics functions while the pre-processed image with the non-filled masks only undergoes preliminary analysis using the computing_metrics function. The filled masks with the computing_metrics_refined function applied are then plotted and shown. The next section of the code produces histograms depicting the spread of the circularity and solidity of the masks and is commented out by default. The analysis of the sample then takes place starting with the determination of particle sizes followed by the PSD, percentage of cracked particles, particle sphericity and surface smoothness respectively. The tabulated summaries in the form of dataframes produced by the particle sphericity and surface smoothness calculations are then concatenated in preparation for conversion into a csv file. The results are then compiled, formatted, presented and saved before the next iteration of the for loop begins. After all the files in all the subfolders have been analysed, the code prints the word "Finished" to signal the program has stopped after progressing normally.

6.2.4 Analysis program functions

Loading img:

This function loads the image and begins the preprocessing of it required to perform the required analysis taking the image file path as the only input. Once it has been loaded, the size of the image is taken and the border containing the metadata for the image removed. The image is converted to greyscale then converted to a numpy array of pixel intensities and enhanced using contrast stretching which changes the values of the pixel intensities over a range which increases the contrast between the particles and the background. The image is then converted to binary using the cv2.THRESH_BINARY function and cv2.THRESH_OTSU function to remove the noise. The function returns the binary image and the numpy array of the original image.

Reading scale:

This function takes the file name, which is extracted as part of the generation of the image file path, splits it between the underscore separating the test number and the scale of the image and the units ("um") to extract the integer which will be used to convert the pixels to μm.

Image processing:

The inputs for this function include the binary image, the scale of the image which is extracted using the reading_scale function and “on” or “off” which determines if the masks are filled or not. The area_opening function is applied to the image to produce a greater degree of separation between the particles to prevent a single mask being applied to multiple particles as often. This is followed by the removal of small objects function which, as the name suggests, removes small foreign objects or fragments which would skew the results of the analysis. The conditional statements which form the toggle for the filling of holes in the masks is then enacted. When the toggle is on, the function ndimage.binary_fill_holes is applied to the image and fills the perceived defects creating a solid mask which then is ensured to be in 8-bit values (greyscale) using the np.astype function. When the toggle is off, only the np.astype function is applied. The function then returns the pre-processed image containing basic masks of the particles.

Computing metrics:

The computing_metrics function labels and performs basic measurements on the masks of the pre-processed image. These measurements include determining the area, solidity, centroid and perimeter of the masks as well as the major and minor axis length and are compiled into a dataframe. The circularity is then calculated with the equation below and added to the initial dataframe.

$$circularity = \frac{4 \times \pi \times area}{perimeter^2} \tag{8}$$

Convert D:

The convert_D function calculates the diameter of the mask using a variety of methods. The first takes the average of the major and minor axes, the second uses the first equation below, the third defines it as the length of the major axis, the fourth as the length of the minor axis and the final method calculates the diameter from the area of the mask using the second equation below which yields the same value as the second method. The function then returns all the calculated diameters in order.

$$diameter = 2 \times \sqrt{\frac{area}{\pi}} \tag{9}$$

Show results blods:

This function creates two subplots which show the masks of the particles. Both plots are formed by scatter plots with the first overlayed over the binary image to brighten the masks for easy viewing and the second overlays them on the original image to show how they compare to the actual particles. The function also calculates the effective radius of the mask using the diameter of the mask calculated with the first method of the convert_D function and plots the centroid of the mask with a circle whose radius is equal to the effective radius of the mask. The first plot is labelled “Preprocessed:” followed by the total number of masks within the image and the second is labelled “Original image with blobs”.

Pix2um:

The pix2um function converts the distance and area measurements of the masks to µm taking the output of the reading_scale function and the dataframe containing the mask labels and measurements as inputs. The function uses the scale passed to it to determine the conversion factor then applies it to all the distance and area measurements. The function can only handle 100 µm and 20 µm scales.

Calculating d50 volume:

The calculate_d50_volume function determines the PSD of the sample using the D50 by volume. The calculation takes the diameter of the masks using the second calculation method of the convert_D function, uses it to calculate the volume using the equation below, assuming a spherical shape, and orders the masks in ascending order using the np.argsort function. Once sorted, the ratio of the cumulative sum and total sum of the particle volume is taken and the function np.interp used to return the volume at which the ratio is equal to or exceeds 0.5.

Computing metrics refined:

The computing_metrics_refined function is made up of three passes. The first pass contains the same code used in the computing_metrics function to create the initial masks. The second pass compares the circularity of each mask to a threshold to determine if further processing is required. If the circularity of the mask falls below the threshold, the mask is extracted and a local watershed applied. The local maxima of the mask are then determined and their coordinates recorded before they are separated by another watershed application. The new masks are labelled with reference to the original image and added to the dataframe with the labels of the existing masks also being updated. The final pass recalculates the measurements in the dataframe, checks that all the circularities fall between zero and one and the perimeter values are valid before returning it and the labelled image. Due to the large number of iterations that this function potentially runs, a progress tracker is also included to allow monitoring.

Sphericity and surface smoothness functions:

The functions for determining, summarising and presenting the shape and surface profile of the particles are identical regarding processing and only differ in the parameters which are measured, the thresholds for differentiating classes and the words used to described them. The functions for the two characteristics are differentiated by the first letter of the parameter as it appears in the code. This is shown as (s/c) in the function name where ‘s’ refers to the solidity of the mask used to determine surface profile and ‘c’ refers to the circularity of the mask which is used to determine particle shape with only one being used at a time (eg. _class_from_s). The thresholds for the functions are consistent with the parameter being measured with the thresholds for the solidity functions being 0.70 and 0.96 and the thresholds for the circularity functions being 0.70 and 0.90.

Class from (s/c):

These functions define the three classes of each parameter which the masks are sorted into. The functions take the solidity or circularity of the mask as well as an upper and lower threshold. If the solidity or circularity of the mask is equal to or greater than the upper threshold, the class ‘smooth’ for solidity and ‘near-circular’ for circularity is applied. If the solidity or circularity of the mask is equal to or greater than the lower threshold but less than the upper threshold, the class ‘rough’ for solidity and ‘sub-rounded / mildly elongated’ for circularity is applied. If the solidity or circularity of the mask is lower than the lower threshold, the class ‘jagged’ for solidity and ‘elongated/angular’ for circularity is applied.

Summarize overall (s/c) from df:

These functions create a numerical analysis and tabulated summary. The functions take the main dataframe and two thresholds as arguments. The function extracts the number of masks and calculates the median circularity or solidity, interquartile range (IQR) and the percentage by count and by area of masks which have a circularity or solidity equal to or greater than the upper threshold.

Both the overall summary and a tabulated summary containing the count for all of the classes of particles are returned by the functions.

Interpret overall:

These functions create a text version of the overall results which includes a worded description of the results. The functions take the overall summary from the respective function summarize_overall_(s/c)_from_df and two thresholds and contains a toggle for the return of the textual description. The textual description contains the almost same information as the overall summary input with the addition of description of the results and the combination of the percentages of masks with a circularity or solidity higher than the upper threshold combined into one line. The median description states the class the typical grain within the sample is a part of, the IQR description states the classes which the range spans (eg. spans rough to smooth) and the description of the masks with a circularity or solidity higher than the upper threshold commenting on the particle size when compared to the number of particles present (eg. Near-circular grains are small on average (contribute far less area than their count share)). When the toggle for the return_text argument is set to true, the functions return the overall summary with the worded descriptions as a string.

Cracked particle calculation:

The cracked_particle_calc function calculates the number and percentage of cracked particles within the sample. The function takes two dataframes created by the computing_metrics function for the filled and unfilled masks. The total and cracked particle counts are set to zero upon activation of the function to prevent miscounting and an empty list created. The rows in the dataframe are iterated through based on the number of rows in the non-filled mask dataframe and the ratio of the area between the non-filled and filled masks taken. These ratios are added to the empty list to allow for debugging. The ratios are compared to the predetermined threshold and those less than or equal to 0.987 cause the count for the number of cracked particles to be increased by one. The total number of particles is increased regardless. The percentage of cracked particles is calculated using the total and cracked particle counts. The count and percentage of cracked particles within the image are returned as well as the total count.

Create results files:

This function creates a csv and txt file of the combined tabulated summaries of the circularity and solidity of the masks and the full interpreted results of analysis respectively as well as a string of the full interpreted results of analysis. The function first creates the names for the files and checks if they already exist. If they do, a ".1" is added to the end of the file name and checked again with the number increasing each time the name is found to exist. The file name is then finalised. The results for the cracked particle and PSD analyses are formatted then compiled with the interpreted summaries of the circularity and solidity of the particles within the image into a single string. The tabulated summary, which is concatenated within the main code, is then converted to a csv file and the compiled analysis results string is written to a txt file. The two file names and the string are returned by the function.

6.2.5 General Limitations

As this program was developed for a specific project, there are limitations associated with it. The program can only process images of 250× and 1000× magnification. Images of 8000× were provided for analysis however the decision was made to not use them due to the limitations of the

initial mask generation process as it requires the whole particle to be visible to produce accurate results and a single particle often fills the entire image at 8000× magnification. The program also tends to unnecessarily subdivide masks as the process of determining which particles need to be subdivided is based on the circularity of the mask. As the circularity of the non-filled masks used in the determination of cracked particles have a circularity much lower than that of the filled masks, they are severely affected by this issue as shown in Figure 36.

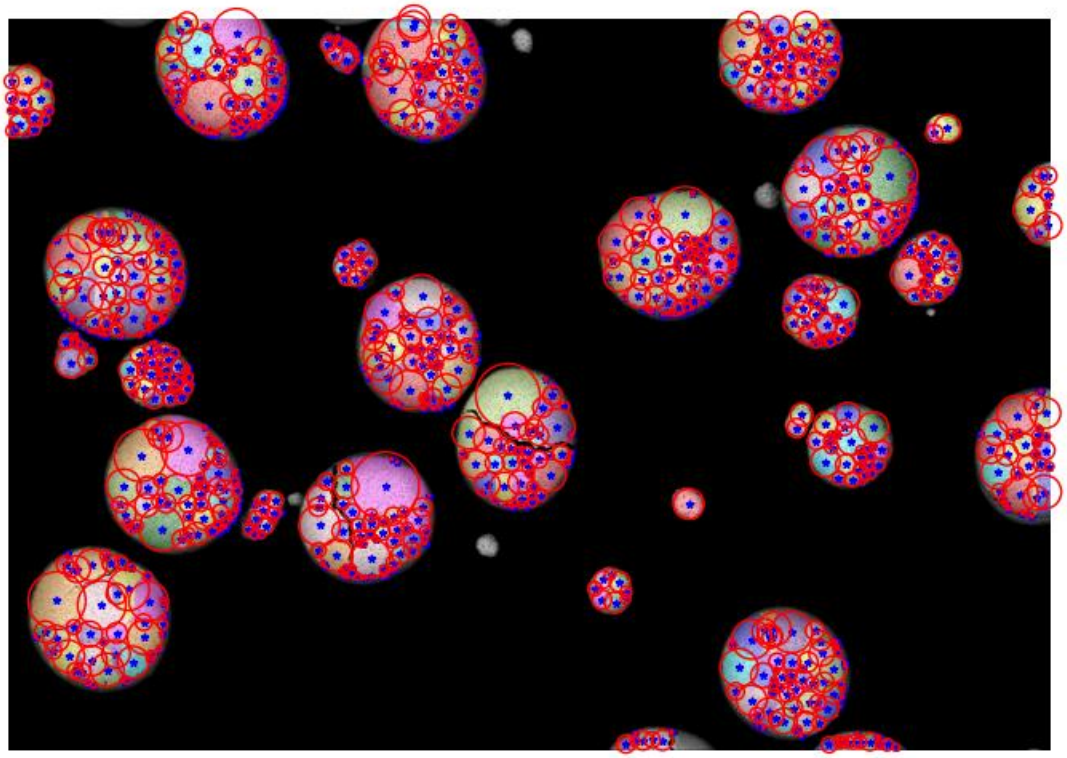

Figure 36 Masks generated by the computing_metrics_refined function using non-filled initial masks generated for the second 1000× magnified image

Due to the phenomenon, the number of masks generated by the computing_metrics_refined function between the filled and non-filled initial masks is significantly different. As the masks produced by the computing_metrics_refined function cannot be compared, the computing_metrics function which does not included the additional processing step is used. This results in different masks used for the calculation of the percentage of cracked particles within the sample than are used for the other calculations performed on the sample however the results produced by the program are typically close to the ground truth. Instances where they are not close is when the sample is comprised of small particles. When this is the case, the number of cracked particles 'detected' by the program is much higher than the ground truth as they tend to be irregular in shape causing deep shadows which cause the ratio between the area of the two masks to fall below the specified threshold and be counted as cracked particles. The opposite issue is observed in particles which have large cracks in them. These cracks are large enough to avoid being filled in by the ndimage.binary_fill_holes function. This means that both masks have that area missing causing the ratio between the area of the two masks to be above the threshold and not be counted. This typically does not cause the program results to drift from the ground truth as the program tends to be slightly more sensitive than required resulting in approximately the same number of false positives as false negatives resulting in no change to the real result.

Tests of the program using different file formats were also conducted to ascertain whether the program could be run without the use of the internet. The program was developed using Google

Colab to allow the file to be easily shared and worked on by multiple people. When the program is run in Google Colab, it takes 33 minutes to run with the 250× magnification images taking the longest to process due to the large number of particles they contain. The file was converted to a python 3 (.py) file then run on a personal computer with an Intel® Core™ i5-9400F central processing unit. The program ran for 20 hours 1 minute and 59 seconds before terminating due to an invalid file name with 20 hours 1 minute and 11 seconds spent processing the 250× magnification image of sample T25_2606_2108, which contains 1578 initial masks, with the time per iteration increasing over time as shown in Figure 37. The sharp spike in processing time for iteration 1452 was caused by the computer which was running the program entering sleep mode then taking time to restart background processes and some applications. The computer entered sleep mode for 3 hours 26 minutes and 29 seconds during iteration 1442 causing that iteration to take 1 hour 30 minutes and 3 seconds and the next iteration to take 1 hour 3 minutes and 30 seconds as they gradually returned to the values within four seconds of the values before the spike. The time taken to run iterations 1442 to 1451 were omitted as the prevented the trend in the data to be seen due to scaling of the vertical axis. The program was converted to a Jupyter Notebook file (.ipynb) file and run in the Jupyter Notebook environment taking 29 minutes and 13 seconds. While Jupyter Notebook requires a web browser to run, the program was confirmed to run without an internet connection due to the connection dropping out during the test.

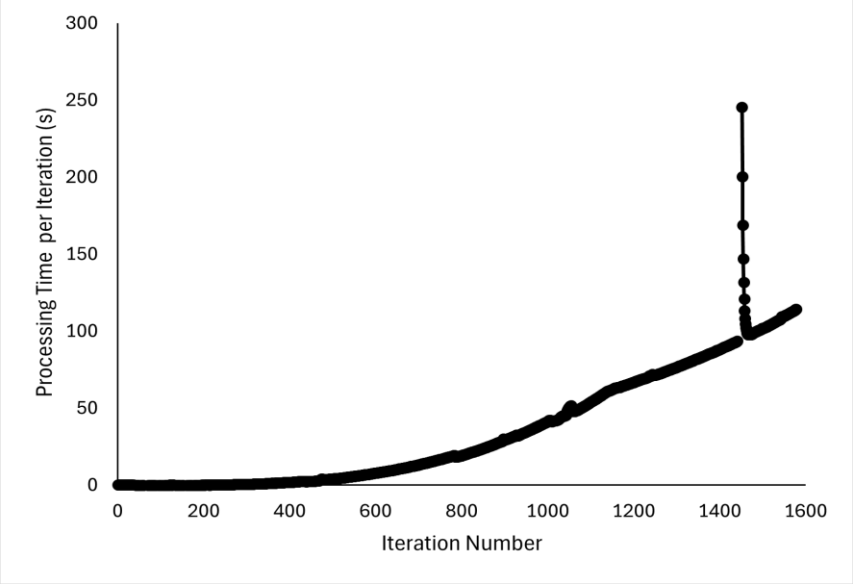

Figure 37 Results of the test run of the .py version of the analysis program showing the Processing time per iteration for the 250× magnification image

6.2.6 Mask Fitting

After the initial generation of the particle masks, the program showed good segregation performing best on samples containing small to medium near-circular particles with a narrow range of sizes at 250× magnification. When wide range of particles is present the program struggles to accurately separate the small particles and subdivides the large particles especially in the 250× image. In the 1000× magnified image of the previous sample, a large proportion of the small particles within the image were not masked as they were removed during threation of the pre-processed image by the remove_small_objects function due to their small size and the difference in size between them and the larger particles within the image. These issues are observed in other tests with the first being primarily observed in images of 250× magnification and the second in images of 1000× however

the issues typically aren't as pronounced as they appear in sample T26_2606_2110. As mentioned previously, the masks of large particles undergo unnecessary subdivision. This is a systematic issue caused by the method by the determination of which masks require subdivision. As the masks are selected for subdivision based on their circularity, large particles which are formed from the combining of two smaller particles, creating an elongated particle with a depression in the centre around the join, as well as particles with large cracks which avoid filling during the initial creation of the filled masks are also typically caught up and subdivided. This typically results in a lower PSD and average circularity as well as a higher proportion of smooth particles when an effect is observed. The issue of subdivision is even more prevalent with the unfilled masks as shown in Figure 36 which rendered the data as unusable when processed using the computing_metrics_refined function. The program also encounters problems with very large, spherical or near spherical particles due to the shadows cast on their underside. The intensity of the pixels within the shadows falls within the same range as the pixels which make up the background causing the shadowed portion of the particles to be classified as part of the background during binarization. This creates a partial mask which does not accurately represent the particles and undergoes unnecessary subdivision in the form of very small masks around the edge of the main mask.

6.2.7 PSD

Most of the values for the PSD of the samples containing small to medium near-circular particles with a narrow range of sizes fell within 15% of the ground truth. A large difference between the PSDs determined by the program from the two magnifications of the same image was noted. The large difference was caused by the inaccurate division of particles which decreased the size of the larger particles and increased the number of smaller particles, both of which contributing to the smaller value. Very large errors were observed in the samples which had a large discrepancy between the particle sizes as the small particles within the image were incorrectly grouped together creating masks many times larger than the largest particles within the image which disproportionally effect the PSD of the sample as calculated by the program.

6.2.8 Sphericity, Surface Profile and Presence of Cracked Particles

The sphericity of the particles was determined using the same methods as if it were determined manually. Therefore, the error between the ground truth and the program results would be due to the error in the masking rather than an error in the calculation. Due to the excessive subdivision of masks, the median circularity of the sample tends to be lower than the actual value and near circular particles tend to be small on average contributing far less area than their count share.

To determine the accuracy of the program results, the percentage of smooth particles was compared to the qualitative analysis of the sample and judge whether it was appropriate. Some error was introduced due to the excessive subdivision of particles leading to a larger number of particles being classified as smooth due to the straight edges of the smaller masks.

The ground truth for the number of cracked particles within an image could be obtained by manually counting them. Some errors were observed in images containing small, irregular particles as the shadows between them were interpreted as cracks by the program. The inverse was true for large particles containing large cracks as they were picked up by the filled mask so could not be detected by a difference in area between the filled and non-filled masks. This second issue tended to be balanced out by the slight over sensitivity which was observed in the program.

6.3 Conclusions and Future Work

A program has been developed to analyse the PSD, sphericity, surface smoothness and the percentage of cracked particles within SEM images of a sample with 250 and 1000 magnification and is one of the first instances of automated SEM image analysis for the battery industry. It should be run using Jupyter Notebook to reduce the processing time for images containing over a thousand particles. The analysis it supplies for small to medium, near circular particles is satisfactory with PSD values falling within 15% of the ground truth and a good agreeance between the quantitative and qualitative results for the other values. The programs main issues revolve around the generation and segmentation of the particle masks with it ignoring many small particles in some images, collecting multiples small particles together in a single mask and excessively splitting large particles. The software developed in this project enables the simultaneous processing of multiple SEM images. It automatically generates quantitative reports detailing particle sphericity, surface smoothness, prevalence of cracking, and PSD. This represents a substantial improvement over previous qualitative assessment methods, providing consistent, objective, and highly reproducible metrics. The ability to quantify these key indicators significantly enhances the accuracy and efficiency of product classification, thereby supporting earlier detection and prevention of issues such as elevated charge density associated with particle defects.

Future developments should focus on enhancing both the accuracy and robustness of the image-analysis program. A key priority is improving mask generation, as current limitations result in the unnecessary splitting of large particles and the merging of small particles into a single mask. Implementing a convolutional neural network (CNN) specifically trained for particle masking would significantly reduce these issues and is expected to improve the accuracy of the PSD and sphericity outputs greatly.

Additional CNN models could also strengthen other components of the analysis workflow. A dedicated CNN for detecting cracked particles would allow reliable identification across a wider range of crack sizes while reducing false positives. Similarly, incorporating a CNN designed to assess particle surface smoothness would enable more precise detection of surface defects, moving beyond the current silhouette-based approach.

Finally, the program should be expanded to accommodate images taken at any magnification. Adapting the system to recognise and normalise scale automatically would increase its versatility and ensure broader applicability across different imaging conditions and sample types.

Collectively, these improvements would enhance the precision, usability, and overall capability of the tool, supporting more rigorous and automated particle-characterisation workflows in future studies.

7 Next Generation Battery Materials

7.1 Introduction

The global battery sector is rapidly evolving. This shift is driven by demand for energy storage solutions with higher efficiency, longer life and lower cost. Next-generation battery materials are emerging that include advanced chemistries and particle engineering strategies such as elemental gradients, novel dopants and high-capacity systems.

Countries and companies are competing to lead in battery innovation, without local R&D, Australia risks falling behind and relying on overseas breakthroughs that are likely to remain proprietary. This activity aims to start to strengthen Western Australia's capability and knowledge in next-generation battery materials. Such materials are expected to shape future commercial standards or pave the way toward them. Strategies to address various degradation mechanisms in NCM cathodes include doping and controlling particle microstructure during cathode particle synthesis. Two tests were conducted as a part of this stretch goal, one using Ti as a dopant in NCM 83 12 05 pCAM chemistry as literature has shown that Ti can stabilise the structure, reducing cation mixing and undesired phase transitions, leading to reduced chemo-mechanical degradation with cell cycling [50]. The other test demonstrated the ability to form elemental gradients within particles, with a NCMA core and NCM shell. This aimed to achieve the high energy density from a nickel rich core, while having a more structurally stable outer layer.

This research builds on previous work with NCM cathode materials and uses semi-batch coprecipitation procedures developed. Candidate materials were selected based on global research trends and evaluated for performance. It should be noted that these tests were only conducted as initial scoping tests to inform future work programs and optimisation is yet to be conducted.

7.2 Literature Review

7.2.1 Next-generations strategies

Several mitigation strategies have been proposed to counter the different degradation mechanisms that occur within NCM cathodes. The most prominent are cathode particle surface coating, doping and the control of the particle microstructure during the synthesis of cathode particles (Figure 38). Doping has been shown to improve structural stability and mitigate phase transitions, whereas coating prevents surface degradation and hinders reactions with the electrolyte. In addition to improving the cycle life of cathode materials, the extent of the improvement may also provide insight into the dominant degradation mechanisms [13]. Surface coating most commonly occurs during the pCAM to CAM conversion process which is out of the C4P scope of work.

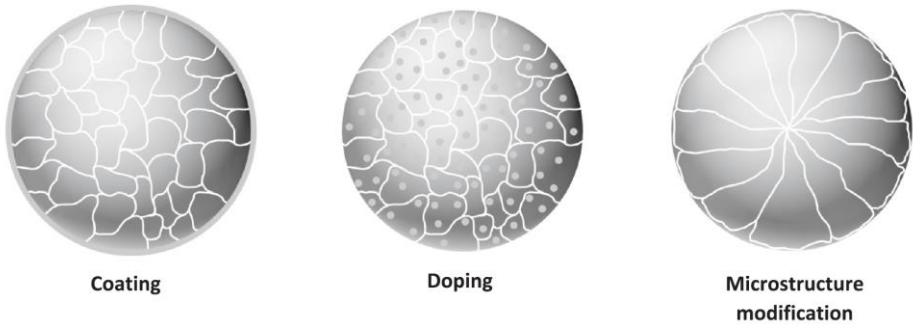

Figure 38 Illustration of the main cathode degradation mitigation strategies; coating, doping and microstructure modification [13]

7.2.2 Ti dopant effects

Different ions with various valences can be introduced into the crystal lattice, where they can occupy different sites. Some elements have been shown to enhance the structural stability, leading to improved electrochemical properties [50]. In this work, the effects of Ti^{4+} as an advanced dopant was investigated.

Transition metals such as Ti, Nb, V, Ta and Mo have a high oxygen affinity, effectively dragging oxygen toward them, as the bond length between these atoms and oxygen is shorter when compared to that of Ni or Mn with oxygen [25]. Ti, when used as a dopant reduces the degree of cation mixing as Ti suppresses the oxygen vacancy formation. Considering the higher migration energy for Ti than that of Ni, Ti ions are less prone to dissolution into the electrolyte, instead, they migrate onto the formed Li and TM vacancies, which eventually generates a Ti-rich rock salt layer on the cathode surface. As a result, this Ti-rich layer pins the oxygen ions and inhibits their migration from the bulk to the surface, preventing continued surface corrosion during long-term cycling. It has been demonstrated that Ti doping could efficiently mitigate phase transition during cycling, implying that the stronger Ti-O bonding could mitigate the oxygen site rearrangement. As a result, Ni-rich Ti-doped pCAM maintains secondary particle integrity even after long-term cycling [23, 50].

7.2.3 Gradient strategy

Another approach to control the structure of secondary particles is to create a core-shell particle, which functions similarly to a coating but involves a thicker layer that is usually chemically similar to the inner core and can be electrochemically active. An example of a core-shell particle is a particle that has a Ni-poor and Mn-rich outer layer (a shell) and a Ni-rich bulk (the core). The Ni-rich inner core provides a high specific capacity and is protected from the effects of electrolytic degradation, and its volume change can be restricted due to a more rigid, stable outer layer. However, the core-shell interface may still degrade over time due to uneven expansion of the different materials. A smoother transition from a Ni-rich to Ni-poor region (i.e. a gradient) could alleviate these structural instabilities as either a core-shell with a concentration gradient or with a full concentration gradient, as shown in Figure 39 [13]. This can also be obtained by doping the particle to various degrees as a function of the distance from the particle centre [9, 13]. When comparing to the inner composition and outer composition material cycling stability, a full concentration gradient (FCG) structure displayed capacity nearly as high as for the Ni-rich inner part, but with stability resembling that of the outer Mn-rich part [13].

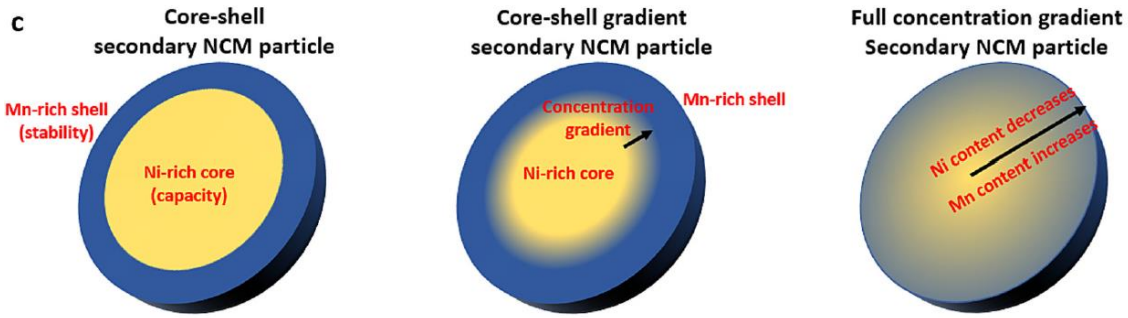

Figure 39 Illustration of core-shell, core-shell concentration gradient, and full concentration gradient NCM particle structures [13]

Considering the current careful fabrication process, a gradient structure cathode material would be difficult to produce in large quantities for use in EVs or other mobile energy storage applications. However, as gradient structures exhibit such promising characteristics, the research in this field continues with the hope of overcoming these difficulties [13].

7.3 Experimental Procedure

7.3.1 Materials

The Ni, Mn and Co sulfates used were as per described in section 1.3.2. The same Al used was used as stated in section 4.3.1. The Ti used was AR grade titanium oxysulfate ($TiOSO_4$) containing 17% Ti.

7.3.2 Semi-batch Reactor Configuration

The hte units were operated in semi-batch mode (using a settling arm) as per section 3.3.6.

7.3.3 Preparation of $Ni_{0.83}Co_{0.12}Mn_{0.05}Ti_x(OH)_2$ precursors in a Semi-Batch Test (Doping Test B31)

The transition metal solution was prepared as per section 1.3.2, with the addition of Ti as a dopant. The process conditions were similar to those used for previous semi batch test work, but with a lower pH and extended chemical addition time. The lower pH was selected to prevent Ti gel formation, which is demonstrated to be exacerbated at higher pH. An extended chemical addition period was conducted to collect additional data about particle growth over time.

7.3.4 Preparation of Ni-rich with Al precursors as the core and a Mn-rich Ni-based chemistry as the shell in a Semi-Batch Test (Gradient Test B32)

Two transition Metal solutions were prepared, one Ni-rich with aluminium doping (NCMA) for the core and another comparatively Mn-rich Ni-based for the shell of the particles. Mn-rich chemistry as the shell was selected for this test, as the C4P team had previously successfully produced, during previous stages conducted under the FBI-CRC, on-specification pCAM products that outperformed commercial benchmarks in electrochemical performance using this chemistry. A summary of the chemical addition time and pH for Test B32 is shown in Table 6.

Table 6 Summary of the chemical additions in Test B32

Time	0-5 h	5-6 h	6-7 h	7-8 h	8-10 h
Ni rich with Al	100%	75%	50%	25%	0%
Mn-rich Ni-based	0%	25%	50%	75%	100%
Premix ratio one	100%	100%	100%	0%	0%
Premix ratio two	0%	0%	0%	100%	100%

7.3.5 Characterisation

Samples were characterised by PSD, SEM, tap-density, ICP-OES, XRD and EDS using the same instruments and methodologies as specified in section 1.3.3.

7.4 Results and Discussion

7.4.1 Ti Doping Test

The tap density of particles produced with Ti doping were within the target specification, and did not show significant alteration from tests conducted in the absence of Ti. Although the Ti doped Test was conducted with a slightly lower addition rate the D50 of particles decreased slightly, the opposite of what was expected. Therefore, it is likely that doping with Ti reduces the particle size. This result aligns well with previous studies, which have demonstrated that a reduction in primary particle size resulted from nucleation. The fine primary particles with numerous grain boundaries dissipate the strain and divert the crack path. This is important to limit fracturing and improve cycle life of the battery [25].

SEM images of the final products from Tests B31 and B30 are presented in Figure 40. The particle morphology appears largely consistent between the two tests; however, the particles in Test B31 are slightly more spherical. This phenomenon can be due to the influence of the Ti dopant, which reduces the size of the primary particles, and resulting in the formation of more spherical particles during agglomeration. While no cracking was observed in the majority of particles, some particles exhibited microcracks. Figure 41 displays SEM images at 4, 7 and 8 hours. Microcrack formation is first observed at 4 hours and appears to deepen progressively with time. Figure 42 shows the SEM images of the final product, captured at various magnifications, focusing on a representative cracked particle. These observations suggest that the Ti concentration used is likely excessive for an NCM composition containing 83 mol.% Ni. To mitigate microcrack formation, test work in future work programs will investigate reducing the Ti concentration. While microcracks may be present throughout the sample, it is critical for future work to determine whether they propagate during electrochemical cycling and to assess their impact on battery performance.

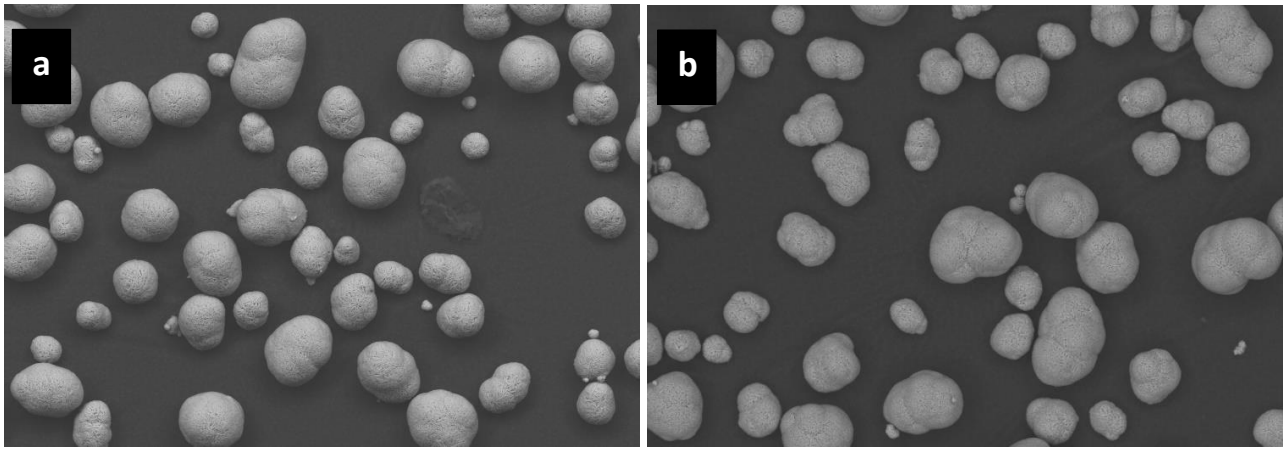

Figure 40 SEM images of the final products at 24 h. a. with Ti dopant. b. without dopant

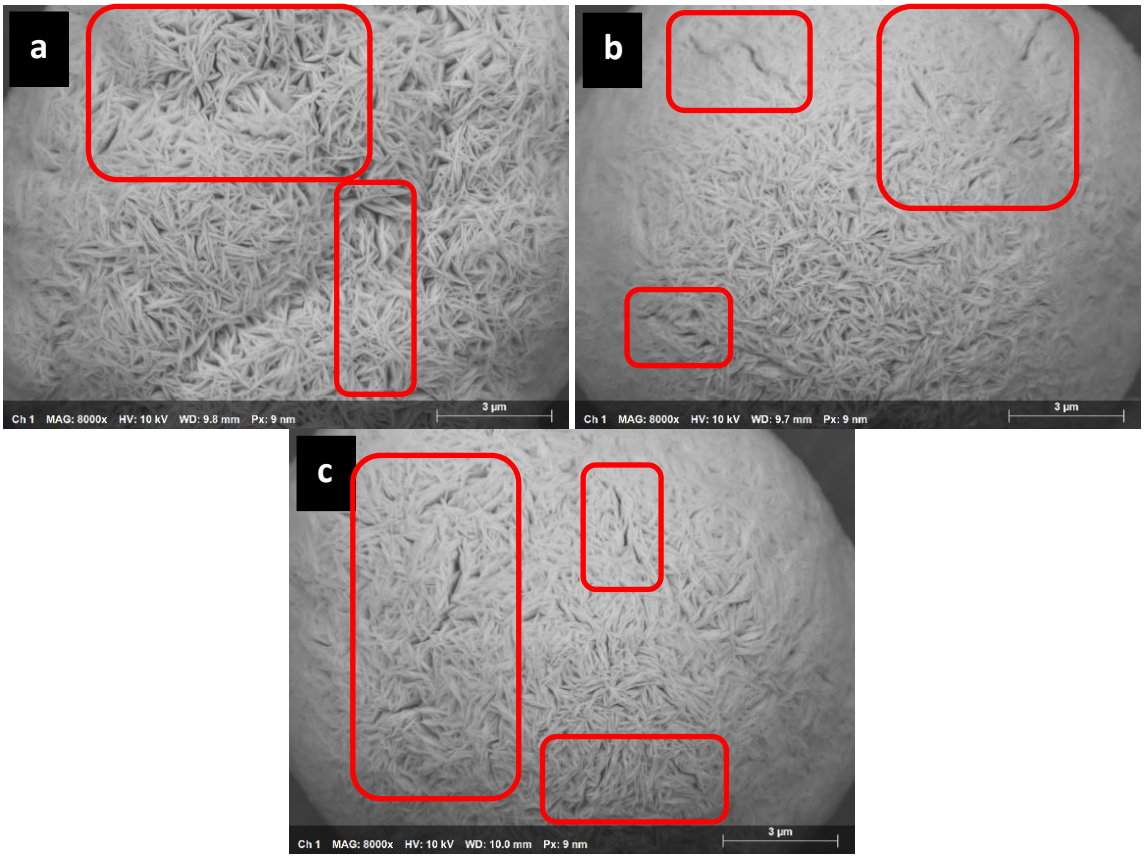

Figure 41 SEM images of Test B31. a. After 4 h. b. After 7 h. c. After 8h

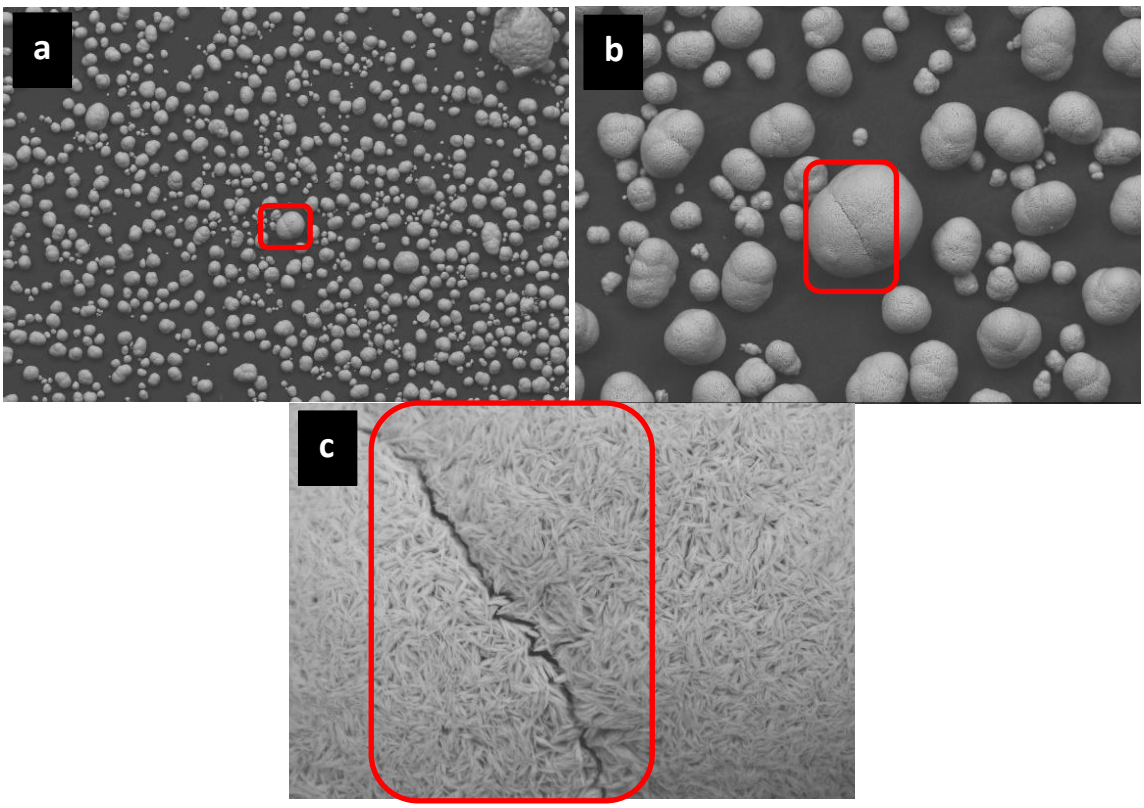

Figure 42 SEM images of final product produced with Ti doping at different magnifications

X-ray diffraction patterns of the solid pCAM products with and without Ti are compared within the range of 5-45° and 65-90° (Figure 43). Test 9 serves as an on-specification reference, without a dopant. With Ti, a single additional small peak was observed around 31°, but due to its low intensity and lack of additional supporting peaks, phase identification was not possible. Additionally, a slight shift in peak positions was noted, suggesting that Ti was incorporated into the crystal lattice, leading to minor changes in lattice parameters.

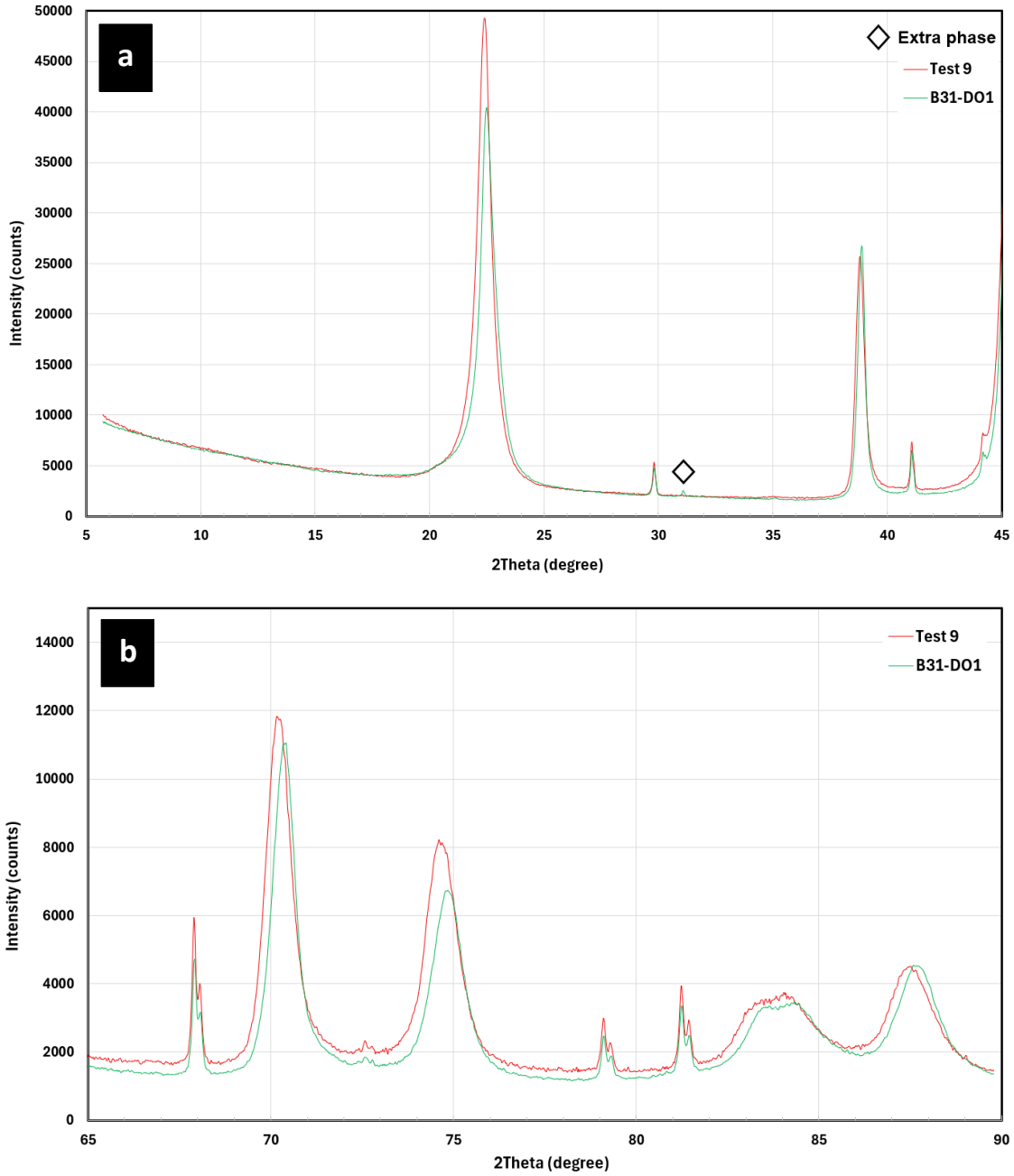

Figure 43 X-ray diffraction patterns of the solid pCAM products Test B31 and Tests 9. a. In the 2Theta=5-45 degree. b. In the 65-90 degrees range

7.4.2 Gradient Test

During the gradient test there was a minor control system communication error which resulted in some particle fragmentation. Despite this, it was demonstrated that particles with the desired elemental gradient could be produced with the desired tap density and particle size close to target specification.

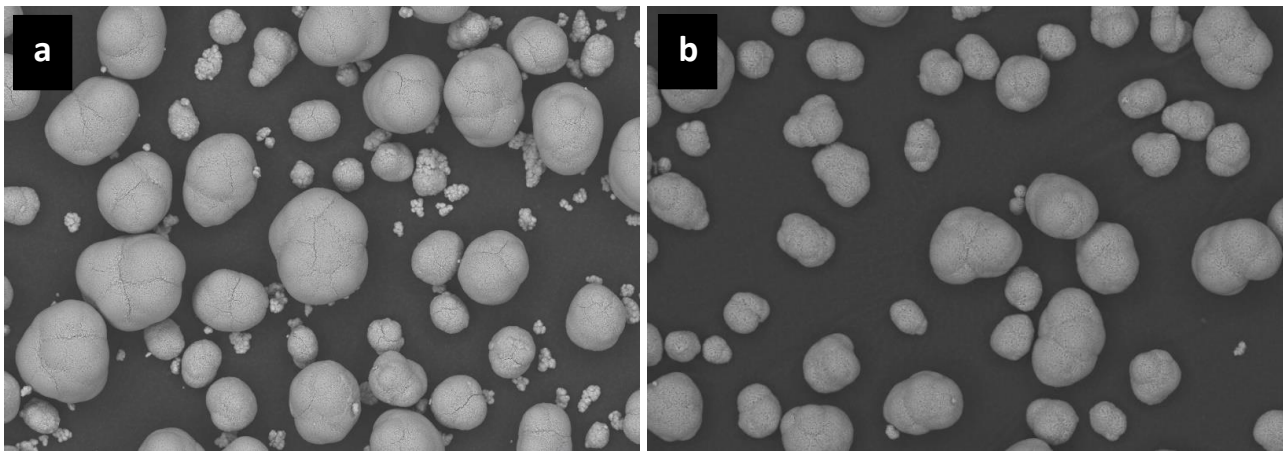

Figure 44 SEM images of the final products of the gradient test (a) and standard pCAM (b)

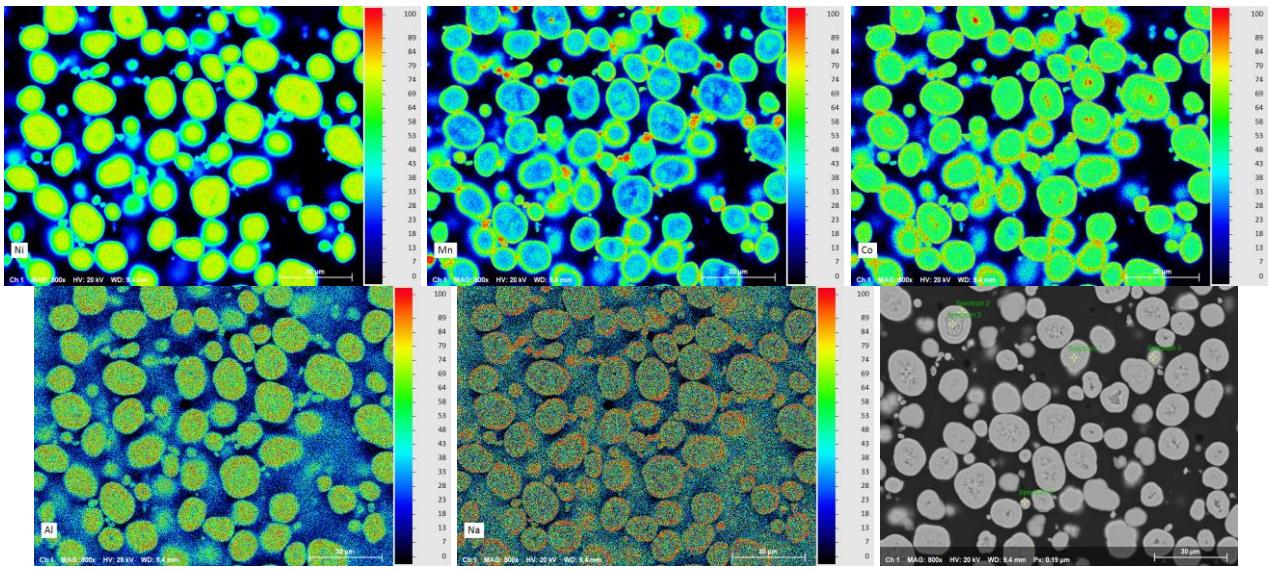

Figure 45 EDS elemental mapping of Test B32 pCAM products

In addition to the standard EDS imaging shown above, a dot scan across a single particle was conducted to better evaluate the transition rate between the two chemistries used, with the results shown in Figure 46.

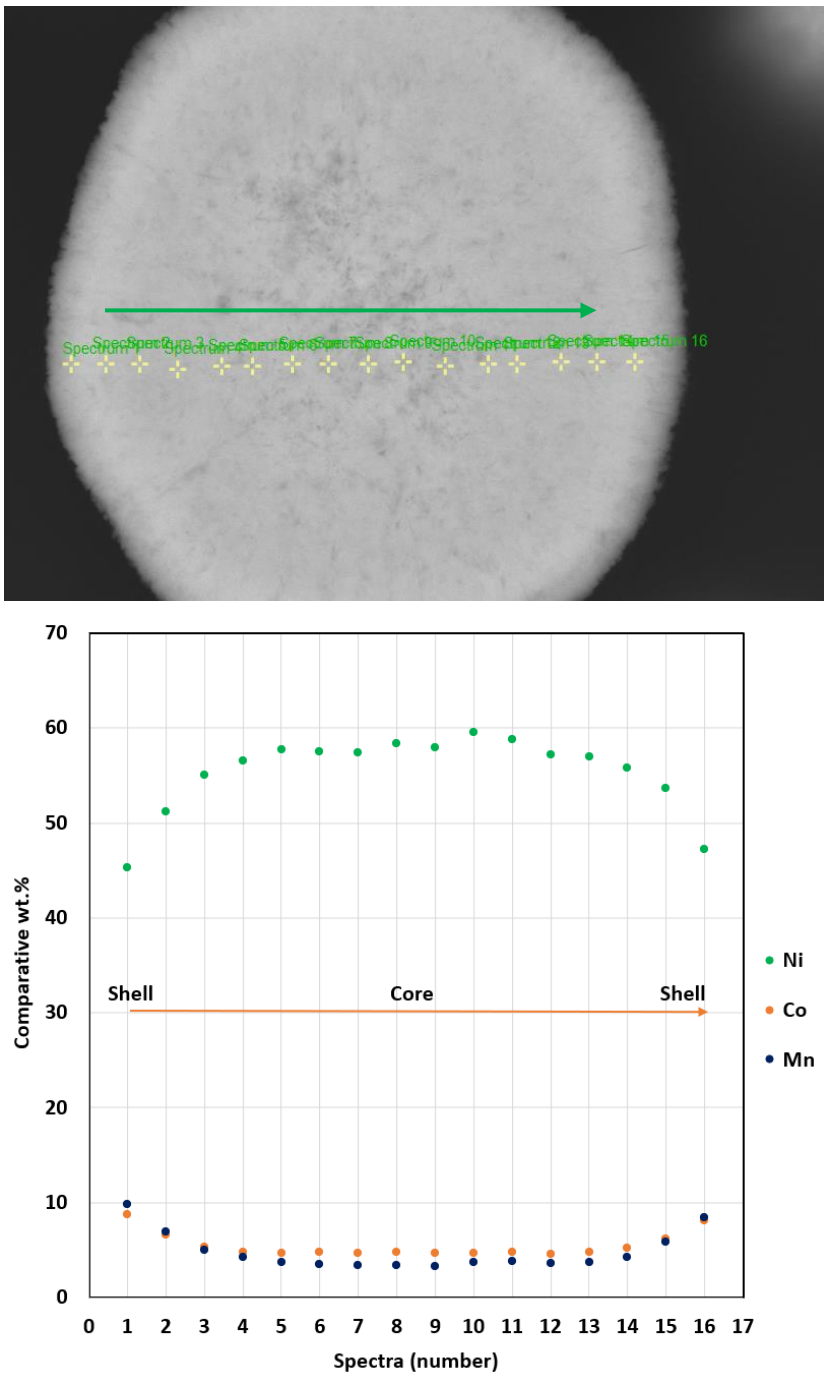

Figure 46 EDS results for major elements for the dot scan of gradient test product

7.5 Conclusions

Ti doping demonstrated promising modifications to the structural characteristics, indicating that anticipated changes occurred using Ti dopant in NCM 83 12 05 chemistry. Nonetheless, the presence of cracks in a few larger particles suggests that the Ti concentration used may not be optimal for these process conditions. For future studies, lower concentrations will be investigated to reduce particle cracking.

An elemental gradient structure featuring a Ni-rich core and a Mn/Co-rich shell was successfully achieved as anticipated. These results indicate the potential for future advancements in optimising the elemental configuration of the particles which can help producing practical commercial higher Ni chemistries.

8 Electrochemical Testing Results

8.1 Introduction

Selected pCAM samples from the above work underwent electrochemical testing following the procedures outlined below. This data is still undergoing validation, as such it is not being released at this time.

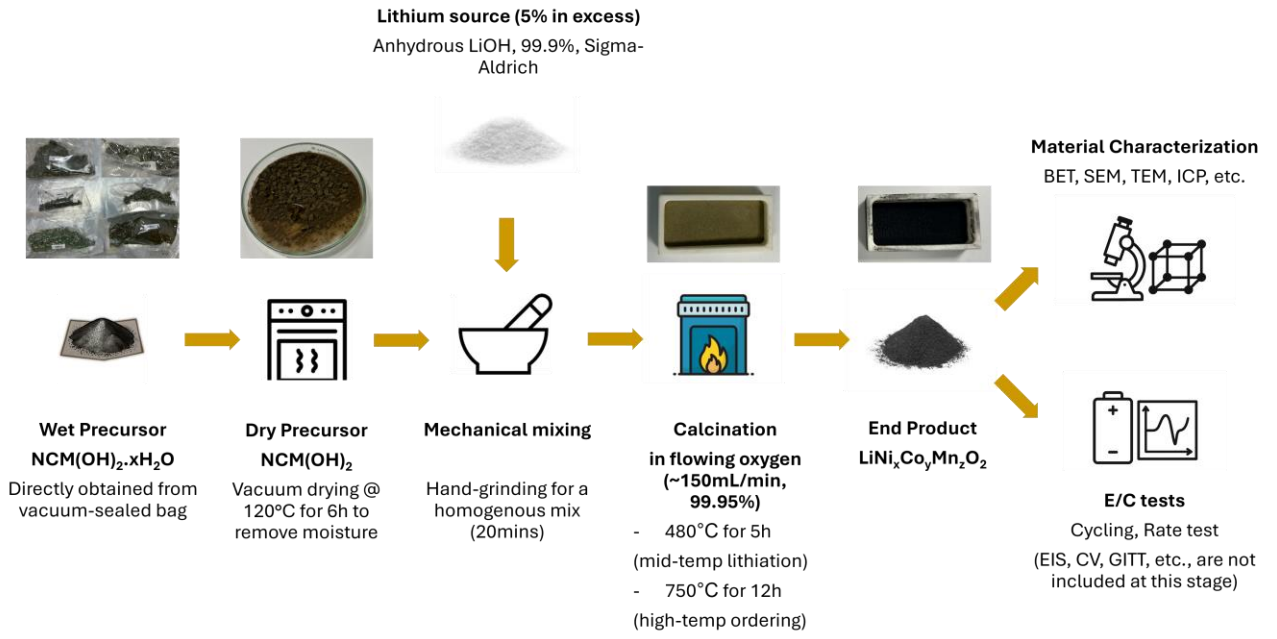

Figure 47 General flow chart – Lithiation of as-received precursor samples

8.1.1 Electrode fabrication and cell assembly

CAM powder was gently deagglomerated and mixed with Acetylene black (AB, a conductive carbon additive) and polyvinylidene fluoride (PVDF, a polymer binder) to prepare a slurry in a conventional cathode solvent 1-Methyl-2-pyrrolidinone (NMP). Slurries were vacuum-mixed to a smooth, defect free consistency and coated on aluminium foil using a fixed gap casting-blade to target the desired areal loadings. Coated foils were dried in vacuum oven overnight before punching to 8 mm cathode disk. To maintain comparability, areal loadings were kept approximately within a range of 2.0 to 3.5 mg cm^2. The 8 mm cathode disk were evenly pressed by hydraulic presser under 45 MPa to achieve uniform electrode density.

Discs were dried immediately before transfer to an Ar glovebox (O_2/H_2O ≤0.1 ppm). Cells were assembled in a CR-type coin format with lithium metal serving as both counter and reference electrode, a microporous polyolefin separator (Celgard 2325) and a carbonate electrolyte (1.0 M $LiPF_6$ in 50/50 EC/DEC, Sigma Aldrich) applied uniformly across all coin cells. After crimping, cells were rested to allow wetting and were then moved to channels for testing.

8.1.2 Electrochemical testing

Each cell underwent a low rate conditioning sequence within the voltage window of 2.8 to 4.3 V to stabilise interfaces. The first complete charge discharge cycle was used to calculate initial coulombic efficiency (ICE). Following formation, galvanostatic cycling was performed at successively higher C-rates: 0.2C, 0.5C, 1C, 1.5C and 2C, before returning to 0.2C to assess recoverable kinetic loss. At each step, multiple cycles were recorded, and the final cycle at each C-rate is used for comparison between samples. The voltage window remained fixed at 2.8 to 4.3 V vs Li/Li^+.

After rate testing, cells were cycled galvanostatically at 1C for 100 cycles within the same voltage window. Capacity retention at cycle 100 was calculated relative to the stabilised baseline established after the rate test. Coulombic efficiency was tracked cycle by cycle. Specific capacities were normalised to the active mass loading of each electrode. Capacity retention, average coulombic efficiency and rate dependent capacities were computed from the exported raw data. Ambient temperature was logged in parallel and used to interpret minor reversible capacity undulations across multi-day sequences.

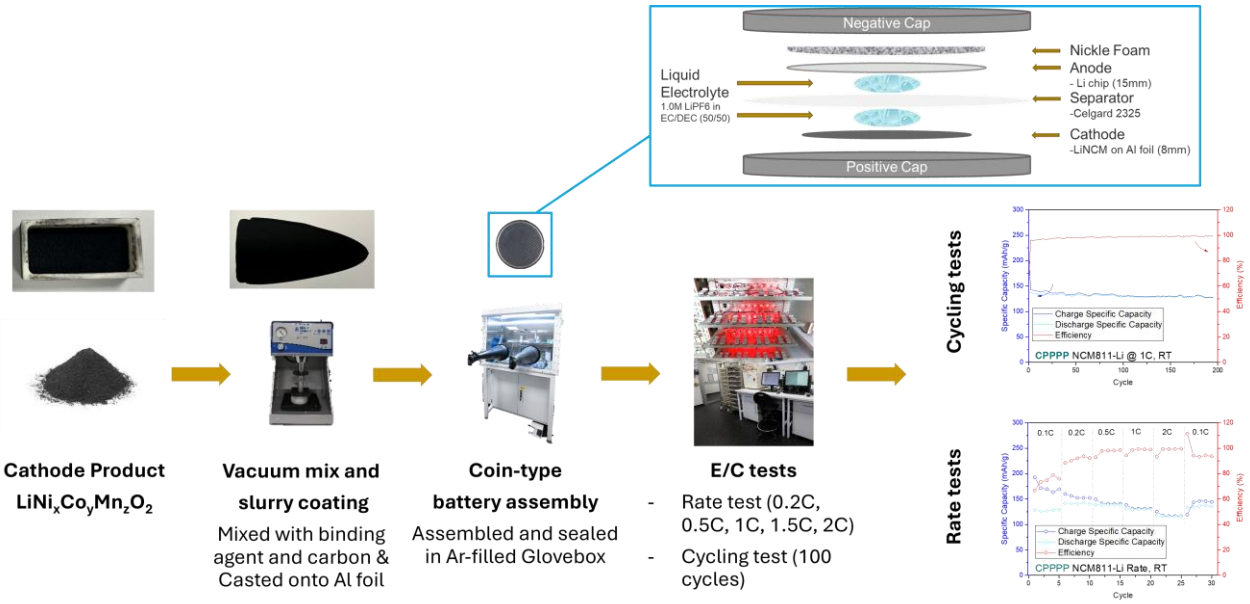

Figure 48 General flow chart – Electrochemical testing of lithiated samples

8.2 Results and Discussion

The team are not able to disclose specific results of electrochemical testing at this stage as further validation is required. Samples tested were analysed in terms of initial coulombic efficiency, capacity at various discharge rates, and capacity loss after 100 cycles at 1C, with initial results showing good performance for all measured metrics, such as capacity retention of up to 98% after 100 cycles.

References

[1] Q. Energy. "QPM Energy TECH Project." https://techproject.com.au/ (accessed.

[2] W. Metals. *Downstream nickel project Integrated battery material facility* (2024). [Online]. Available: https://www.igo.com.au/site/file/282/view/IGODownstreamNickelProjectAugust2023.pdf

[3] IEA, "Global Critical Minerals Outlook ", 2024. [Online]. Available: https://www.iea.org/reports/global-critical-minerals-outlook-2024

[4] BloombergNEF, "Electric Vehicle Outlook 2025," 2025. [Online]. Available: https://about.bnef.com/electric-vehicle-outlook/

[5] M. Beak *et al.*, "Effect of Na from the leachate of spent Li-ion batteries on the properties of resynthesized Li-ion battery cathodes," *Journal of Alloys and Compounds,* vol. 873, p. 159808, 2021/08/25/ 2021, doi: https://doi.org/10.1016/j.jallcom.2021.159808.

[6] M. Malik, K. H. Chan, and G. Azimi, "Review on the synthesis of LiNixMnyCo1-x-yO2 (NMC) cathodes for lithium-ion batteries," *Materials Today Energy,* vol. 28, p. 101066, 2022/08/01/ 2022, doi: https://doi.org/10.1016/j.mtener.2022.101066.

[7] Y.-S. Chen, R. Dominko, M. Marczewski, and W. Wieczorek, "Optimizing high-energy lithium-ion batteries: a review of single crystalline and polycrystalline nickel-rich layered cathode materials: performance, synthesis and modification," *Applied Physics A,* vol. 130, no. 10, p. 740, 2024/09/19 2024, doi: 10.1007/s00339-024-07897-7.

[8] Z. Huang *et al.*, "Effect of Mg doping on the structural and electrochemical performance of LiNi0.6Co0.2Mn0.2O2 cathode materials," *Electrochimica Acta,* vol. 182, pp. 795-802, 2015/11/10/ 2015, doi: https://doi.org/10.1016/j.electacta.2015.09.151.

[9] Y. Yerkinbekova, A. Kumarov, B. Tatykayev, A. Mentbayeva, E. Repo, and E. Laakso, "Ni-rich cathode materials with concentration gradients for high-energy and safe lithium-ion batteries: A comprehensive review," *Journal of Power Sources,* vol. 626, p. 235686, 2025/01/15/ 2025, doi: https://doi.org/10.1016/j.jpowsour.2024.235686.

[10] B. Cui, Z. Xiao, S. Cui, S. Liu, X. Gao, and G. Li, "Safety Issues and Improvement Measures of Ni-Rich Layered Oxide Cathode Materials for Li-Ion Batteries," *Electrochemical Energy Reviews,* vol. 7, no. 1, p. 27, 2024/07/22 2024, doi: 10.1007/s41918-024-00211-2.

[11] S. Mubarac, M. N. T. Silva, G. T. M. Silva, B. Freitas, J. M. Gonçalves, and H. Zanin, "Super Ni-rich and Co-poor LiNixCoyMn1-x-yO2, LiNixCoyAl1-x-yO2, and LiNixCoyMnzAl1-x-y-zO2 (x ≥ 0.85) based cathodes for lithium-ion batteries: A review on emerging trends, recent developments, and future perspectives," *Journal of Energy Storage,* vol. 96, p. 112612, 2024/08/15/ 2024, doi: https://doi.org/10.1016/j.est.2024.112612.

[12] S. Li *et al.*, "Direct Observation of Defect-Aided Structural Evolution in a Nickel-Rich Layered Cathode," *Angewandte Chemie International Edition,* vol. 59, no. 49, pp. 22092-22099, 2020/12/01 2020, doi: https://doi.org/10.1002/anie.202008144.

[13] L. Britala, M. Marinaro, and G. Kucinskis, "A review of the degradation mechanisms of NCM cathodes and corresponding mitigation strategies," *Journal of Energy Storage,* vol. 73, p. 108875, 2023/12/01/ 2023, doi: https://doi.org/10.1016/j.est.2023.108875.

[14] P. Laine *et al.*, "Co-precipitation of Mg-doped Ni0.8Co0.1Mn0.1(OH)2: effect of magnesium doping and washing on the battery cell performance," *Dalton Transactions,* 10.1039/D2DT02246J vol. 52, no. 5, pp. 1413-1424, 2023, doi: 10.1039/D2DT02246J.

[15] M. Elias, "Nickel laterite deposits – geological overview, resources and exploitation," *CODES Centre ofr Ore Deposit Research,* vol. Special Publication 4, pp. 205-220, 01/01 2002.
[16] M. Adams *et al.*, "Piloting of the beneficiation and epal® circuits for ravensthorpe nickel operations," *International Laterite Nickel Symposium,* pp. 193-202, 01/01 2004.
[17] L. T. Tijsseling, R.P. Whattoff, P. Shah, R. , "Nickel's Carbon Challenge."
[18] "A Critical Juncture: Australia's Opportunities and Challenges in Nickel," Mandala, 2024. [Online]. Available: https://mandalapartners.com/reports/critical-juncture
[19] T. Schmidt, M. Buchert, and L. Schebek, "Investigation of the primary production routes of nickel and cobalt products used for Li-ion batteries," *Resources, Conservation and Recycling,* vol. 112, pp. 107-122, 2016/09/01/ 2016, doi: https://doi.org/10.1016/j.resconrec.2016.04.017.
[20] C. M. Julien and A. Mauger, "NCA, NCM811, and the Route to Ni-Richer Lithium-Ion Batteries," *Energies*, vol. 13, no. 23*,* doi: 10.3390/en13236363.
[21] M. Srivastava, A. Kumar M R, S. Ahmed, and K. Zaghib, "Exploring oxide cathodes for Li-ion batteries: From mineral mining to active material production," *Journal of Power Sources,* vol. 645, p. 236968, 2025/07/30/ 2025, doi: https://doi.org/10.1016/j.jpowsour.2025.236968.
[22] Z. Wang *et al.*, "Advances in reactive co-precipitation technology for preparing high-performance cathodes," *Green Carbon,* vol. 1, no. 2, pp. 193-209, 2023/12/01/ 2023, doi: https://doi.org/10.1016/j.greenca.2023.12.001.
[23] H. Xie *et al.*, "Structures, issues, and optimization strategies of Ni-rich and Co-low cathode materials for lithium-ion battery," *Chemical Engineering Journal,* vol. 470, p. 144051, 2023/08/15/ 2023, doi: https://doi.org/10.1016/j.cej.2023.144051.
[24] Z. Liao *et al.*, "Revealing the Mechanism of Mg–Cu Heterolayer Doping on Ni/Li Migration Dynamics for NCM811 Cathode," *The Journal of Physical Chemistry C,* vol. 128, no. 25, pp. 10308-10316, 2024/06/27 2024, doi: 10.1021/acs.jpcc.4c02210.
[25] J. Tao, A. Mu, S. Geng, H. Xiao, L. Zhang, and Q. Huang, "Influences of direction and magnitude of Mg2+ doping concentration gradient on the performance of full concentration gradient cathode material," *Journal of Solid State Electrochemistry,* vol. 25, no. 7, pp. 1959-1974, 2021/07/01 2021, doi: 10.1007/s10008-021-04984-0.
[26] M. Shiea, A. Querio, A. Buffo, G. Boccardo, and D. Marchisio, "CFD-PBE modelling of continuous Ni-Mn-Co hydroxide co-precipitation for Li-ion batteries," *Chemical Engineering Research and Design,* vol. 177, pp. 461-472, 2022/01/01/ 2022, doi: https://doi.org/10.1016/j.cherd.2021.11.008.
[27] M. L. Para *et al.*, "A modelling and experimental study on the co-precipitation of Ni0.8Mn0.1Co0.1(OH)2 as precursor for battery cathodes," *Chemical Engineering Science,* vol. 254, p. 117634, 2022/06/08/ 2022, doi: https://doi.org/10.1016/j.ces.2022.117634.
[28] D. L. Marchisio, J. T. Pikturna, R. O. Fox, R. D. Vigil, and A. A. Barresi, "Quadrature method of moments for population-balance equations," *AIChE Journal,* vol. 49, no. 5, pp. 1266-1276, 2003, doi: https://doi.org/10.1002/aic.690490517.
[29] X. Yang *et al.*, "Growth mechanisms for spherical Ni0.815Co0.15Al0.035(OH)2 precursors prepared via the ammonia complexation precipitation method," *Journal of Energy Chemistry,* vol. 53, pp. 379-386, 2021/02/01/ 2021, doi: https://doi.org/10.1016/j.jechem.2020.05.049.
[30] A. Mersmann, *Crystallization Technology Handbook (1st ed.)*. CRC Press, 2001.
[31] C. Steyer, *Precipitation of barium sulfate in a semi-batch stirred tank reactor - influence of feeding policy on particle size and morphology*. 2012.

[32] M. H. Lee, Y. J. Kang, S. T. Myung, and Y. K. Sun, "Synthetic optimization of Li[Ni1/3Co1/3Mn1/3]O2 via co-precipitation," *Electrochimica Acta,* vol. 50, no. 4, pp. 939-948, 2004/12/15/ 2004, doi: https://doi.org/10.1016/j.electacta.2004.07.038.
[33] R. O. Fox, "On the relationship between Lagrangian micromixing models and computational fluid dynamics1This contribution is dedicated to the remembrance of Professor Jaques Villermaux.1," *Chemical Engineering and Processing: Process Intensification,* vol. 37, no. 6, pp. 521-535, 1998/11/01/ 1998, doi: https://doi.org/10.1016/S0255-2701(98)00059-2.
[34] Y. Liu and R. O. Fox, "CFD predictions for chemical processing in a confined impinging-jets reactor," *AIChE Journal,* vol. 52, no. 2, pp. 731-744, 2006, doi: https://doi.org/10.1002/aic.10633.
[35] K. El Kadi and I. Janajreh, "Desalination by Freeze Crystallization: An Overview," *The International Journal of Thermal & Environmental Engineering (IJTEE),* vol. 15, pp. 103-110, 10/02 2017, doi: 10.5383/ijtee.15.02.004.
[36] E. a. K. Isaacson, H.B., *Analysis of Numerical Methods*, G. B. C. Corporation, ed., 1994.
[37] L. A. Bromley, "Thermodynamic properties of strong electrolytes in aqueous solutions," *AIChE Journal,* vol. 19, no. 2, pp. 313-320, 1973/03/01 1973, doi: https://doi.org/10.1002/aic.690190216.
[38] A. van Bommel and J. R. Dahn, "Analysis of the Growth Mechanism of Coprecipitated Spherical and Dense Nickel, Manganese, and Cobalt-Containing Hydroxides in the Presence of Aqueous Ammonia," *Chemistry of Materials,* vol. 21, no. 8, pp. 1500-1503, 2009/04/28 2009, doi: 10.1021/cm803144d.
[39] K. Batuş, "How Particle Size Distribution (PSD) Affects Cell Capacity. Battery Design," (in English), *batterydesign.net,* 2025 2025. [Online]. Available: https://www.batterydesign.net/how-particle-size-distribution-psd-affects-cell-capacity/.
[40] S. J. Esses *et al.*, "Automated image quality evaluation of T₂ -weighted liver MRI utilizing deep learning architecture," (in en), *Magnetic Resonance Imaging,* vol. 47, no. 3, pp. 723-728, 2018/03// 2018, doi: 10.1002/jmri.25779.
[41] W. Huangfu *et al.*, "Automated extraction of mining-induced ground fissures using deep learning and object-based image classification," (in en), *Earth Surf Processes Landf,* vol. 49, no. 7, pp. 2189-2204, 2024/06/15/ 2024, doi: 10.1002/esp.5824.
[42] J. Chen, M. Zhou, H. Huang, D. Zhang, and Z. Peng, "Automated extraction and evaluation of fracture trace maps from rock tunnel face images via deep learning," (in en), *International Journal of Rock Mechanics and Mining Sciences,* vol. 142, p. 104745, 2021/06// 2021, doi: 10.1016/j.ijrmms.2021.104745.
[43] K. Song and Y. Yan, "A noise robust method based on completed local binary patterns for hot-rolled steel strip surface defects," (in en), *Applied Surface Science,* vol. 285, pp. 858-864, 2013/11// 2013, doi: 10.1016/j.apsusc.2013.09.002.
[44] G. Bakas *et al.*, "A Tool for Rapid Analysis Using Image Processing and Artificial Intelligence: Automated Interoperable Characterization Data of Metal Powder for Additive Manufacturing with SEM Case," (in en), *Metals,* vol. 12, no. 11, p. 1816, 2022/10/26/ 2022, doi: 10.3390/met12111816.
[45] R. Cohn, I. Anderson, T. Prost, J. Tiarks, E. White, and E. Holm, "Instance Segmentation for Direct Measurements of Satellites in Metal Powders and Automated Microstructural Characterization from Image Data," (in en), *JOM,* vol. 73, no. 7, pp. 2159-2172, 2021/07// 2021, doi: 10.1007/s11837-021-04713-y.
[46] B. L. DeCost, H. Jain, A. D. Rollett, and E. A. Holm, "Computer Vision and Machine Learning for Autonomous Characterization of AM Powder Feedstocks," (in en), *JOM,* vol. 69, no. 3, pp. 456-465, 2017/03// 2017, doi: 10.1007/s11837-016-2226-1.

[47] "SEM Image Analysis using Machine Learning and Deep Learning," (in en), *Spectral AB,* 2024/11/30/ 2024. [Online]. Available: https://spectral.se/blogs/webinars/sem-image-analysis-using-machine-learning-and-deep-learning.

[48] J. Cai *et al.*, "RootGraph: a graphic optimization tool for automated image analysis of plant roots," (in en), *EXBOTJ,* vol. 66, no. 21, pp. 6551-6562, 2015/11// 2015, doi: 10.1093/jxb/erv359.

[49] N. Zhang, X. Gao, X. Lai, H. Xu, Y. Liu, and H. Ma, "Research on crack detection method for shallow-buried underground compressed air energy storage cavern based on improved mask R-CNN model," (in en), *Earth Energy Science,* vol. 1, no. 3, pp. 203-212, 2025/09// 2025, doi: 10.1016/j.ees.2025.07.001.

[50] I. Rambukwella, H. Ponnuru, and C. Yan, "The role of dopants in mitigating the chemo-mechanical degradation of Ni-rich cathode: A critical review," *EcoEnergy,* vol. 3, no. 2, pp. 321-353, 2025/06/01 2025, doi: https://doi.org/10.1002/ece2.92.

For further information

CSIRO
Michael Jackson
+61 8 9334 8984
m.jackson@csiro.au
https://www.csiro.au/en/about/people/business-units/mineral-resources

Curtin University
Laurence Dyer
+61 8 9088 6122
laurence.dyer@curtin.edu.au